Radiation Effects in Molybdenum and Molybdenum-Zirconium Alloy

Kang-Yih Liou

December 1979

UWFDM-332

Ph.D. thesis.

FUSION TECHNOLOGY INSTITUTE

UNIVERSITY OF WISCONSIN

MADISON WISCONSIN

Radiation Effects in Molybdenum and Molybdenum-Zirconium Alloy

Kang-Yih Liou

Fusion Technology Institute
University of Wisconsin
1500 Engineering Drive
Madison, WI 53706

http://fti.neep.wisc.edu

December 1979

UWFDM-332

Ph.D. thesis.

RADIATION EFFECTS IN
MOLYBDENUM AND MOLYBDENUM-ZIRCONIUM ALLOY

BY

KANG-YIH LIOU

UNIVERSITY OF WISCONSIN

1979

RADIATION EFFECTS IN
MOLYBDENUM AND MOLYBDENUM-ZIRCONIUM ALLOY

BY

KANG-YIH LIOU

A thesis submitted in partial fulfillment of the
requirements for the degree of

DOCTOR OF PHILOSOPHY
(Materials Science)
at the
UNIVERSITY OF WISCONSIN-MADISON
1979

ABSTRACT

Radiation Effects in Molybdenum and Molybdenum-Zirconium Alloy

Kang-Yih Liou

Under the supervision of Professor Peter Wilkes

Void swelling and phase stability in the binary Mo-Zr system under high energy copper ion irradiation as compared with similar irradiation of pure Mo has been investigated. The over-sized Zr atoms slow down or eliminate void nucleation in the temperature range 700 - 900°C, where voids form rapidly in pure Mo. In the alloy at 700°C, voids are suppressed up to 7 dpa, at 800°C they form only after an incubation dose of 6 dpa, at 900°C the incubation dose is 1.5 dpa, but nucleation continues even at 6 dpa. However, the growth of voids once nucleated is more rapid than in Mo. The result is a reduction or supression of swelling in the alloy at lower doses or temperatures but an increased swelling at higher doses and temperatures. Dislocation loops nucleate and grow continuously in the alloy and only at 900°C (6 dpa) and 850°C (7 dpa) does a dislocation network form and inhibit further development. Analysis of larger loops between 200 Å and 300 Å observed in the alloy show that they are of the interstitial type and are faulted with $\vec{b} = a/2 \langle 110 \rangle$. Although the two-phase alloy was aged to equilibrium before irradiation, many small additional precipitates of Mo_2Zr formed at the grain boundaries, especially during irradiation at 900°C. This irradiation induced precipitation is understandable in terms of the coupling of solute flux with the defect flux due to a binding between the vacancy and the over-sized Zr atom.

A detailed theory is presented for radiation induced order-disorder phase transformations. Both radiation enhanced ordering and radiation induced disordering are described and the temperature and radiation rate-dependent balance between them is obtained. The theory is applied to the case of Cu_3Au. The free energy of partially or completely disordered phases is then calculated so that radiation modified diagrams can be computed. The theory is applied to compute the phase diagrams of the Ti-Co, Nb-Rh and Ti-Ru system under conditions typical of neutron irradiation and heavy-ion bombardment.

ACKNOWLEDGEMENTS

Of the many people at the University of Wisconsin who have aided me during the course of this study, I wish especially to thank Professor P. Wilkes, my advisor, for his continual guidance and encouragement. I am also very grateful to Professor G. L. Kulcinski for his advice and assistance.

Special thanks are due to Dr. H. V. Smith, Jr., Dr. J. H. Billen, Dr. J. B. Whitley, Dr. E. Tjhia, R. G. Lott, S. K. McLaurin, R. W. Knoll, and G. A. O'Donnell for both their assistance in the experimental work and the warm friendship during my study in the United States.

In addition, I am grateful to the University of Wisconsin Nuclear Physics Group for the use of the tandem Van de Graaff accelerator and its facilities.

This work was sponsored by the Department of Energy, and the University of Wisconsin Graduate School.

Finally, I would like to dedicate this work to my wife, Shu-Jane, whose patience and support have made the obtaining of this degree possible.

TABLE OF CONTENTS

TABLE OF CONTENTS (continued)

I. INTRODUCTION

A. Void Swelling

Irradiation of crystalline solids by energetic neutrons from fission or fusion reactions produces vacancies and interstitials. In an intermediate temperature range where vacancies and interstitials are mobile and the concentrations of these point defects are higher than the thermal equilibrium values, formation of defect clusters from this supersaturated state is favored. Voids formed from clustering of vacancies were first observed in 1967 in neutron irradiated stainless steel by Cawthorne and Fulton (1) using a transmission electron microscope. Since then radiation damage research, related to the development of advanced reactors, has been centered around the studies of void formation in metals.

The increase in the external dimensions, or swelling, of cladding materials associated with void formation is one of the major problems for the design of Liquid Metal Fast Breeder Reactors (LMFBR). This problem is exacerbated by the temperature and dose dependence of void swelling value. Because of the temperature and neutron fluence gradient in the reactor core, fuel assemblies can be stressed or bend due to nonuniform swelling. In the proposed Controlled Thermonuclear Reactors (CTR), void swelling induced by the high intensity flux of neutrons at approximately 14 MeV through the first wall will be one of the largest obstacles towards commercialization of fusion reactors (2).

Besides voids, dislocation loops which are planar clusters of either vacancies or interstitials may form in metal under irradiation. Formation of dislocation loops and their coarsening into network dislocations are related to irradiation creep and to changes in mechanical properties of metals under irradiation. Void swelling due to the clustering of the vacancies can not be separated from dislocation structures because the latter are sinks for interstitials and vacancies. Internally generated gases from (n,α) and (n,p) reactions can also play important roles in void swelling of reactor materials, because the presence of such gases in void nuclei stabalize them.

In addition to neutron damage studies, ion simulation has been widely used to obtain irradiation damage data since its first introduction in 1969 by Nelson and Mazey (3). The major advantage of ion irradiation is the high damage rate, which is three to four orders of magnitude higher than in neutron irradiation. Because no experimental facility that provides the high intensity 14 MeV neutron flux necessary to simulate damage in a CTR environment is available, ion irradiation experiments are used to study void swelling in metals which are possible candidates for the first wall material of the reactor. Implantation of helium in samples before irradiation and simultaneous helium and heavy-ion irradiation have been used to study the effect of gaseous impurities produced by neutron irradiation on void swelling. The closest simulation is the simultaneous injections of the gaseous species of helium and hydrogen and self-ion bombardment. The effectiveness of ion-simulation is still under debate.

Direct observation of damage microstructure induced by electron bombardment in high voltage transmission electron microscopes (HVEM) provides information on its evolution during irradiation. However, the structure of displacement cascades produced by neutron irradiation in a reactor is completely different from the generation of Frenkel pairs by electron bombardment. While exact correlation between charge-particle irradiation and neutron irradiation has not been attained so far, the large amount of data accumulated from the former due to its much higher damage rate are invaluable to our understanding of the phenomenon of void formation under irradiation.

Theories of void nucleation under irradiation with similar results were developed independently by Katz and Wiedersich (4) and Russell (5). Both considered interstitials as anti-particles for void clustering. Bullough (6) has developed a void growth theory which has been the most convenient theoretical formalism to evaluate swelling value as a function of irradiation and materials parameters. The temperature and dose rate dependence of void swelling derived in this theory provides the only formalism so far to correlate heavy-ion irradiation damage to neutron damage by a temperature shift (7). The theory was later extended to include the possibility of vacancy loop formation by cascade collapse such that void swelling generated by electron irradiation can be correlated to that by heavy-ion and neutron irradiation using different values of cascade collapse efficiency (8).

Experimental and theoretical studies have provided our basic understanding of void formation. Experimental results, however, also demonstrated the complicated dependence of void swelling on material parameters. Interstitial or substitutional impurities, for example, can dramatically change irradiation induced defect microstructures, and the experimental results are sometimes left unexplained. This leads one to believe that the development of swelling resisting alloys depends on our understanding of the overall behavior of point defects, defect clusters, alloying elements, and the interactions between them in an irradiation environment.

B. Phase Instability under Irradiation

While the phenomenon of void swelling of irradiated metals or alloys has been extensively investigated for the design of fast and fusion reactors, many experimental results evidence that irradiation by high energy particles can have several other effects on the structural stability of alloys. It was well known before the discovery of voids that irradiation can disorder an ordered alloy at low temperatures, and radiation induced nonequilibrium precipitation had been observed. Phase instability of alloys under irradiation, however, was not recognized as a major problem for the design of advanced reactors until recently when experimental evidences accumulated from void swelling studies.

Several reviews of phase stability have been presented (9-14). It is believed that structural stability of alloys may change during irradiation by several mechanisms.

1. The irradiation induced point defects may enhance diffusion and therefore accelerate the approach of the alloy toward an equilibrium state. In such cases, the true equilibrium state of the alloy which is

normally unobtainable because of the sluggish diffusion may be attained under irradiation (15,16).

2. Mixing of solute atoms on the surfaces of precipitates due to displacement cascades is similar to surface sputtering, and this may dissolve or redistribute precipitates in alloys (17).

3. In the case where coupling between solute atoms and point defects exist, solute atoms may be dragged by point defects and deposited at defect sinks. This radiation induced solute segregation may enrich solute concentration and result in precipitation near defect sinks (18).

In addition to these effects there is experimental evidence of formation of wrong or new phases (out of place of thermal equilibrium phase diagram), that can not be explained by any of the mechanisms described above. Examples are found in stainless steels (19) and the W-Re system (19,20). In general, irradiation displaces the alloy system from thermal equilibrium, while the return of the system back to equilibrium is accelerated by the enhanced diffusion. Whenever the new steady state obtained by the balance between these two opposite processes is different from the thermal equilibrium state, the phase stability of the alloy is modified by irradiation.

Void swelling can not be separated from phase stability because alloy microstructure may directly affect radiation induced defect microstructure by influencing void nucleation and growth. The irradiation induced redistribution of precipitates or the formation of new phase may completely change the physical properties of the alloy, from ductile to brittle, for example. This causes another material problem for the design of the advanced reactors namely the prediction of the behavior of complex commercial alloys under given irradiation conditions in the reactors.

Theories for phase stability under irradiation are reviewed in Section II-E. A recent theory which gives quantitative description of irradiation induced disorder and phase change as a function of dose rate has been developed as part of this thesis and is presented in Chapter VII.

C. The Choice of Molybdenum and Its Alloys for Radiation Damage Study

Molybdenum or its titanium-zirconium alloy, TZM, is considered as the most favored material compared to other candidates for the first wall material of the proposed fusion reactors. This is because of its physical, thermal, and neutronic properties are concerned and consider also the availability and cost. One big draw-back, however, is the difficulty of welding. Neutron and heavy-ion irradiation studies show that swelling in TZM is reduced or suppressed compared to Mo (88,90). This is an important result for high temperature fusion reactor applications. Interpretation, however, is complicated by the alloying elements or impurity level of this commercial alloy. Carbides or other precipitates are commonly found in the irradiated samples.

Both Ti and Zr are oversized alloying elements, and the effective volume of Zr is larger than Ti. Both are good getters which might change the local concentrations of available interstitial impurities of gas species. A molybdenum-zirconium binary alloy clearly simplifies the alloy composition which makes the interpretation of data easier. One objective of this experiment is to use ion simulation technique with better controlled irradiation parameters to study the heavy-ion induced damage microstructure in pure Mo and Mo-9.1 at.%Zr two-phase alloy. The University of Wisconsin tandem Van de Graaff accelerator was used to bombard samples with 14 ∿ 19 MeV copper ions at irradiation temperatures from 700°C to 1000°C.

Mo-9.1 at.%Zr alloy is a two-phase mixture of bcc Mo-rich solid solution and γ-phase (Mo_2Zr). The composition was chosen such that the alloy is close to the phase boundary at thermal equilibrium. This provides two advantages for the purpose of this study. Firstly, possible irradiation induced phase instability or change in local concentration can be detected once the amount of irradiation modification reaches the phase boundary. Secondly, a large region of matrix (Mo-7.5at.%Zr between 700°C and 900°C) was available to observe damage structure produced by irradiation to study the effect of Zr addition.

II. REVIEW OF RADIATION EFFECTS IN METALS

A. The Production of Point Defects

Elastic and inelastic interactions of energetic particles with a crystalline solid may in general generate vacancies and interstitials by displacing atoms from lattice sites, and introduce impurities from transmutation reactions. The latter is important in the case of neutron irradiation when there are finite cross-sections of (n,α), (n,nα), (n,p), and (n,n'p) reactions producing helium and hydrogen gases, which may affect the physical properties of the solid or influence the mechanisms of clustering of point defects. Generation rates of gaseous species can be calculated when the cross-sections are known. Irradiation of a metal by foreign ions also builds up impurity, which is inhomogeneously distributed because of the short range of ions in metals.

A metal atom can be displaced from its lattice site if the energy transferred to the atom when it interacts with irradiation is higher than the displacement threshold. When the PKA (primary knock-on atom) in this primary event carries a large excess kinetic energy, it can eject secondary atoms resulting in a displacement cascade. A radiation unit commonly accepted by void swelling investigators is the displacement per atom (dpa), which is the average number of times a metal atom is displaced from its regular lattice site to an interstitial position calculated from the displacement theory given a total irradiation fluence.

The displacement rate per atom (dpa rate) of a metal in a flux $\phi(E)$ by elastic collisions is given by

$$R_d(E) = \phi\ (E) \int_{E_d}^{\Lambda E} \nu(T) \ \frac{d\sigma(E,T)}{dT} \ dT \tag{2.1}$$

where,

E_d = the kinetic energy necessary to displace an atom

ΛE = the maximum energy an incident particle of energy E can transfer to the PKA

$\frac{d\sigma(E,T)}{dT}$ = the differential cross-section for an incident particle of energy E to transfer energy T to the PKA

ν = number of displacements caused by a PKA of energy T.

In most cases of neutron irradiation, there is an energy spectrum having $d\phi(E)$ neutrons in the interval dE at E, and there can be several types of reactions in which energy is transferred to the recoil. Equations (2.1) should then be generalized to

$$R_d = \sum_i \int_0^{\infty} \frac{d\phi(E)}{dE} \ dE \int_{E_d}^{T_{max}} \nu(T) \ \frac{d\sigma i(E,T)}{dT} \ dT \ . \tag{2.2}$$

In an elastic collision with an incident particle of energy E, the energy transferred to the PKA is calculated assuming a two-body interaction,

$$T = \frac{4mM}{(m + M)^2} \; E \sin^2 (\psi/2) \quad , \tag{2.3}$$

where m is the mass of the incident particle, M is the mass of the knock-on atom, and ψ is the scattering angle in the center of mass coordinate.

The maximum energy transferred is therefore

$$T_{max} = \Lambda E = \frac{4mM}{(m + M)^2} E \quad . \tag{2.4}$$

In the case of electron irradiation, classical mechanics does not apply in the energy range where the electron is capable of displacing an atom. Using special relativity theory, Equation (2.4) is replaced by

$$T_{max} = \frac{2E \; (E \; + 2m_o C^2)}{M \; C^2} \quad , \tag{2.5}$$

where m_o is the rest mass of an electron. Appropriate expressions of T_{max} should also be used in Equation (2.2) for different interactions.

The number of displacements $\nu(T)$ caused by a PKA of energy T can be evaluated by the Kinchin and Pease model (21,22) ,

$$\begin{aligned} \nu(T) &= E_c/2E_d && \text{for } T \geq E_c \\ \nu(T) &= T/2E_d && \text{for } E_c \geq T \geq 2E_d \\ \nu(T) &= 1 && \text{for } 2E_d \geq T \geq E_d \\ \nu(T) &= 0 && \text{for } E_d > T \ . \end{aligned} \tag{2.6}$$

In this model, it is assumed that all energy above a critical energy E_c is lost by electronic excitation, and hard-sphere collision is assumed below E_c. Other models or modifications have been suggested to calculate $\nu(T)$ in references 23-28, which will not be discussed in detail here. The energy required by a lattice atom to be displaced depends on crystallographic orientation. The average value is higher than the displacement threshold E_d^{Th} for displacement along the easiest direction. Furthermore, a recoil can lose energy by being channelled or focused along certain crystallographic direction (22); therefore, the displacement efficiency is reduced. The effective displacement energy E_d in Equation (2.6) is taken to be approximately $(5/3)E_d^{Th}$.

Because of the short range of ions in metals ($\lesssim$ 10 μm), calculation of heavy-ion irradiation damage is complicated by the partition of ion energy as a function of depth into the target. The most widely used formalism for this calculation is the model of Lindhard, Scharff, and Schiott (LSS) (29). The interactions between the incident charged particles and bound electrons in metals are not capable of displacing atoms; vacancy-interstitial pairs are generated by the nuclear collisions.

It is assumed in this model that energy losses by nuclear collisions and electron excitations can be treated separately. Using the screened coulomb potential for nuclear collision, LSS obtain a differential scattering cross-section

$$d\sigma = \pi a^2 f(t^{1/2})/(2t^{3/2})\ dt \quad , \tag{2.7}$$

where $t^{1/2} = \varepsilon \sin(\theta/2)$; a is the screening length and θ is the center of mass scattering angle.

Two dimensionless parameters used by LSS are the reduced energy

$$\varepsilon = E/E_L = \frac{E}{Z_1 Z_2\ e^2 (M_1 + M_2)/aM_2} \tag{2.8}$$

and the reduced range

$$\rho = R/R_L = \frac{R}{(M_1 + M_2)^2/(4\pi a^2 N M_1 M_2)} \tag{2.9}$$

where M_1, Z_1 and M_2, Z_2 are the masses and atomic numbers of the incident ion and the target atom, respectively. E and R are the energy and the range of the incident ion.

The function $f(t^{1/2})$ is calculated by Winterbon et al. for a Thomas-Fermi potential to be

$$f(t^{1/2}) = \lambda t^{1/6} [1 + (2\lambda t^{2/3})^{2/3}]^{-3/2} \tag{2.10}$$

with $\lambda = 1.309$.

The nuclear stopping power can then be caluclated by

$$(d\varepsilon/d\rho)_n = (R_L/E_L)\ (dE/dR)_n$$

$$= \int_o^E dx\ f(x)/E \qquad (2.11)$$

where $x = t^{1/2}$.

The electronic stopping power in the LSS model is found to be proportional to the velocity of the incident ion.

$$(d\varepsilon/d\rho)_e = k\ \varepsilon^{1/2} \qquad (2.12)$$

where k is a constant of the order of 0.1 to 0.2. Energy loss by electron excitation dominates at high energies but nuclear collisions become more important at low energies.

The above calculation should be corrected for range straggling and energy straggling of the incident ions (30). With the differential cross-section and the energy partition calculated by LSS model, energy losses by nuclear collision can then be converted into dpa using the Kinchin and Pease model. A Gaussian range distribution is assumed by Manning and Mueller (31). They develop a computer code to compute the dpa value as a function of depth from the bombarded surface and the positions where the incident ions stop. The E-DEP-1 code of Manning and Mueller (31) was used in this study to determine the dpa values of molybdenum and the molybdenum-zirconium alloy irradiated with copper ions.

The formation of defect clusters in metals under irradiation is affected by the spatial distribution of point defects, which depend mainly on the PKA energy spectrum. In the electron irradiation case using the high voltage electron microscope, vacancy-interstitial pairs are mostly produced in the primary events. For neutron or heavy-ion irradiation, however, many PKA's carry excess energy which is distributed in a cascade of atomic collisions producing subsequent displacements. The momentum of a PKA can be focused along a close-packed direction resulting in a replacement sequence. This produces an interstitial and a vacancy separated by the replacement sequence, which can be as long as a few 10's of Å. The resulting displacement cascade is a vacancy-rich region at the center surrounded by an interstitial-rich region. Displacement cascades may provide nucleation sites for void nucleation. However, only the vacancies which escape the cascades are responsible for void growth. Long spatial separations between vacancies and interstitials in cascades may reduce the in-cascade defect recombination, resulting in a higher concentration of free vacancies for void growth. When an ordered alloy is irradiated, although only a vacancy and an interstitial are produced at the beginning and the end of a replacement sequence, respectively, different atoms along this sequence are disordered. Radiation induced disorder is another feature of radiation damage which is affected by the structure of displacement cascades. Since this has been studied as part of this thesis, further discussion will be given in Chapter VII.

B. The Theory of Void Nucleation

When a metal is quenched from equilibrium at an elevated temperature and then annealed, the quenched-in supersaturated vacancies may nucleate and grow into voids. Classical nucleation theory, which was developed to describe condensation from the vapor phase, or precipitation from solid solution, can be readily applied to the above case of vacancy precipitation. For radiation induced void formation, however, classical nucleation theory is not applicable because of the competing effects of the supersaturated vacancies and interstitials on void nucleation. Russell and Wiedersich et al. independently developed the theory for void nucleation during irradiation. Although the details of these two models are different, they both consider interstitials as anti-particles for void nucleation and obtain similar conclusions. We shall discuss Russell's (5) model first, then summarize the approach of Katz and Wiedersich (4).

Russell considers dilute solution thermodynamics, and assumes that the lattice is in dynamical equilibrium during irradiation with a steady-state concentration of vacancies and interstitials. Displacement cascades and thermal spikes are not considered. Mono-vacancies and mono-interstitials are assumed to be the only mobile defects.

The nucleation rate can then be described in terms of the flux in cluster size space as

$$J_n = \beta_v(n)\ \rho(n) - \alpha_v(n+1)\ \rho(n+1) - \beta_i(n+1)\ \rho(n+1) \qquad (2.13)$$

where $\rho(n)$ = number of voids containing n vacancies

$\beta_v(n)$ = rate of vacancy capture by an n-order vacancy

$\beta_i(n)$ = rate of interstitial capture by an n-order interstitial

$\alpha_v(n)$ = rate of vacancy loss by emission from an n-order cluster.

$\alpha_i(n)\ \rho(n)$ is neglected because of the negligible probability of interstitial emission.

Two variables $\rho'(n)$ and $\Delta G'_n$, which are functions of n, are defined by the relationship:

$$\frac{\rho'(n)}{\rho'(n+1)} = \frac{\rho^\circ(n)}{\rho^\circ(n+1)} + \frac{\beta_i(n+1)}{\beta_i(n)} = \exp\,(\delta G'_n/kT) \qquad (2.14)$$

where

$$\delta G'_n = \Delta G'_{n+1} - \Delta G'_n \quad , \qquad (2.15)$$

and

$$\rho^\circ(n) = N_\circ\ \exp(-\Delta G^\circ_n) \qquad (2.16)$$

= the number of n-mer at the equilibrium situation that $J_n = 0$.

The nucleation rate can then be expressed as

$$J_n = -\beta_v(n)\ \rho'(n) \quad \frac{\partial[\rho(n,t)/\rho'(n)]}{\partial n} \quad . \qquad (2.17)$$

Note that the integer n in the above equation is approximated as a continuous variable for mathematical simplicity.

Equation (2.17) is now in exactly the same form as that in the nucleation theory when only vacancies are present. Following the same line of classical nucleation theory we have readily

$$J_k = Z'\beta_k \rho'_k \exp(-\tau/t) \tag{2.18}$$

with the incubation time

$$\tau = (2\beta_k Z'^2)^{-1} \quad . \tag{2.19}$$

The steady state nucleation rate is therefore

$$J_k^\circ = Z'\beta_k \rho'_k \quad . \tag{2.20}$$

The corresponding Zeldovich factor is

$$Z' = \left[-\frac{1}{2\pi kT} \left(\frac{\partial^2 \Delta G_n'}{\partial n^2} \right)_{n_k'} \right]^{1/2} \quad . \tag{2.21}$$

One should note that $\Delta G_n'$ defined in Equations (2.14) and (2.15) is not the free energy in classical nucleation theory. $\Delta G_n'$ here, containing kinetic quantities, such as βi and βv, is not a thermodynamic variable.

As is usually done in classical nucleation theory, Russell uses the capillarity model to express the free energy change ΔG_n° and derives the corresponding critical radius

$$r_k' = \frac{2\sigma V}{kT \left[\ln\left(\frac{\beta v - \beta i}{\beta_v^e} \right) \right]} \quad , \tag{2.22}$$

where σ is the surface energy, V the atomic volume, and β_v^e the impingement frequency of the thermal vacancies. One can see that in the presence of both vacancy and interstitial supersaturations, Russell's theory results in a modified Gibbs-Thompson relation [Eq. (2.22)], which is related to the difference between the vacancy and interstitial jumping rate into the void.

Compared to the case of nucleation when there are only supersaturated vacancies, Russell's results show that the size of the "critical" nucleus is increased in the presence of interstitials. The height of the activation barrier is also increased, but the peak is flatter, which means a longer incubation time.

With similar assumptions, Katz and Wiedersich (4) explicitly computed the steady state nucleation rate,

$$J = 1 \Bigg/ \int_1^\infty \frac{dx}{[\beta_v + \beta_i^\circ\, m^\circ(x,x+1)]\; S(x)n(x)}$$

$$\cong \beta_v \Bigg/ \int_1^\infty \frac{dx}{S(x)n(x)} \tag{2.23}$$

β_i° is negligible compared with β_v.

$$J = \beta_v N\, S^\circ \left[\frac{g''(\bar{x}) + (2/9)\bar{x}^{-4/3}}{2\pi}\right]^{1/2} \exp\left[g(\bar{x}) - xg'(\bar{x}) - \frac{1}{3}\xi\, \bar{x}^{2/3}\right] \tag{2.24}$$

where $\bar{x}$ is the size of the critical nucleus (a void with x vacancies), which is determined by the zero of the equation

$$\left[g'(x) + \ell n(S) - \frac{2}{3}\,\xi\, x^{-1/3}\right]_{x=\bar{x}} = 0 \qquad (2.25)$$

$$g(x) = \sum_{j=1}^{x-1} \ell n\, P_j + \ell n\left(1 + \frac{\beta_i^\circ}{\beta_v}\, m^\circ(x,x+1)\right) + \left(\frac{2}{3}\right) \ell n\, x \qquad (2.26)$$

and

$$P(x) = \left[\, 1 + \frac{\beta_i + \beta_i^\circ}{\beta_v/m^\circ(x,x+1) + \beta_i^\circ}\,\right]^{-1}$$

$$\cong \left[\, 1 + \left(\frac{\beta_i}{\beta_v}\right) m^\circ(x,x+1)\right]^{-1} \quad . \qquad (2.27)$$

In Equation (2.24), g(x) and P(x) are extended into continuous functions of x to carry out the integration, with $m^\circ(x,x+1) = [(x+1)/x]^{2/3} \exp[\ell nS - \xi(x+1)^{2/3} + \xi x^{2/3}]$ and $\xi \equiv S^\circ\sigma/kT$. $S \equiv C_v/C_{ve}$ is the vacancy supersaturation. σ is the surface energy assuming that the void is spherical, and S(x) is the surface area. n(x) is the void size distribution subjected to the constraint J(x) = 0. The superscript ° denotes values when vacancies and interstitials are in equilibrium with voids.

The steady state nucleation rate and the size of critical nuclei from Equations (2.24) and (2.25) are calculated using values for defect properties in nickel. The results show that nucleation is possible only when β_i/β_v is smaller than one; for which the physical meaning is apparent. Defect arrival rates at void surfaces are proportional to the product of their mobility and concentration. Equal numbers of interstitials and vacancies are produced by irradiation. Because interstitials have a larger jump frequency than vacancies, sinks which annihilate interstitials preferentially are required to reduce the ratio β_i/β_v to less than one. The dislocation is an example of such a biased defect sink. If there are no biased defect sinks present, precipitation of interstitials or vacancies to form dislocation loops may have to occur before void formation can take place. At a constant vacancy supersaturation, the size of critical nucleus increases with increasing concentration of interstitials; so does the incubation time. The calculated results show that the nucleation rate increases steeply as vacancy supersaturation increases. Nucleation rate therefore increases with defect production rate. Since a minimum vacancy supersaturation is necessary for void nucleation, voids form only below a temperature limit (∿0.6 absolute melting point), above which the concentration of radiation induced vacancies is negligible compared to thermal vacancies.

Wiedersich, Burton and Katz (34) extended void nucleation theory to include the effects of mobile inert gas atoms from transmutation reactions. Their result shows that insoluble helium can greatly enhance the void nucleation rate. Further discussions of Katz, Wiedersich and Russell's model, and the gas assisted nucleation can be found in references 35-39.

Wolfer and Yoo (40) have studied the interactions between the point defects and voids, and the effects of dislocation bias, and surface stress of voids on void nucleation. They found that the interaction of the point defects with the void through the image force and the surface stress introduces a strong interstitial bias, especially when the void is small. Using the approach of Katz, Wiedersich and Russell they found that because of this void bias, which is important at the nucleation stage, segregation of impurity in the material to the void surface may be necessary (to reduce the surface energy and the void bias) in addition to the dislocation bias for a significant void nucleation rate. As in the case of the dependence of the void bias on the void size, Wolfer and Yoo found that the bias factor for dislocation loops decreases with the loop radius. Void nucleation and growth rate may thereby change with the evolution of dislocation structure during irradiation.

C. The Theory of Void Growth

Several models (6,7,41,42) of void growth have been developed based on the mechanism that biased defect sinks attract interstitials preferentially, therefore more vacancies enter voids then interstitials. A rate theory developed by Brailsford and Bullough (6) has been the most convenient and accurate approach to compute the swelling associated with voids. This theory is summarized below.

Brailsford and Bullough assume that sinks for vacancies and interstitials are homogeneously distributed. The discrete random array of defect sinks is approximated by a continuum with an effective sink strength. The total sink strength parameters k_i and k_v are defined such that the loss rates of the interstitials and the vacancies in this medium are written as $(D_iC_ik_i^2)$ and $(D_vC_vk_v^2)$, respectively. The quantities $(k_i)^{-1}$ and $(k_v)^{-1}$ can be seen to be respectively the mean free distances an interstitial and a vacancy travel in the medium before becoming trapped at a sink. The effective sink strength for each type of sink (dislocation loops, dislocation networks, voids, coherent or incoherent precipitates) is derived by solving a boundary value problem for the flow of defects to a sink of that type. The defect sink considered is surrounded by a sink free region, which is enclosed by an effective medium with the total effective sink strength parameters $k_i{}^2$ and $k_v{}^2$. The effective sink strength is then calculated by satisfying the condition that the loss rate of defects to the sink is equal to the loss rate to the same type of sinks in the continuum. Voids and incoherent precipitates are considered as natural sinks which absorb vacancies and interstitials equally. Dislocations, however, are biased sinks which absorb interstitials preferentially due to the higher interaction between the strain fields of an interstitial and the dislocation. When dislocations, voids and precipitates are included as defect sinks, one finds

$$k_i^2 = Z_i\rho_d + 4\pi\, r_sC_s + Y_i4\pi r_pC_p \tag{2.28}$$

$$k_v^2 = Z_v\rho_d + 4\pi\, r_sC_s + Y_v4\pi r_pC_p \quad , \tag{2.29}$$

where ρ_d is the total dislocation density; Z_i and Z_v are respectively the bias factors for interstitials and vacancies. r_s and C_s are the radius and the concentration of natural sinks (voids or incoherent precipitates). r_p and C_p are the radius and the concentration of coherent precipitates with variable bias factors Y_i and Y_v for interstitials and vacancies, respectively. The steady state defect concentrations, C_v and C_i, are then given by the simultaneous solution of the steady state equations,

$$K - D_i C_i k_i^2 - \alpha \, C_i C_v = 0 \qquad (2.30)$$

$$K' - D_v C_v k_v^2 - \alpha \, C_i C_v = 0 \qquad (2.31)$$

where α is the vacancy-interstitial recombination coefficient; D_i and D_v are diffusion coefficients of the interstitial and the vacancy respectively, and K is the defect generation rate by irradiation. The generation rate K' of vacancies is corrected to include thermal vacancy emission.

Solution of the equations gives the interstitial concentration

$$C_i = \frac{D_v k_v^2}{2\alpha} \left\{ -(1 + \mu) + [(1 + \mu)^2 + \eta]^{1/2} \right\} \qquad (2.32)$$

and the vacancy concentration

$$C_v = \frac{D_i k_i^2}{2\alpha} \left\{ -(1 - \mu) + [(1 + \mu)^2 + \eta]^{1/2} \right\} \qquad (2.33)$$

where

$$\eta = \frac{4\alpha k_B}{D_i D_v k_i^2 k_v^2}$$

$$\mu = \frac{(K' - K)\eta}{4K}$$

and k_B is the Boltzman constant.

The volume swelling rate is then given by the net accumulation rate of vacancies at the voids

$$\frac{d(\Delta V/V)}{dt} = (D_v C_v - D_i C_i)k^{v^2} - K_v \qquad (2.34)$$

where K_v is the vacancy emission rate from the voids and k^{v^2} is the defect sink strength of the void.

After some algebra and approximation, the percentage volume swelling can be expressed by

$$\Delta V/V(\%) = SF(\zeta)\ K(t - t_o) \qquad (2.35)$$

where $S = \rho_d 4\pi r_s C_s / [(\rho_d + 4\pi r_s C_s)\ (\rho_d + 4\pi r_s C_s + 4\pi r_p C_p)]$

ρ_d = dislocation density

r_s = radius of voids (natural sinks)

C_s = concentration of voids

$4\pi r_p C_p$ = sink term for precipitates

$\zeta = 400 \exp\ [-(E_m^v/k_B)(1/T_s - 1/T)]$

$F(\zeta) = \frac{2}{\zeta}\ \{(1 + \zeta)^{1/2} - 1 - \frac{1}{2}\ \zeta\ \exp[-\frac{Q}{k_B}\ (1/T - 1/T_f)]\}$

T_s and T_f are respectively the start and finish temperatures for the void swelling regime.

Q = activation energy for self-diffusion

E_m^v = activation energy for vacancy migration

Kt = dose in dpa

Kt_o = incubation dose.

When this rate theory is used to study the dose rate dependence of the void swelling, it is shown that a change in dose rate can cause corresponding changes in the temperature dependence of swelling. A temperature shift should therefore be considered when one wishes to correlate the results of the higher dose-rate ion simulation to the swelling produced in the lower dose-rate neutron environment. Bullough and Perrin (7) obtain a formulation for this temperature shift by requiring the equality

$$K_1/D_1 = K_2/D_2 \tag{2.36}$$

where D_1, D_2 are the diffusion coefficients of the vacancy in two different irradiation environments, and K is the dose rate. This led to the expression

$$\frac{T_1 - T_2}{T_2} = \left[\frac{k_B T_2}{E_m^v}\ \ell n\left(\frac{K_1}{K_2}\right)\right] \bigg/ \left[1 - \frac{k_B T_2}{E_m^v}\ \ell n\left(\frac{K_1}{K_2}\right)\right] . \tag{2.37}$$

This homogeneous rate theory was extended later by Bullough et al. (8) in the case of heavy-ion or neutron irradiation to include the effect of displacement cascades. A parameter termed cascade collapse efficiency, which allows for the loss of vacancies to form vacancy loops from cascade collapse, is introduced in this hetergeneous rate theory. Using appropriate values of cascade collapse efficiencies, swelling produced by electron irradiation can then be correlated to that by neutron or heavy-ion irradiation.

D. The Formation of Dislocation Loops

Among the defect clusters observed in metals are dislocation loops, which provide the necessary defect-sink bias required for void nucleation and growth. Interstitial loops can be considered as planar precipitates of interstitials. A vacancy loop, however, can form by athermal collapse of the vacancy rich region at the center of a displacement cascade into a planar cluster of vacancies. Coarsening of interstitial loops is different from vacancy loops because interstitials are preferentially absorbed at both types of loops due to the dislocation bias.

Observation of dislocation loops in metals and alloys during irradiation has been reviewed by Eyre (43). Interstitial loops in fcc metals usually nucleate on {111} planes and mostly remain faulted with $\vec{b} = \frac{a}{3}\langle 111\rangle$ until they intersect with another loop. In a bcc metal, interstitial loops usually nucleate on {110} planes faulted with $\vec{b} = \frac{a}{2}\langle 110\rangle$, but they unfault to a perfect configuration with $\vec{b} = \frac{a}{2}\langle 111\rangle$ at an early stage due to the high stacking fault energy (44). Theoretically a di-interstitial is assumed to be the minimum stable loop nucleus. The steady state number density of interstitial loops when the nucleation stage has been completed is given by (43)

$$C_L^i = C_o^i K^{1/2} \exp(-E_m^i/2k_BT) \tag{2.38}$$

where C_o^i is a geometrical constant, K is the defect production rate, and E_m^i is the interstitial migration energy. When interstitials interact with impurities in the material, the effective value of E_m^i will be different from that in the pure metal because of the modified interstitial mobility. Impurities may also provide nucleation centers for loop formation.

The growth or shrinkage rate of interstitial loops can be written as

$$\left(\frac{dr_L}{dt}\right)_i = \frac{1}{b}\{Z_iD_iC_i - D_vC_v + D_vC_v^e \exp[-(E_{el} + \gamma_{SF})b^2/k_BT]\} \tag{2.39}$$

where b is the Burgers vector, E_{el} is the elastic energy of the loop, and γ_{SF} is the stacking fault energy if faulted.

Faulted loops are sessile, but when interstitial loops in bcc metals unfault after nucleation, they become glissile. Aggregation of loops in molybdenum due to the elastic interaction between them to form rafts is an evidence of unfaulted glissile loops. Because of the large bias factor when loops are small, nucleation of vacancy loops is unlikely to occur according to present theory. Vacancy loops are believed to form by athermal collapse of displacement cascades. The growth or shrinkage rate of a vacancy loop is given by

$$\left(\frac{dr_L}{dt}\right)_v = \frac{1}{b}\{D_vC_v - Z_iD_iC_i - D_vC_v^e \exp[(E_{el} + \gamma_{SF})b^2/kT] \quad . \qquad (2.40)$$

From Equation (2.40) vacancy loops are unstable because of the bias driven shrinkage at low temperature when $Z_iD_iC_i > D_vC_v$, and emission dominated shrinkage at high temperature. Interstitial loops are basically stable according to Equation (2.39); they grow due to dislocation bias and vacancy emission. The actual behavior of dislocation loops during irradiation, however, should be much more complicated than the simple model described above.

E. Theories of Phase Stability under Irradiation

Irradiation affects the structural stability of alloys in two ways. Firstly, it displaces the alloy from thermal equilibrium; and secondly, it accelerates the approach of the alloy to equilibrium by the irradiation enhanced diffusion. Three different modifications of the microstructure of the alloy may result from different effects of the above two processes:

1. Irradiation leads the alloy to a new phase equilibrium which is not described by the thermal equilibrium phase diagram, and the approach of the alloy toward the irradiation modified phase structure is accelerated by the enhanced diffusion.

2. Irradiation displaces the alloy from thermal equilibrium but does not modify the phase diagram. The tendency of the alloy to come back to equilibrium is accelerated by the enhanced diffusion.

A steady state may be attained at the balance between these two competing processes.

3. Irradiation does not affect the thermal equilibrium state; it accelerates the approach of the alloy toward thermal equilibrium which may not be attainable by thermal treatment because of sluggish diffusion.

Case (3) can be distinguished from (1) and (2) by a post-irradiation anneal, which will bring the alloy back to thermal equilibrium.

The quantitative prediction of the phase stability of alloys under irradiation is important for the design of fast or fusion reactors. Furthermore, the application of irradiation to obtain alloys with new structures and physical properties which are unattainable by thermal processes may become an important technique.

At the present time, however, even qualitative predictions of the phase stability under irradiation are not possible, because different mechanisms that can influence phase stability may work at the same time in this complicated phenomenon. The radiation enhancement of diffusion and the rate of phase transformation are better understood than the radiation induced phase change. Several models based on different mechanisms have been developed for phase stability. A recent theory of radiation induced disorder and phase instability has been developed by Liou and Wilkes (45). The details of this theory are discussed in Chapter VII. Other theories of phase stability under irradiation and related experiments are reviewed below.

1) Disorder-dissolution and Recoil-dissolution

The effect of ion irradiation on Ni-13.5 at.%Al alloys at a dose rate of 10^{-2}dpa/sec was investigated by Nelson, Hudson and Mazey (17). They observed an inverse Östwald ripening of coherent ordered $\gamma'(Ni_3Al)$ precipitates in the alloys. Large γ' particles were observed to shrink to an equilibrium size after irradiation above 300°C. A high concentration of small γ' particles re-precipitated from the matrix after 5 dpa at 550°C resulting in an identical equilibrium distribution of particle size independent of the initial γ' distributions. Below 300°C, γ' particles disordered and finally dissolved after 1 ∿ 10 dpa. Similar shrinkage of γ' precipitates to an equilibrium size was also found in Nimonic PE16 alloy bombarded by Ni ions at 640°C.

Nelson et al. (17) have presented a theory to explain the experimental observation. They suggest that a fraction f of the solute atoms in a shell of thickness ℓ at the surface of a γ' particle is lost to the matrix per unit time due to the radiation induced disorder and enhanced thermal reorder by diffusion of atoms in the shell. The dissolution rate is given by

$$\frac{dV}{dt} = - 4\pi r^2 \ell f K \qquad (2.41)$$

where K is the dpa rate, and r is the particle radius. The growth of precipitate from supersaturated solution is approximated by (46)

$$\frac{dV}{dt} = \frac{3D' C_x r}{C_p} \qquad (2.42)$$

where D' is the radiation enhanced diffusion coefficient; C_x and C_p are solute concentrations in the matrix and the precipitate, respectively. With the boundary condition for the conservation of total solute concentration,

$$C = \frac{4}{3}\pi r^3 C_p n + C_x \quad , \tag{2.43}$$

equations (2.41) and (2.42) are combined to give

$$\frac{dr}{dt} = \frac{3D'C}{4\pi r C_p} - D'r^2 n - \ell f K \tag{2.44}$$

where n = the number density of precipitates. Nelson et al. then kept n as a constant and determined the equilibrium precipitate radius by finding the zero of the equation dr/dt = 0. From Equation (2.44) one can see that $dr/dt \to \infty$ as $r \to 0$ and $dr/dt \to -\infty$ as $r \to \infty$. There is only one root r_c. Therefore, all particles larger than r_c shrink and all particles smaller than r_c grow under irradiation. It has been pointed out by Wilkes (14) that this argument is misleading. By the same argument, one can still find a solution r_c of dr/dt = 0 when the dose rate K equals zero. This is in controdiction to the Östwald ripening under thermal condition without irradiation. A modification of this model is suggested by Wilkes with some preliminary result presented in reference (14).

2) Irradiation Induced Solute Segregation

The coupling between defect fluxes and solute flux in alloys under irradiation can locally modify the composition of the alloys.

A local compositional change can be sufficient to affect the phase stability of the alloy under irradiation. Solute segregation to the voids in 1 MeV electron irradiated 18Cr-8Ni-1Si stainless steel resulting in the precipitation at void surfaces was first observed by Okamoto, Harkness and Laidler (47) in 1973. Since that time, considerable experimental evidence (18,48-58) of radiation-induced solute segregation has been reported.

Anthony (39) suggested that vacancies may dragg an alloying element to vacancy sinks when there is a strong binding between the alloying element and the vacancy. A flux of an alloying element in the opposite direction to the vacancy flux, due to preferential migration of the vacancies via the alloying element, was also proposed. Okamoto and Wiedersich (18), however, proposed an interstitialcy mechanism to explain their experimental observation in stainless steel. Under-sized atoms are preferentially accommodated in interstitial sites according to strain field models , migration of the interstitials to defect sinks could therefore enrich the concentration of the under-sized element near the sinks.

Johnson and Lam (60-62) developed a kinetic model of the irradiation induced solute segregation which applies only to dilute fcc alloys. The model assumes that interstitials are in the form of <100> dumbbells and considers the binding between a solute atom and the interstitial and/or the vacancy. The vacancy-solute complex is considered to be mobile with an energy equal to the vacancy migration energy. One immobile and one mobile interstitial-solute complex with a migration energy related to the interstitial migration energy and the interstitial-solute binding energy are included. Generation and annihilation of point defects, formation and dissociation of defect-solute complexes are treated as chemical reactions with rate constants expressed in terms of appropriate activation energies and frequency factors. Clustering of defects, however, is neglected. Phenomenological equations for the concentrations of the point defects and the defect-solute complexes can therefore be written by equating the time derivative of each concentration to the sum of the diffusion term and the generation and the annihilation terms. These equations are then solved with boundary conditions determined by the geometry of the sample being irradiated, conservation of mass, and given initial condition. Defects and defect-solute complexes or the fluxes and the local concentration of solute atoms can then be determined to describe the phenomenon of irradiation induced solute segregation. Calculations using this model for a thin-foil geometry and void geometry show that solute segregation by interstitial mechanism dominates. Significant solute segregation is found in the temperature range from 0.2 Tm to 0.6 Tm (Tm is the absolute melting point) with a peak segregation temperature which decreases as defect production rate decreases. Segregation to void surfaces is found to peak at intermediate void size due to the dependence of the interstitial flux to the void surfaces on the void size. Under heavy-ion irradiation, the variation of displacement rate with depth from the irradiated surface builds up a defect concentration gradient on both sides of the peak damage depth. Calculation using this kinetic model was extended by Lam, Okamoto and Johnson (58) to include segregation caused by the coupling between the solute flux and the defect fluxes down the defect concentration gradient. Qualitative agreements between experiments and results of the above calculations are usually found. Quantitative comparison is, however, limited by the lack of information on defect-solute binding energies, activation energies for the generation and annihilation of defect species, defect migration mechanisms and migration energies. Some defect parameters are varied to study their effect on solute segregation. By varying the vacancy-solute binding energy, for example, 0.1 eV is found to be necessary for solute enrichment near defect sinks caused by the vacancy mechanism (58).

The Johnson-Lam model is limited to dilute alloys because defect-solute bonding and migration of defect-solute complexes become ill-defined as solute concentration increases. Wiedersich, Okamoto and Lam (63) have developed a general approach for concentrated alloys without using the concept of defect-solute binding. They consider a binary A-B alloy of atomic fraction X_A, X_B and assume that the two alloying elements are randomly mixed. The local concentrations of the vacancies and the interstitials and alloy components are given by Fick's Law with defect production rate K and recombination rate R.

$$\frac{\partial C_v}{\partial t} = -\nabla J_v + K - R \tag{2.45}$$

$$\frac{\partial C_i}{\partial t} = -\nabla J_i + K - R \tag{2.46}$$

$$\frac{\partial C_A}{\partial t} = -\nabla J_A \tag{2.47}$$

$$\frac{\partial C_B}{\partial t} = -\nabla J_B \quad . \tag{2.48}$$

The coupling between defect fluxes and atom fluxes, which is the driving force for solute segregation, is accounted for by partitioning atom fluxes J_A and J_B into that occuring via vacancy flux J_R and via interstitial flux J_i and vise versa. With the conservation condition,

$$J_A + J_B = -J_v + J_i \tag{2.49}$$

equations (2.45) to (2.48) reduce to the three independent equations

$$\frac{\partial C_v}{\partial t} = \nabla[-(d_{Av} - d_{Bv})\, \alpha\Omega C_v \nabla C_A + D_v \nabla C_v] + K - R \tag{2.50}$$

$$\frac{\partial C_i}{\partial t} = \nabla[(d_{Ai} - d_{Bi})\, \alpha\Omega C_i \nabla C_i + D_i \nabla C_i] + K - R \tag{2.51}$$

$$\frac{\partial C_A}{\partial t} = \nabla[D_A\, \alpha\nabla C_A + \Omega C_A\, (d_{Ai}\nabla C_i - d_{AV}\nabla C_v] \quad , \tag{2.52}$$

where $\alpha = (1 + \frac{\partial\, \ell n\gamma_A}{\partial\, \ell nX_A}) = (1 + \frac{\partial\, \ell n\, \gamma_B}{\partial\, \ell nX_B})$, γ_A and γ_B are the activity coefficients. $d_{Av} = 1/6\, b_v^2\, Z_v \nu_{Av}$ is the product of the correlation factor, square of the jump distance, coordination number and the jump frequency into a vacant site. It is related to the partial diffusion coefficient of A atoms via vacancy flux, D_A^v, by

$$D_A^v = d_{Av}X_v \tag{2.53}$$

or the partial diffusion coefficient of vacancies via flux of A atoms, D_v^A, by

$$D_v^A = d_{Av}X_A \tag{2.54}$$

because $\nu_{Av} = \nu_{vA}$.

Other partial diffusion coefficients are similarly given by

$$D_B^v = d_{Bv}X_v \tag{2.55}$$

$$D_A^i = d_{Ai}X_i \tag{2.56}$$

$$D_B^i = d_{Bi}X_i \quad . \tag{2.57}$$

Equations (2.50) to (2.52) are numerically solved for the transient period. The steady state solution gives the relation

$$\nabla C_A = \frac{X_A X_B d_{Bi} d_{Ai}}{\alpha(d_{Bi}N_B D_A + d_{Ai}N_A D_B)} \left(\frac{d_{Av}}{d_{Bv}} - \frac{d_{Ai}}{d_{Bi}} \right) \nabla C_v \quad . \tag{2.58}$$

The vacancy concentration C_v decreases toward a defect sink. Enrichment or depletion of A atoms near the sink is therefore determined by the sign of $(d_{Av}/d_{Bv} - d_{Ai}/d_{Bi})$.

Calculations using this model in the case of a thin foil agree qualitatively with experimental dose, dose rate and temperature dependencies of solute segregation in concentrated alloys and are similar to the results of the Johnson and Lam model in dilute alloys.

3) Stability of Precipitate Nucleus under Irradiation

Maydet and Russell (64) propose that vacancy flux to an incoherent precipitate particle with over-sized solute releases the volume strain and enhances the absorption of solute atoms. Conversely for under-sized solute, excess vacancies increase the volume strain energy and promote precipitate disolution. They consider kinetic behavior of incoherent precipitates in the space of the excess vacancies n and the number of solute atoms x. The precipitates are considered to be unbiased sinks for point defects and the solute flux to the precipitate matrix interface via interstitial flux is neglected. Including the volume strain energy related to the fraction of excess vacancies and the solute-matrix misfit in the total free energy of the precipitate and using the principle of detailed balancing, dn/dt and dx/dt in the (n,x) space are derived. The critical radius of the precipitate determined by dx/dt = dn/dt = 0 is given by

$$r_c = \frac{-2\gamma\Omega ppt}{\Delta\phi} \qquad (2.59)$$

where $\Delta\phi = -k_BT\ell n\{S_x[S_v(1 - \beta_i/\beta_v)]^\delta\} - [k_BT\ell nS_v(1 - \beta_i/\beta_v)]^2/4B$

(2.60)

S_x = solute supersaturation = $C_x/C_x{}^e$

S_v = vacancy supersaturation = $C_v/C_v{}^e$

β_i/β_v = ratio of the interstitial and vacancy arrival rate at the precipitate - matrix interface

$\delta = (\Omega ppt - \Omega matrix)/\Omega matrix$ = volumetric misfit

$B = \Omega ppt\ E/9k_BT(1 - \nu)$

E = Young's modulus

ν = Poisson's ratio.

The important result is that the critical nucleus r_c is determined by an effective potential $\Delta\phi$, which is related to both thermodynamic and kinetic properties. A non-negative critical radius r_c exists only when $\Delta\phi > 0$ such that particles larger than r_c grow and those smaller than r_c shrink. With biased sinks such as dislocations and assume that incoherent precipitates are natural sinks, $\beta_i/\beta_v < 1$. Precipitates with over-sized solute ($\delta > 0$) are stabilized under irradiation and are destabilized in the reverse case ($\delta < 0$) as seen from Equations (2.59) and (2.60).

Assuming that an incoherent precipitate is a natural perfect sink for point defects and therefore neglecting the emission and absorption of solute atoms via the interstitial flux to the solute-matrix interphase could be inadequate or leading to the wrong prediction of stability of second phase during irradiation. Another problem is the fact that incoherent precipitates even when quite small can emit dislocation loops with no nucleation barrier and the energy for this process is far less than that involved in growing the precipitate to a different size. Maydet and Russell's approach, however, can be applied to the study of the kinetics of nucleation of precipitates under irradiation (65).

III. REVIEW OF RADIATION DAMAGE EXPERIMENTS ON MOLYBDENUM AND MOLYBDENUM ALLOYS

Ion and neutron irradiation damage in M_o and its commercial alloy, TZM, have been extensively studied since they were considered as potential materials for controlled thermonuclear reactor applications. Irradiation damage observed includes the following structures:

1. Voids
2. The development of void superlattice
3. Dislocation loops
4. Dislocation networks
5. Rafts - agglomerates of small dislocation loops and/or unidentified small defect clusters

Some early experiments were aimed at void swelling and possible comparison between ion and neutron damage to simulate swelling of the first wall of a fusion reactor. However, some experiments analysing all types of damage structures have been carried out to study the relations between void formation and the development of other defect structures including the effects of impurities in the materials. Damage structure in bcc molybdenum differs from fcc metals in the nature of the dislocation loops. Due to the higher stacking fault energy in the bcc structure, dislocation loops in M_o are reported to unfault in the early stage of loop formation and to become glissile. The elastic interaction between loops can then result in aggregation of the loops reported as "rafts" (43,44). Different cascade structures produced by irradiation with different ions or neutrons with different energy spectra and impurity levels in the samples affect void swelling. Scattering in the swelling values can also come from electron microscopy analysis and variation in data handling (73). Though it is difficult to draw definite conclusions from limited experimental data, general observations and some qualitative conclusions from ion and neutron irradiation studies are summarized in the following two sections.

A. Ion Irradiation Damage in Molybdenum and Molybdenum Alloys (TZM, Mo-Ti)

Void swelling data for ion bombarded M_o, TZM, and Ti-0.5%Ti alloys from previous investigations (67-73,164) are listed in Tables III-1,2,3 and the general observations are summarized below.

1. Voids are observed at all temperatures from 700°C to 1500°C in pure Mo. The reported lower temperature varies from 700°C to 800°C but the higher temperature threshold for void formation has not been reported. Peak swelling occurs above 1200°C (72).

2. At a given dpa value, void size usually increases and void number density decreases with irradiation temperature.

3. An approximately linear increase in the void volume fraction in pure Mo with increasing dose was observed while no swelling saturation was reported. The average void size was commonly found to increase with increasing dose while number density remains approximately constant. This probably indicates that void nucleation is completed early during irradiation and void growth accounts for later swelling.

4. Void swelling is reduced in TZM and Mo-0.5%Ti alloys (67,72). A 5-8 dpa incubation dose for void swelling was observed in Mo-0.5% Ti.

Small grain sized Mo-0.5%Ti alloy (∿1 μm grain diameter), however, showed no evidence of incubation dose and a tendency for swelling saturation with dose was found (72).

5. Void alignment has been observed in Mo, TZM and Mo-0.5%Ti alloys. The degree of void ordering increases with dose in appropriate temperature range. The void superlattices are bcc in structure matching the host lattice. The lattice parameter usually increases with increasing irradiation temperature such that its ratio to the void diameter (a/d_V) remains approximately constant. Further discussion of the dependence of void lattice formation in Mo on irradiation temperature and dose is given in Section (VI-A).

6. Higher densities of dislocation loops are found at lower irradiation temperatures. At temperatures just below the void formation threshold (∿750°C) the damage structure is dominated by dislocation loops with a/2 <111> Burgers vector. Interstitial loops having identical Burgers vectors tend to glide together to form rafts due to the elastic interaction between them. Isolated vacancy loops which can be formed by cascade collapse have also been observed. At temperatures above the swelling threshold, however, vacancy clusters could be stabilized to form voids instead of collapsing into loops due to the high stacking fault energy.

7. When helium was pre-injected into Mo before heavy-ion irradiation, an increase in the void number density and a decrease in the average void size were observed (74,75). Void nucleation was found to continue up to high dose levels in Mo simultaneously bombarded with

Table III-1

Summary of Heavy Ion Irradiation of Molybdenum

Ion	T(°C)	dpa/sec x 10^{-3}	dpa	$N_v(cm^{-3})$ x 10^{16}	$\bar{d}$(Å)	ΔV/V(%)	Ref.
2 MeV N^+ (a)	400	∿10	70	ND	–	–	68
	500	∿10	70	ND	–	–	68
	600	∿10	70		∿15	–	68
	700	∿10	70	visible	–	–	68
	800	∿10	70	visible	–	–	68
	850	∿10	70	visible	–	–	68
	900	∿10	50	10.5	27	0.138	68
	900	∿10	70	11.9	26	0.15	68
	900	∿10	120	10.9	34	0.225	68
	900	∿10	200	16.7	39	0.438	68
	900	∿10	400			0.55	68
	870	7	100	19	40	0.6	164
2 MeV N^+	790	7	100	ND	–	–	164
3.1 MeV V^+	750	2.98	34	ND	–	–	72
	750	3.07	35	visible	0∿54	–	72
	830	3.71	23.2	3.8	48	0.35	72
	840	5.50	17.6	5.5	56	0.98	72
	875	3.76	15.8	2.2	84	0.88	72
	880	4.45	14.9	5.4	54	0.65	72
	890	5.38	17.1	5.1	62	1.05	72
	898	4.51	32.5	3.4	82	1.56	72
	900	4.08	13.0	4.3	66	1.78	72
	900	2.57	5.4	2.5	50	0.21	72
	900	3.3	3.5	5.9	46	0.38	72
	900	4.85	5.1	4.1	51	0.36	72
	908	4.74	54.0	4.5	84	3.22	72
	928	6.67	48.9	3.0	102	2.48	72
	970	2.68	11.8	1.6	83	0.65	72

Table III-1 (continued)

Ion	T(°C)	dpa/sec x 10^{-3}	dpa	$N_v(cm^{-3})$ x 10^{16}	$\bar{d}(\mathring{A})$	ΔV/V(%)	Ref.
3.1 MeV V^+	990	2.57	5.9	2.3	63	0.38	72
	1007	3.43	15.1	1.1	108	0.98	72
	1007	2.07	9.1	2.2	82	0.81	72
	1108	5.06	10.2	0.43	172	1.43	72
	1120	2.62	10.2	0.43	160	1.21	72
	1120	2.62	10.2	0.99	120	1.24	72
	1120	2.02	2.1	0.96	98	0.57	72
	1132	5.37	14.8	0.18	223	1.50	72
	1250	4.64	33.4	0.11	504	10.30	72
	1256	6.18	44.5	0.13	400	5.80	72
	1256	5.75	41.0	0.011	1018	8.10	72
	1285	3.57	25.7	0.027	876	11.90	72
	1287	2.08	15.0	0.019	883	10.00	72
	1295	4.17	35.0	0.015	938	8.10	72
	1312	2.10	17.6	0.0064	1322	9.80	72
	1507	4.15	34.9	0.0013	2323	12.80	72
5MeV Ni^{++}	650	8	5	ND	-	-	67
	800	8	5	5	45	0.23	67
	800	3	20	5	44	0.065	73
	900	8	5	4	60	0.43	67
	900	3	2	9.3	34	0.47	73
	900	3	20	8	54	2.0	73
	900	10	2	4	37	0.3	73
	900	10	20	5	64	1.85	73
	1000	8	5	5	120	0.48	67
	1000	3	21	2.1	53	0.45	73
	1000	10	2	9	38	0.48	73

Table III-1 (continued)

Ion	T(°C)	dpa/sec x 10^{-3}	dpa	$N_v(cm^{-3})$ x 10^{16}	$\bar{d}$(Å)	ΔV/V(%)	Ref.
5 MeV Ni^{++}	1000	10	20	7.5	64	3.0	73
2.7 MeV Mo^{+}	800	2.5	2	6.1	36	0.20	66
	800	2.5	20	8.1	56	1.01	66
	900	2.5	2	8.2	40	0.34	66
	900	2.5	20	5.8	80	2.07	66
7.5 MeV Ta^{3+}	800	∿10	150	70	∿25	1.0	71
	900	∿10	38	5.0	55	0.42	69
	900	∿10	113	6.0	65	0.80	69
	940	∿10	170	4.5	76	2.5	71
	1000	∿10	1	2.5	45	0.12	71
	1000	∿10	1			0.08	71
	1000	∿10	1.2	2.3	50	0.15	71
	1000	∿10	2.8	2.7	52	0.20	71
	1000	∿10	2.9			0.24	71
	1000	∿10	3	2.45	50	0.16	71
	1000	∿10	9	4.02	55	0.35	71
	1000	∿10	10	3.53	59	0.38	71
	1000	∿10	11			0.55	71
	1000	∿10	23			0.83	71
	1000	∿10	30	4.35	76	1.0	71
	1000	∿10	90	2.86	100	1.5	71
	1000	∿10	109			2.33	71
	1000	∿10	150	2.66	136	3.5	71
	1000	∿10	160			2.2	71

(a) He Preinjected
ND Not Detected
T Irradiation Temperature
dpa Displacement per Atom

dpa/sec Dose Rate
N_v Void Number Density
$\bar{d}$ Average Void Diameter
ΔV/V Void Volume Fraction

Table III-2
Summary of Heavy Ion Irradiation of TZM

Ion	T(°C)	dpa/sec x 10^{-3}	dpa	$N_V(cm^{-3})$ x 10^{16}	$\bar{d}$(Å)	ΔV/V(%)	Ref.
3.1 MeV V^+	750	5.02	37.2	Void Visible			72
3.1 MeV V^+	750	3.28	37.4	Void Visible			72
3.1 MeV V^+	750	2.97	35.0	None Visible			72
3.1 MeV V^+	800	3.18	36.3	3.8	67	1.10	72
3.1 MeV V^+	850	3.03	9.7	1.0	63	0.15	72
3.1 MeV V^+	850	3.81	12.2	1.7	56	0.24	72
3.1 MeV V^+	850	5.28	16.9	2.8	49	0.25	72
3.1 MeV V^+	850	3.90	24.4	2.7	53	0.57	72
3.1 MeV V^+	880	5.79	66.0	3.6	52	0.35	72
3.1 MeV V^+	897	3.98	57.3	2.2	73	0.84	72
3.1 MeV V^+	900	6.77	7.1	2.5	62	0.38	72
3.1 MeV V^+	900	7.05	16.0	1.3	85	0.51	72
3.1 MeV V^+	900	5.38	19.2	3.2	59	0.47	72
3.1 MeV V^+	911	3.38	24.3	1.5	73	0.39	72
3.1 MeV V^+	926	2.81	40.4	2.6	77	0.91	72
3.1 MeV V^+	927	2.86	20.6	4.3	68	0.87	72
3.1 MeV V^+	990	7.51	17.3	0.69	60	0.10	72
3.1 MeV V^+	998	7.58	17.4	0.86	86	0.32	72
3.1 MeV V^+	1000	4.05	9.3	0.41	72	0.09	72
3.1 MeV V^+	1072	6.57	18.3	0.61	101	0.41	72
3.1 MeV V^+	1090	4.42	4.6	0.08	72	0.02	72
3.1 MeV V^+	1090	3.08	12.0	0.21	115	0.19	72
3.1 MeV V^+	1090	7.44	15.0	0.42	103	0.27	72
3.1 MeV V^+	1227	4.79	34.5	0.025	537	3.20	72
3.1 MeV V^+	1240	6.32	45.5	0.01	915	5.51	72
3.1 MeV V^+	1293	2.67	19.2	0.0018	1330	2.68	72
3.1 MeV V^+	1305	1.92	13.8	0.00076	1690	2.48	72
3.1 MeV V^+	1420	3.74	31.4	0.0071	790	2.58	72

Table III-2 (continued)

Ion	T(°C)	dpa/sec x 10^{-3}	dpa	$N_v(cm^{-3})$ x 10^{16}	$\bar{d}$(Å)	ΔV/V(%)	Ref.
5 MeV Ni^{2+}	800	8	5	3.2	60	0.36	67
5 MeV Ni^{2+}	900	8	5	1.6	80	0.43	67
5 MeV Ni^{2+}	1000	8	5	0.36	105	0.22	67

Table III-3

Summary of 3.1 MeV Vanadium Ion Irradiation of Mo-0.5%Ti.[72]

T(°C)	dpa/sec x 10^{-3}	dpa	$N_v(cm^{-3})$ x 10^{16}	$\bar{d}$(Å)	ΔV/V(%)
		Small Grains (≃0.8 μm)			
880	2.84	9.1	2.8	66	0.52
880	3.09	9.9	3.3	57	0.43
889	1.40	10.1	2.1	78	0.67
900	3.90	4.1	4.6	47	0.31
900	4.28	9.0	2.5	78	0.77
900	4.31	13.7	4.7	54	0.58
900	3.74	15.7	2.0	84	0.77
900	3.74	15.7	2.4	85	0.89
927	4.73	34.4	2.3	81	0.86
990	3.53	8.1	1.6	114	1.49
998	3.95	17.4	1.0	140	1.86
1000	4.52	18.7	0.95	148	1.88
1033	5.14	22,6	0,94	151	2.16
1038	3,44	7.9	1,3	137	2.01
1090	3.75	3,9	0,46	133	0.78
1090	2,09	11.3	0.46	185	2.18
1102	5,55	15.3	0.45	188	2,03
1110	5.06	6,1	0,80	149	1.83
1113	6,75	18.1	0.54	179	2.23
1113	6,75	13,6	0,38	200	2,00
1120	3,57	13,9	0.35	201	2.12
1227	1,19	8.6	0.0012	1263	1.59
1293	5,51	39.7	0,005	1318	7.67
1300	4,08	34,3	0,023	572	3,21
1312	3,20	26,9	0,013	739	4,41

Table III-3 (continued)

T(°C)	dpa/sec x 10^{-3}	dpa	$N_v(cm^{-3})$ x 10^{16}	$\bar{d}$(Å)	ΔV/V(%)
		Large Grains (≃23 μm)			
750	0.68	7.7	None Observed		
750	0.068	7.8	None Observed		
750	1.10	12.6	None Observed		
800	0.077	8.8	Void Visible		
900	2.32	16.7	3.3	70	0.82
900	1.84	21.0	5.0	64	0.92
907	1.38	19.9	4.8	70	1.21
910	1.61	11.6	1.2	68	0.27
915	2.54	18.3	3.2	67	0.65
1247	3.75	27.0	0.0066	959	4.88
1275	4.05	29.2	0.0053	1287	8.94
1300	2.94	24.7	0.0057	1316	8.65
1367	3.36	28.3	0.023	689	5.35
1430	4.00	33.6	0.0013	1754	4.41

helium and heavy ions (76). However, the void size distribution skewed and shifted to smaller sizes as dose increases resulting in a magnitude of void swelling similar to that in Mo irradiated by heavy ions only (76).

B. Neutron Irradiation Damage in Molybdenum and Molybdenum Alloys (TZM, Mo-Ti)

Neutron irradiation experiments have covered a wider range of temperatures from ∿77°K to ∿1635°K and a dose range from 1 x 10^{17}n/cm^2 to 3 x 10^{22}n/cm^2. It is often difficult to compare reported data because of the different neutron spectra in different locations in reactors and the uncertainty in temperatures in the reactors. Also, different secondary displacement models have been used by different investigators to calculate dpa values resulting in substantial differences (66). Tables III-4,5 list the void swelling data for neutron irradiated Mo, TZM and Mo-0.5%Ti alloys from previous studies (69,77-88). Drawing confident conclusions is very difficult due to the large spread in the data shown and the insufficient amount of data, especially for the alloys. Some experimental observations are summarized.

1. Void swelling in neutron irradiated Mo has been observed between 330°C (79) and 1300°C (69). The lower swelling threshold temperature and the peak swelling observed in this temperature range compared to that no peak swelling has been detected in heavy-ion irradiated Mo can be qualitatively understood by the effective temperature shift due to the lower point defect supersaturation produced by the lower dpa rate for neutron as compared with heavy ions.

The incubation dose for void formation is small (<0.05 dpa).

2. Void number density decreases and average void size increases in Mo as the irradiation temperature increases. Voids develop into an ordered lattice at higher doses.

3. Small vacancy loops and rafts are observed at lower irradiation temperatures in Mo. The number density of vacancy loops drops rapidly as the irradiation temperature increases and rafts become network dislocations.

4. Void formation is suppressed in neutron irradiated TZM (88,90). A fine distribution of voids at lower temperatures is replaced at T $\geq$ 750°C by a high concentration of vacancy loops and an almost complete absence of voids (90). This observation is interpreted as being due to loop stabilization due to the segregation of over-sized alloying elements to the dislocation cores (90). However, other complicated mechanisms could exist in this commercial alloy. Without understanding the complex precipitation observed in TZM, interpretation of radiation damage data is more difficult.

5. Comparison of void swelling produced by ion irradiation with neutron irradiation by normalizing the dose rates using the temperature shift model (7) can usually be made only with difficulty and is not necessarily predicted by the theory quantitatively.

Table III-4
Summary of Neutron Irradiated Molybdenum

Reactor	T(°C)	Fluence x 10^{-21}n/cm^2	N_v(cm^{-3})	$\bar{d}$(Å)	ΔV/V(%)	Ref.
Pluto	330	0.1	1.3 E17	17.4	0.036	79
Pluto	330	0.1	2.2 E17	18.6	0.072	79
Pluto	330	0.3	1.4 E17	18.4	0.046	79
Pluto	330	0.3	2.6 E17	18.4	0.085	79
EBR-II	430	∿10	5.4 E16	45	0.25	80
HFR (Bel)	440	0.35	5.0 E16	25	0.04	82
Hanford	450	0.075	2.4 E16	20∿25	0.015	67
EBR-II	455	17	6.2 E16	30	0.09	66
Pluto	475	0.1	5.8 E16	36.8	0.153	79
Pluto	475	0.1	6.2 E16	36.4	0.156	79
Pluto	475	0.3	8.4 E16	39.2	0.267	79
Pluto	475	0.3	1.0 E17	32.2	0.180	79
EBR-II	540	7.4	1.2 E17	41	0.47	66
Pluto	575	0.1	1.3 E16	63	0.167	79
Pluto	575	0.1	2.6 E16	49.8	0.167	79
Pluto	575	0.3	4.2 E16	43.6	9.181	79
Pluto	575	0.3	5.2 E16	35.4	0.122	79
EBR-II	580	10	5.8 E16	46	0.30	80
EBR-II	585	∿25	7.2 E16	64	1.10	83
EBR-II	595	7.4	1.8 E17	42	0.7	66
HFR (Bel)	600	0.52	2.0 E16	40	0.07	82
Siloe	600	0.50	8.0 E16	20∿30	0.10	84
DFR	640	20	1.0 E17	40	0.55	85
Pluto	650	0.1	2.3 E14	167.4	0.056	79
Pluto	650	0.1	9.4 E14	106.4	0.059	79
Pluto	650	0.3	2.3 E16	59.2	0.246	79
Pluto	650	0.3	2.3 E16	59.2	0.247	79
Hanford	650	15	3.5 E16	25	0.028	67

Table III-4 (continued)

Reactor	T(°C)	Fluence x $10^{-21}n/cm^2$	$N_v(cm^{-3})$	$\bar{d}(\mathring{A})$	$\Delta V/V(\%)$	Ref.
ETR	665	0.85	2.0 E16	35	0.07	67
ETR	700	0.14	3.0 E16	40	0.10	86
EBR-II	700	∿10	4.05 E16	42	0.16	80
ETR	708	0.6	7.0 E15	55	0.06	67
ETR	725	1.04	6.0 E15	65	0.11	67
EBR-II	750	9.0	9.4 E16	38	0.26	66
Pluto	750	0.1	9.9 E13	232	0.065	79
Pluto	750	0.1	6.3 E14	105.8	0.039	79
Pluto	750	0.3	2.2 E15	131.6	0.265	79
Pluto	750	0.3	3.9 E15	89.2	0.085	79
ETR	755	1.37	5.0 E15	70	0.11	67
Hanford	750	0.15	2.0 E16	35	0.045	67
HFR (Bel)	760	0.44	5.0 E15	50	0.03	82
EBR-II	790	25	5.4 E16	72	1.19	83
EBR-II	800	∿10	1.5 E16	52	0.11	80
Siloe	800	0.5	1.0 E16	80	0.20	84
Hanford	800	0.1	1.0 E16	45	0.045	67
Pluto	850	0.1	5.2 E13	218.0	0.028	79
Pluto	850	0.3	1.7 E15	149.2	0.302	79
Pluto	850	0.3	3.0 E15	89.2	0.110	79
EBR-II	900	∿10	6.7 E15	73	0.14	80
ETR	900	1.61	4.0 E15	65	0.09	67
Siloe	900	0.5	3.0 E15	80∿200	0.2∿0.4	84
ETR	970	1.96	6.0 E14	140	0.12	67
ETR	985	1.26	3.5 E14	263	0.47	67
ETR	1000	0.13	5.0 E14	200	0.19	86
EBR-II	1000	∿10	2.85 E15	102	0.16	80
ETR	1050	1.0	1.2 E14	290	0.17	87

Table III-4

Reactor	T(°C)	Fluence $\times 10^{-21} n/cm^2$	$N_v(cm^{-3})$	$\bar{d}(\mathring{A})$	$\Delta V/V(\%)$	Ref.
ETR	1150	1.0	5 E13	470	0.28	87
Siloe	1200	0.5	1 E13	300∿600	0.2	84
ETR	1230	1.68	1 E13	830	0.032	67
ETR	1300	1.98	1 E12	800	0.01	67
ETR	1380	2.74	None	0	0	67

---

* In the data from Ref. 79, Mo samples of two purities, 99,95 and 99,97%, were irradiated for each temperature and fluence.

Table III-5

Summary of Neutron Irradiated Molybdenum Alloys.

Reactor	T(°C)	Fluence x 10^{-21} n/cm^2	Nv(cm^{-3})	$\bar{d}$(Å)	ΔV/V%	Alloy	Ref.
Pluto	330	0.3	9.7 E14	39.8	0.003	TZM	79
Pluto	475	0.1	8.7 E16	34.8	0.192	TZM	79
Pluto	475	0.3	1.0 E17	32.8	0.190	TZM	79
EBR-II	500	38	-	-	0	TZM	88
EBR-II	500	80	-	-	0.01	TZM	88
Pluto	575	0.1	3.2 E16	41.4	0.119	TZM	79
Pluto	575	0.3	1.1 E17	35.0	0.249	TZM	79
EBR-II	600	38	-	-	0.79	TZM	88
DFR	640	20	-	-	0.55	TZM	89
Pluto	650	0.3	6.0 E16	42.4	0.237	TZM	79
EBR-II	425	25	0	0	0	Mo-0.5Ti	79
EBR-II	430	10	9.84 E16	37	0.28	Mo-0.5Ti	79
EBR-II	580	10	7.75 E16	46	0.44	Mo-0.5Ti	79
EBR-II	585	25	2.4 E17	69	4.5	Mo-0.5Ti	79
EBR-II	700	10	5.2 E16	49	0.34	Mo-0.5Ti	79
EBR-II	790	25	6 E16	72	1.3	Mo-0.5Ti	79
EBR-II	800	10	1.9 E16	53	0.18	Mo-0.5Ti	79
EBR-II	900	10	6.9 E15	86	0.27	Mo-0.5Ti	79
EBR-II	1000	10	3.3 E15	100	0.31	Mo-0.5Ti	79

IV. EXPERIMENTAL PROCEDURE

A. Pre-irradiation Specimen Preparation

1) High Purity Mo

Pure Mo was the reference material supplied by Pacific Northwest Laboratory (PNL) for an interlaboratory correlation experiment entitled "the Body-Centered Cubic Ion Correlation Experiment" (73). Table IV-1 contains the vendor's analysis of the original molybdenum ingot and the chemical analysis for the interstitial elements after annealing at PNL for 2 hours at 1600°C in a vacuum of 1×10^{-7} torr. The average grain size was approximately 60 μm. The material obtained from PNL was in strip form 7 cm x 1.25 cm x 0.15 mm thick. To accommodate this material into the sample holder for irradiation (Figure IV-8) it was cut in half and two 3.2 mm diameter and five 4.8 mm diameter holes were spark machined in the sample strips. After spark machining, but prior to irradiation, the specimen strips were electropolished in a 15% H_2SO_4, 85% methyl alcohol solution at -20°C and 10 volts to produce a flat surface. Although there was some preferential grain boundary attack, the as-polished surface was generally very smooth.

2) Mo-9.1at.%Zr Alloy

Figure IV-1a shows the phase diagram of Mo-Zr binary alloy from E. Rudy (95). The Mo-rich solid solution is bcc in structure. The intermetallic compound $\gamma(Mo_2Zr)$ is a Layes phase isotypic with $MgCu_2$ (C15 type) with lattice parameter a = 7.596 Å (96). On the Zr-rich side, the bcc solid solution decomposes eutectoidally to form a mixture of the hexagonal α-Zr and $\gamma(Mo_2Zr)$. The details of the Mo-rich

Table IV-1a

Vendor's Chemical Analysis of Molybdenum Ingot*.

Elements	wt.%
C	0.005
O	0.0005
N	0.002
H	<0.0001
Fe	0.004
Ni	<0.001
Si	0.001

*From Reference 73.

Table IV-2b

Chemical Analysis of Interstitial Impurities after Vacuum Anneal*.

Elements	wt.%
C	<0.001
O	0.001
N	0.001
H	0.0003

*From Reference 73.

side of the phase diagram are shown in Figure IV-1b. The solid solubility of Zr in Mo at temperature near 1160°C is 9.1 at.% or 8.5 wt.% as indicated in Figure IV-1b. The thermal equilibrium Mo-9.1 at.% Zr alloy in the temperature range (700-900°C) of this study is a two-phase mixture of γ and the Mo-rich solid solution ($\sim$7.5 at.%). The composition of this alloy is close to the phase boundary such that the major portion of the alloy is the bcc Mo-rich matrix.

Mo-9.1 at.% Zr alloy for this study was prepared by melting marz grade Mo and marz grade Zr in argon atmosphere in a MRC (Materials Research Corporation) arc melter. The alloy was arc melted and stirred while a piece of Zr used as a getter was kept hot. After each melt, the alloy was turned over and the melting process was repeated six times to insure complete mixing. The as-cast alloy had the typical dendritic structure which formed when the alloy was slowly cooled from liquid into the two-phase region then down to room temperature. 1.5-2 mm thick slices were cut from the as-cast alloy using a high speed diamond wheel. A slice of the as-cast sample was homogenized by annealing at 1650°C in the one-phase region for 30 hours. This solution treatment was carried out in a 10^{-8} torr vacuum by electron beam heating in an ultra-high vacuum furnace, a facility designed and constructed for this experiment.

The specimen holder and the filament design in the furnace are shown in Figure IV-2. The specimen holder was constructed of tantalum mesh spark-welded on a tantalum frame which was supported by two 99.95% alumina rods to reduce the loss of heat by conduction. Five

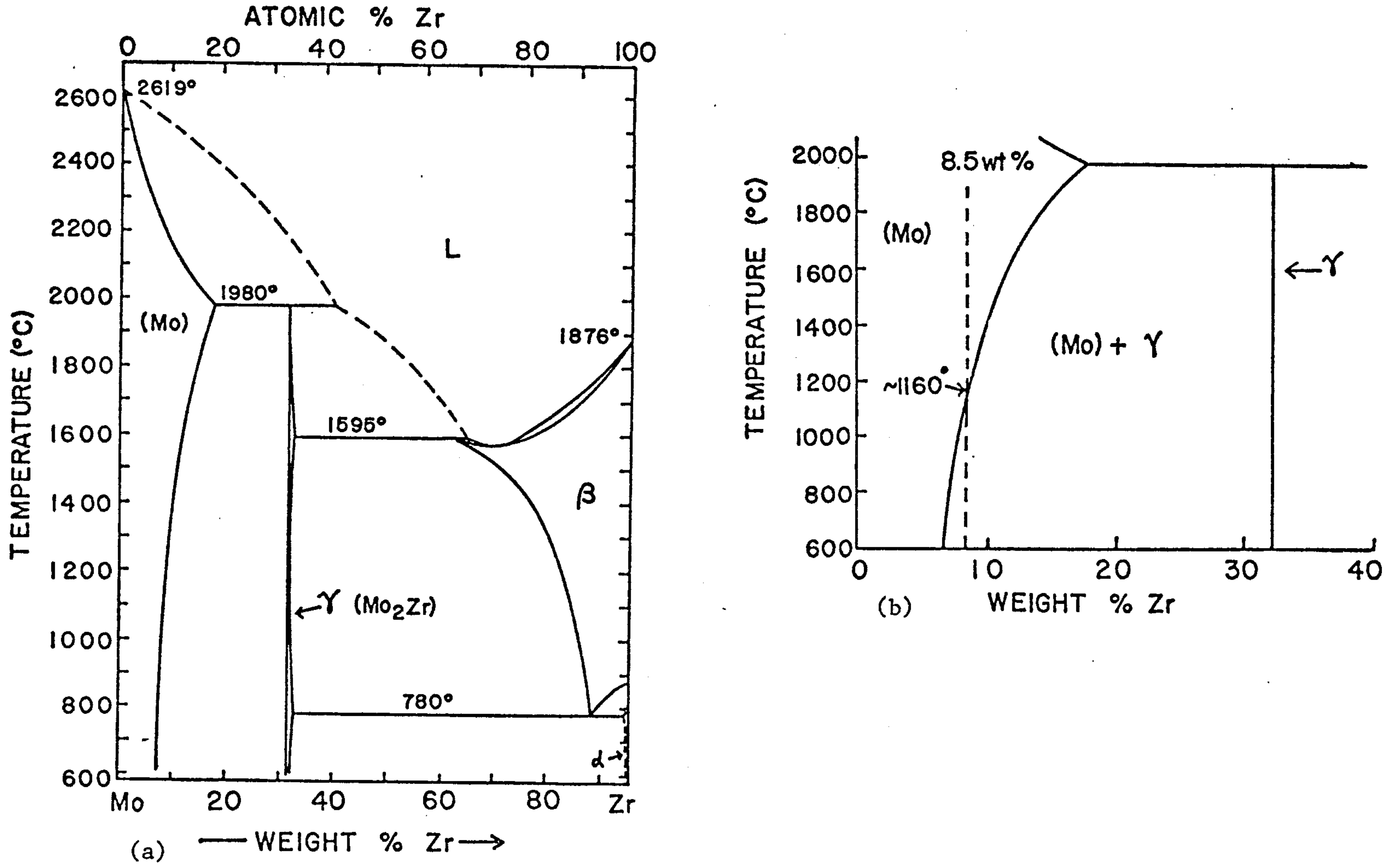

Figure IV-1. (a) Phase diagram of the Mo-Zr system, (b) details of the Mo-rich side. The dashed line in (b) shows the total composition of the alloy used in this study (8.5-wt.% or 9.1-at.%Zr).

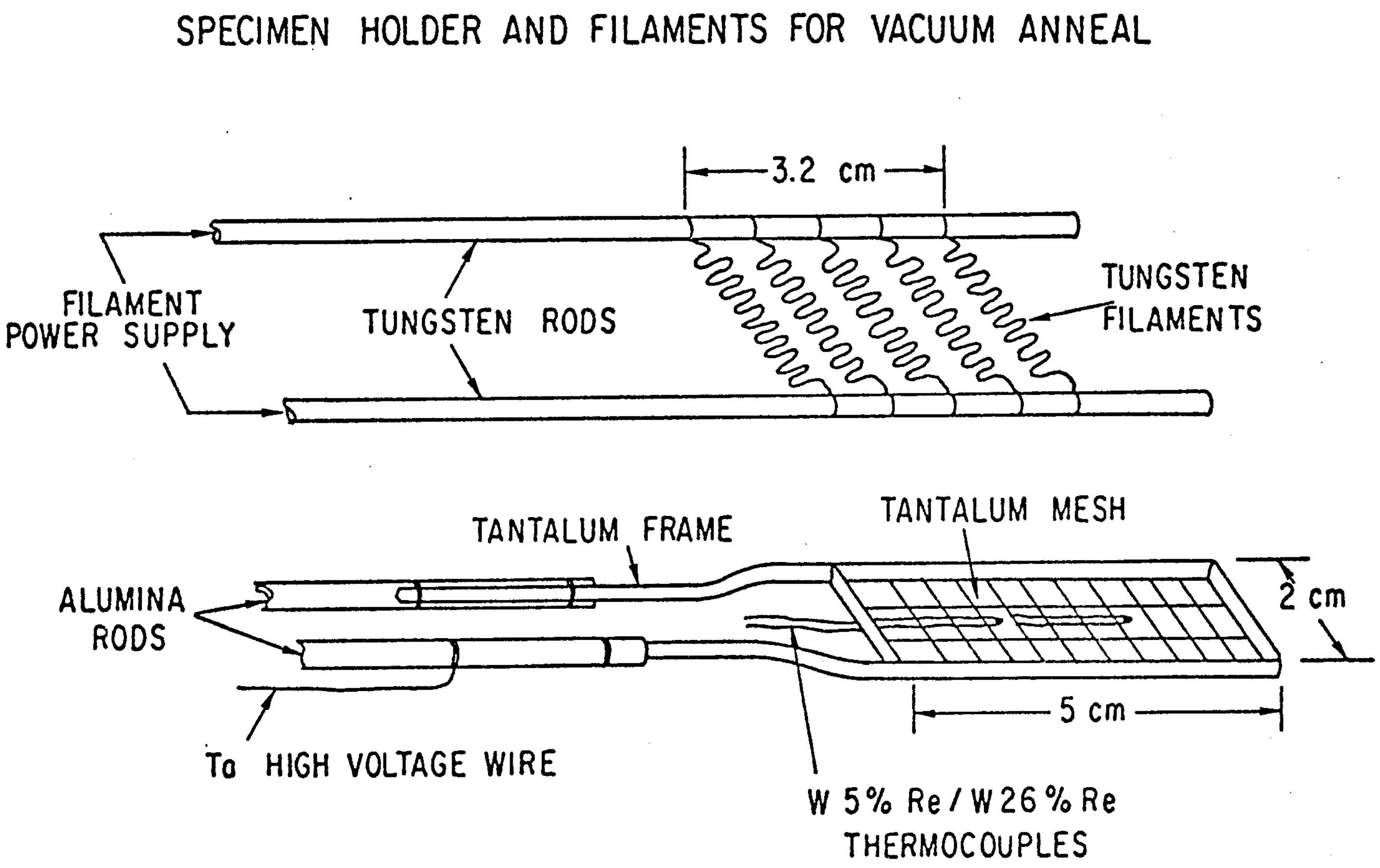

SPECIMEN HOLDER AND FILAMENTS FOR VACUUM ANNEAL

Figure IV-2. The specimen holder and filaments for vacuum anneal by electron beam heating. Not shown in the diagram is a heat shield constructed of tantalum foil enclosing the specimen holder and filaments with an open window for pumping.

filaments located at ∿2 cm above the sample holder were constructed into the shape shown in Figure IV-2 to increase the homogeneity of electron bombardment. The specimen holder was biased at 2 KV for high temperature anneals. The sample temperature was measured with two pairs of W 5% Re - W 26% Re thermocouples. The hot zone during an anneal at 1650°C was approximately 2.5 cm. Figure IV-3 contains a series of optical micrographs of sample surfaces etched with a solution of 15 grams $K_3Fe(CN)_6$ and 2 grams NaOH in 100 mℓ water at room temperature. Figure IV-3a shows the dendritic structure in the as-cast Mo 9.1 at.% Zr alloy. Figure IV-3b shows the microstructure of the alloy annealed at ∿1650°C for 10 hours in 10^{-8} torr vacuums. After an anneal at ∿1650°C for 30 hours, the homogenized alloy is shown in Figure IV-3c. Outgassing of argon introduced into the alloy during arc melting was detected by residual gas analysis during the vacuum anneal. A small argon peak observed at the beginning of the anneal disappeared after approximately 5 hours. The residual gas was dominated by hydrogen with relatively negligible amounts of water and hydrocarbons. Being homogenized by solution treatment in the one-phase region, the alloy was slowly cooled into the two-phase region and annealed to obtain a mixture of the $\gamma(Mo_2Zr)$-particles and the bcc Mo-rich solid solution.

A slice of the homogenized alloy was thinned from both sides by mechanical polishing. One side of the slice was then electropolished in 12.5% sulfuric acid and 87.5% methanol at -35°C and 20 volts to give a smooth surface for irradiation. The thickness of the polished

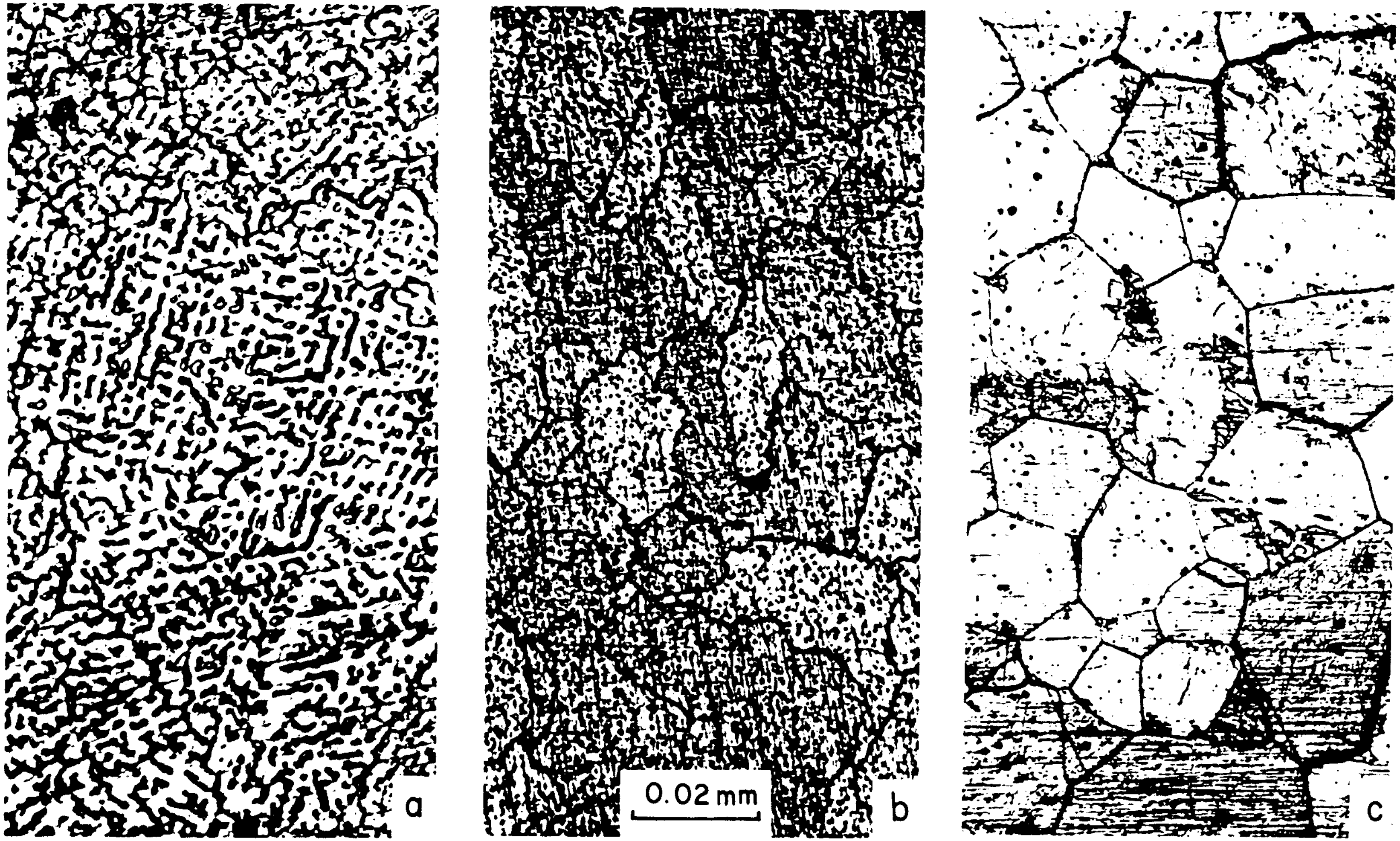

Figure IV-3. Optical micrographs showing alloy structure of Mo-9.1 at.%Zr during 1650°C anneal. (a) dendritic structure in the as-cast alloy, (b) after 10 hrs anneal, and (c) homogenized two-phase alloy after 30 hrs anneal and slowly cooled.

samples varied from 0.3 to 0.4 mm. 3-mm discs that fit the transmission microscope sample holder were spark machined from slices of the alloy. The discs were electropolished in the same solution for 20 seconds to remove possible oxide film produced during spark machining. Before irradiation, the samples were annealed in the ultra-high vacuum furnace in the two-phase region at 1050°C to outgas any hydrogen injected into the samples during electropolishing in acid. This was followed by an anneal at the irradiation temperature for ∿40 hours in 10^{-8} torr vacuum to obtain an equilibrium, two-phase mixture of $\gamma(Mo_2Zr)$ and Mo-rich solid solution. (The first irradiation on Mo-9.1 at.% Zr at 900°C and 700°C was an exception in which the samples were annealed at 900°C to stabilize the two-phase mixture.) The average grain size of the alloy samples was approximately 200 µm (Figure IV-3c).

B. Irradiation Facilities and Procedure

The University of Wisconsin tandem Van de Graaff accelerator was used to irradiate the samples with high energy copper ions. Figure IV-4 shows schematically the components of the irradiation facility.

Copper ions from a Sputter Penning Ionization Gauge Source (SPIGS) developed by Smith and Richards (91) was used to irradiate Mo and Mo-9.1 at.% Zr samples. However, a SNICS (Source of Negative Ions by Cesium Sputtering) ion source with a higher beam intensity developed later (92,93) was used for the last irradiation on Mo-9.1 at.%Zr alloy. Although self-ions are more appropriate for heavy-ion irradiation experiments, the intensity of negative molybdenum or

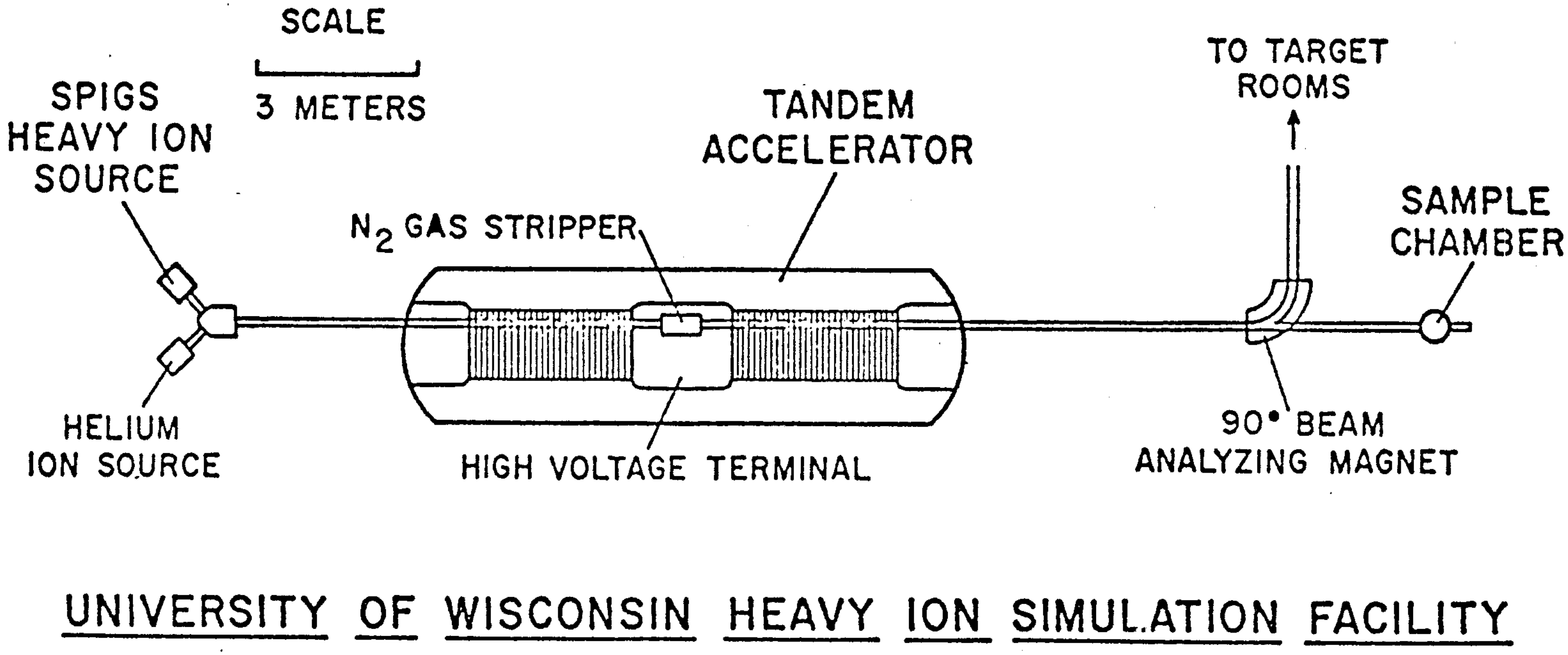

Figure IV-4. Schematic of the heavy ion irradiation facility at the University of Wisconsin – Madison.

zirconium ion beams was not high enough to irradiate samples in practicable machine time. The impurity effect due to the use of foreign copper ions, however, may be avoided for low dose irradiation by using a high accelerating voltage capable of separating the implanted copper ions from the electron microscopy analysis zone in the sample. The energy attained by ions in a tandem accelerator (with gas stripping in the dome) is given by

$$E = (q + 1)V \tag{4.1}$$

where V is the dome voltage of the accelerator and q is the charge of the copper ions after the gas stripper.

The irradiation sample chamber was located along the beam line behind a 90° analyzing magnet which had been used to bend lighter particle beams into other target rooms. This magnet, however, can only bend the copper ion beam by $\sim 1/4°$ because of the small charge to mass ratio. The magnet together with a quadrupole lens and slits were used to separate the undesired ions from the copper ions at the selected charge state. Figure IV-5 shows a schematic of the beam line extension after the 90° magnet and the sample chamber. The details of the sample chamber with the charge state analysis device are shown in Figure IV-6. The energy of the bombarding ions, or the charge state of the beam, was determined by elastic scattering of the beam by a thin gold foil though 90° recorded by a solid state detector. Cu^{4+} ions of either 17 or 18.8 MeV (in separate runs) were used to irradiate

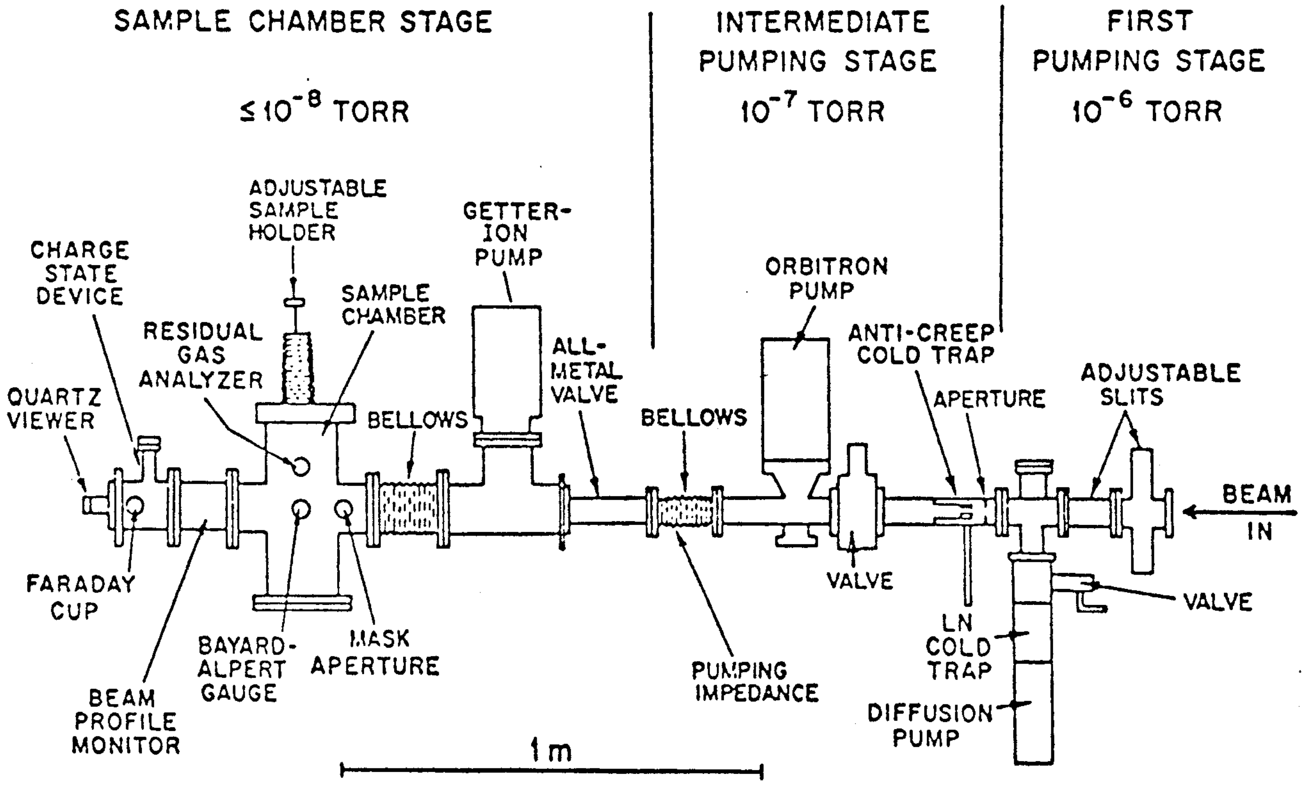

Figure IV-5. The target chamber and beam line extension of the heavy-ion irradiation facility.

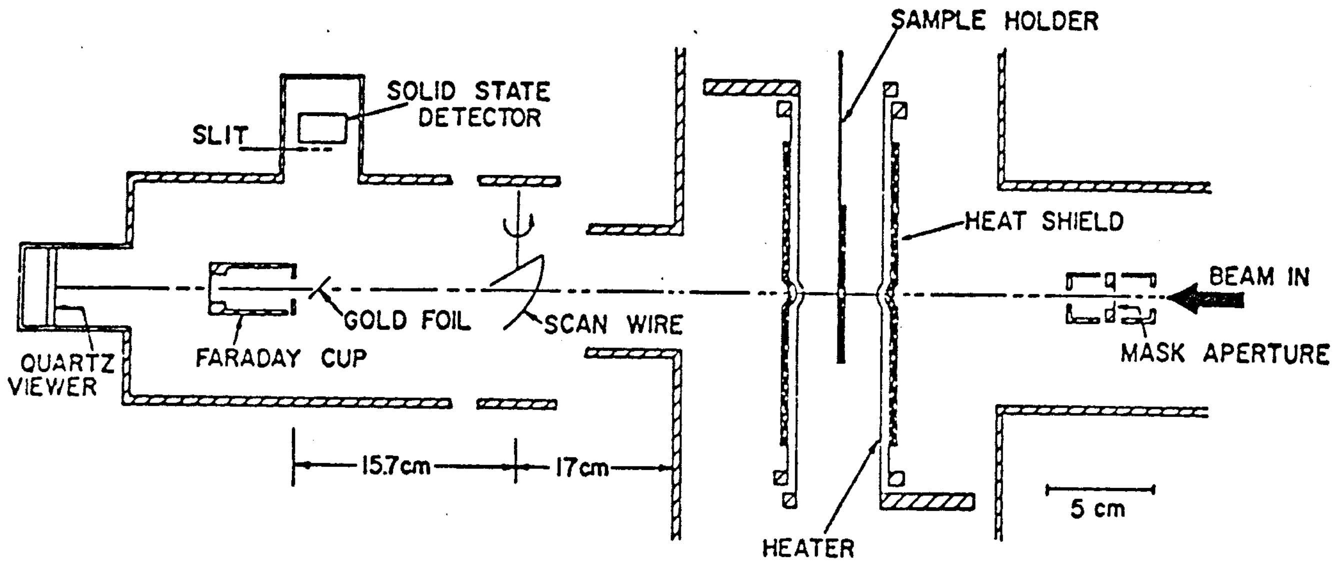

Figure IV-6. Schematic of the sample chamber showing details of ion beam diagnostic devices, heater, heat shield, and sample holder.

pure Mo samples while 14 MeV Cu^{3+} ions were used to bombard the Mo-9.1 at.% Zr alloy. A typical energy spectrum of bombarding ions obtained from an irradiation with Cu^{4+} ions is shown in Figure IV-7. The beam current density collimated by a 3 mm-diameter mask aperture could then be determined with the charge state spectrum and the current measured with a Faraday cup located behind the sample holder. The total fluence of particles on the sample was then given by the integrated beam current over irradiation time divided by the final charge state.

The beam line and the sample chamber were pumped in three stages as shown in Figure IV-5. A diffusion pump with a cold trap pumped the first section down to $\sim 2 \times 10^{-6}$ torr. A 400 liter/sec orbitron pump was used to pump the second section, which was isolated from the first section by a liquid nitrogen cold trap. An ultra-high vacuum irradiation environment was then produced in the sample chamber by a 1000 liter/sec getter-ion pump. Samples were irradiated at pressures near 1×10^{-8} torr at temperatures from 850 to 1000°C, and at $5\text{-}8 \times 10^{-9}$ torr at 700 and 800°C. Residual gas analysis prior to the first 1000°C irradiation on Mo revealed that the typical residual gas in the sample chamber was composed of 57% H_2, 18% CO, 22% H_2O, 2% CO_2, and 1% CH_4.

The samples were heated by thermal radiation from a cylindrical heater constructed of tantalum sheet, which was surrounded by a 15 layered spirally wound heat shield. Pure Mo sample in strip form 7 cm x 1.25 cm x 0.15 mm thick was placed in a tantalum sample holder shown

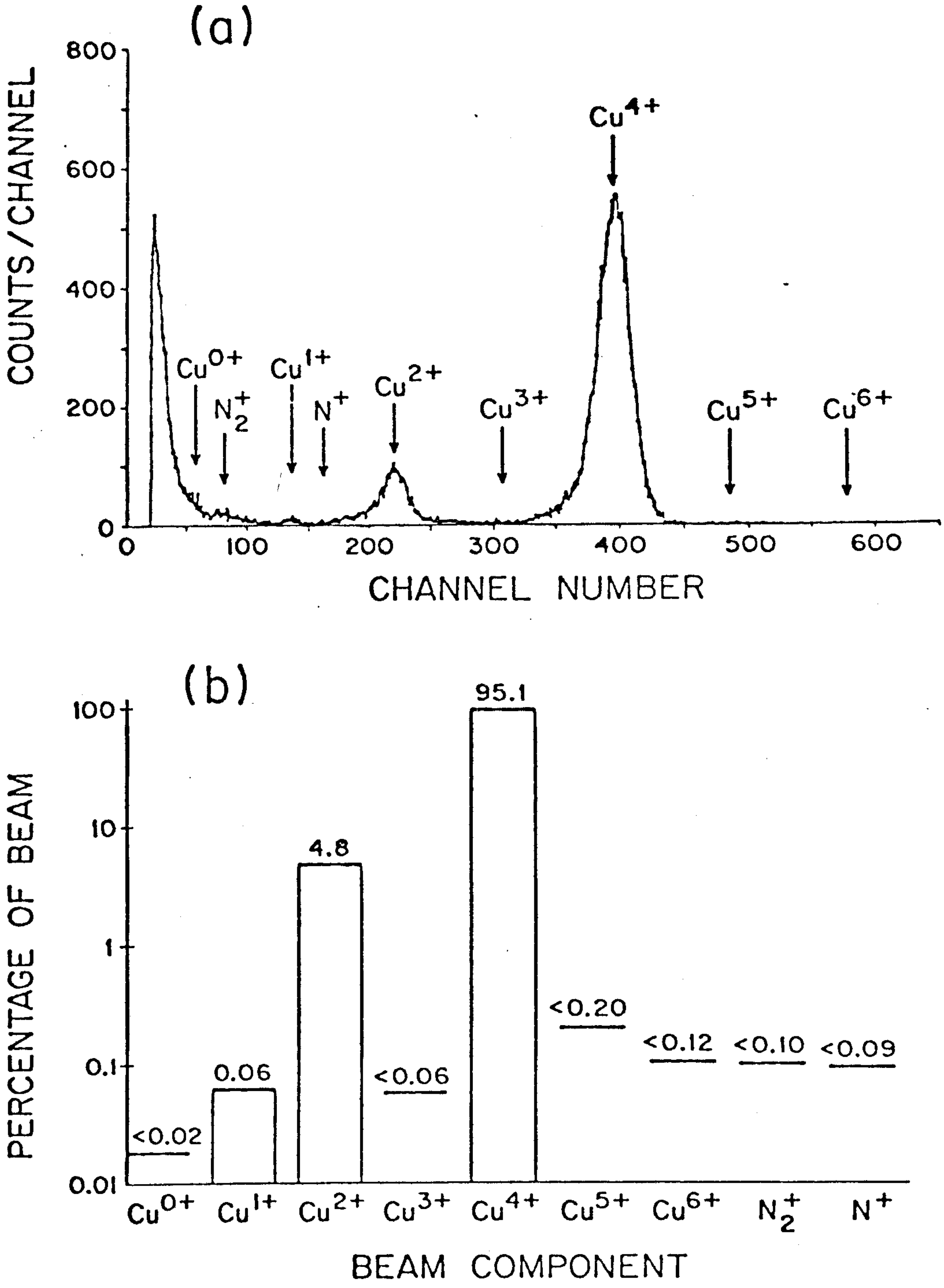

Figure IV-7. (a) A typical energy spectrum for the ion beam during an irradiation with Cu^{4+} ions. (b) The composition as determined from the above spectrum.

in Figure IV-8. Six 3-mm disc samples were cut from the 6 irradiated spots on a single irradiated sheet for electron microscopy examination. Irradiation temperatures were measured with two pairs of chromel-alumel thermocouples. For the irradiation on Mo-9.1 at.% Zr, a new specimen holder was used (shown in Figure IV-9). This holds eight 3-mm disc samples with a pair of thermocouples at each sample position. The sample holder was suspended from a bellows to allow adjustment of the sample position. The sample holder, heater, and heat shield were shorted together and isolated to form a Faraday cup unit to measure the beam current.

A computer code (E-DEP-1) by Mannig and Mueller (31) using the model outlined in Section II-A was used to compute the dpa value (displacement per atom) as a function of depth from the irradiated surface. A threshold displacement energy of 37 eV was used for pure Mo in the computation. For Mo-9.1 at.% Zr, the threshold displacement energy was assumed to be the average of 37 eV for Mo and 24 eV for Zr over the atomic fraction of the alloy composition. A typical depth distribution of damage computed by E-DEP-1 code for 17 MeV copper irradiation on molybdenum is shown in Figure IV-10. The implanted Cu ion distribution as shown in the diagram was gaussian in form at 2.7 μm from the irradiated surface while the damage is peaked at 2.5 μm. For 14 MeV Cu on Mo-9.1 at.% Zr the peak damage is located at 2.2 μm and the implanted Cu ions are deposited near 2.4 μm from the irradiated surface. Whitley et al. (32,33) have shown by an experimental study on the depth dependence of ion damage profile in Ni that the

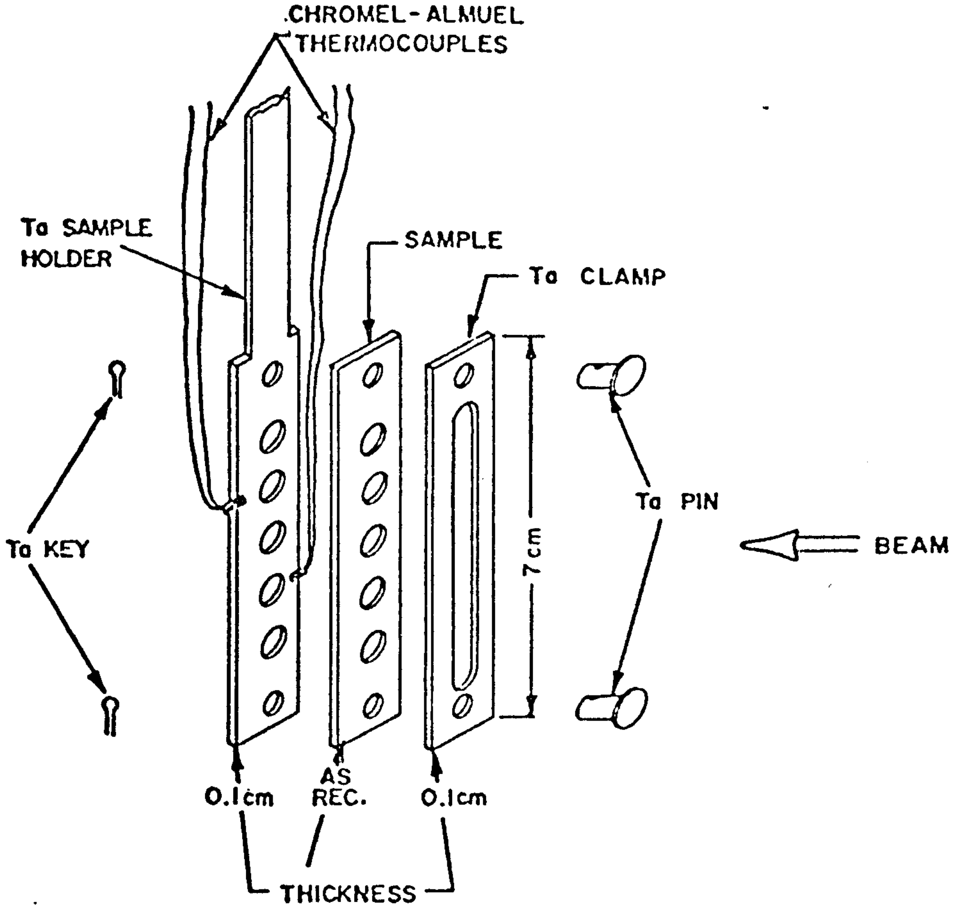

Figure IV-8. The sample holder used during copper ion bombardment on pure molybdenum.

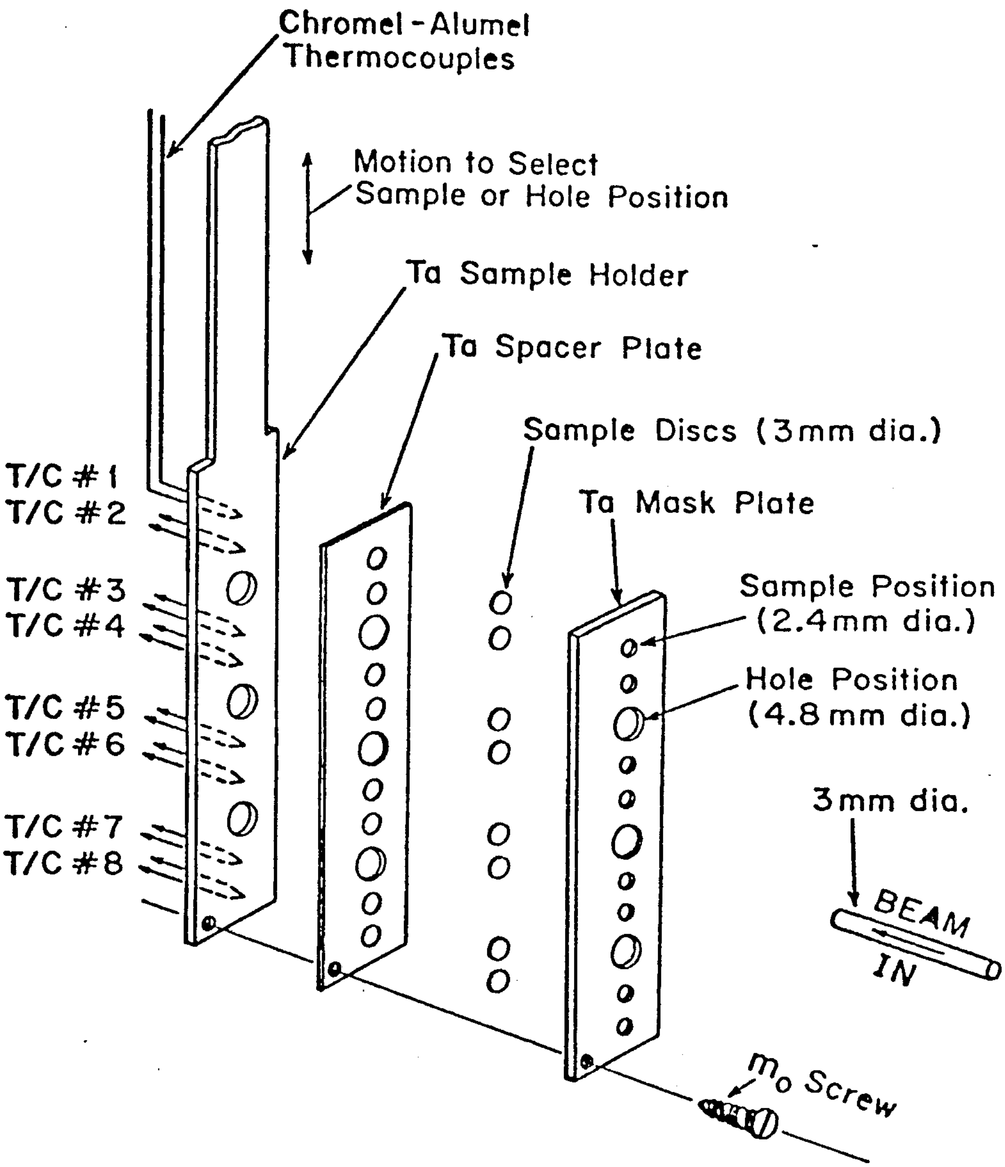

Figure IV-9. Sample holder for heavy-ion irradiation on Mo-9.1at.%Zr alloy.

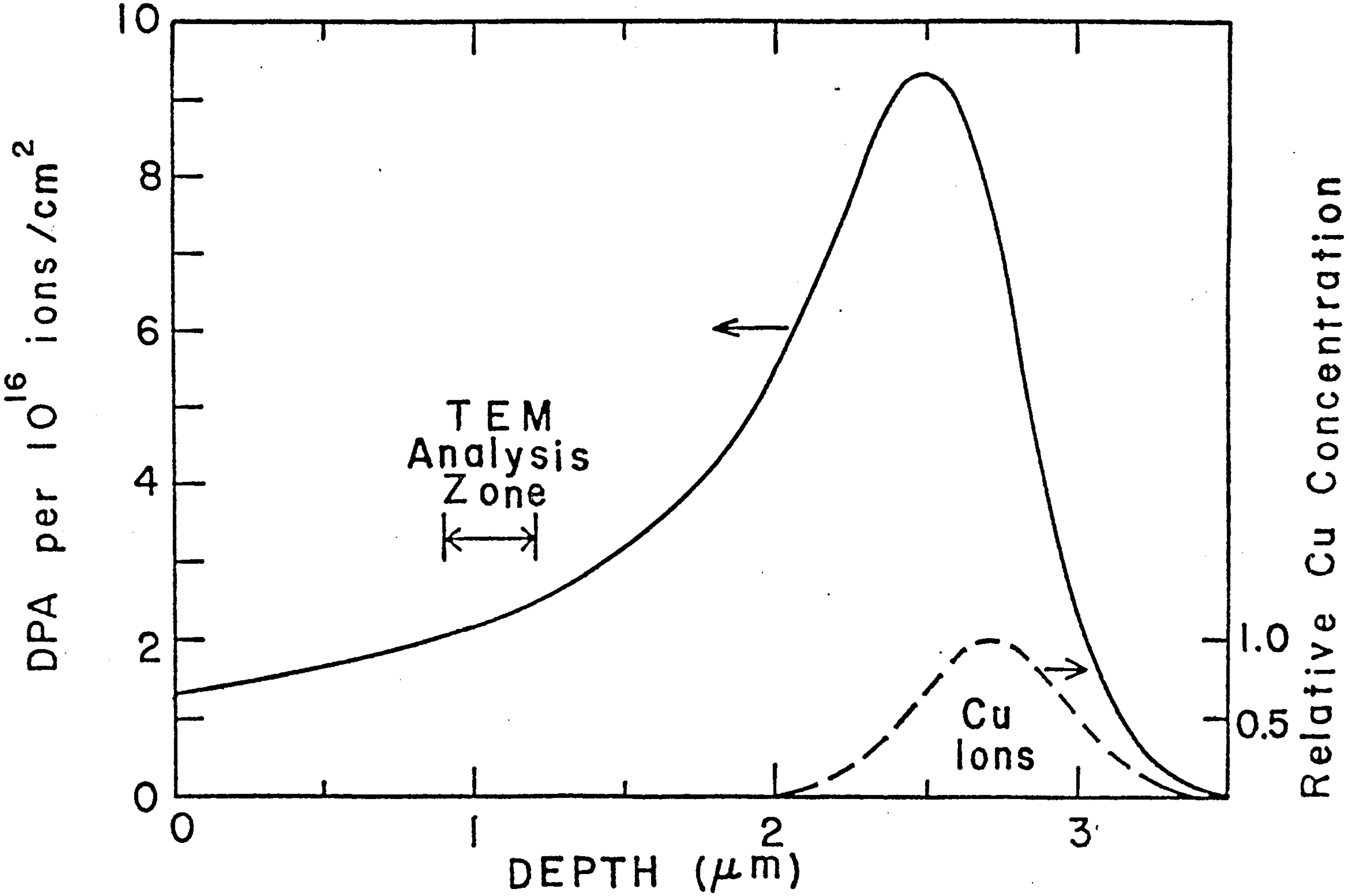

Figure IV-10. Damage vs depth curve for 17 MeV Cu on molybdenum calculated using the E-DEP-1 code of Ref. (31). Also indicated on the figure are the TEM analysis zone and the location of the deposited copper ions.

computed range of damage could be 15% smaller than the actual extent. The transmission electron microscope examination, however, was carried out in an analysis zone near 1 μm (Figure IV-10) where the slope of the damage curve or the depth dependence was smaller. A radiation enhanced diffusion calculation showed that the back diffusion of the implanted Cu ions into the TEM analysis zone was negligible in the samples examined. The dose rates in the TEM analysis zone of the irradiated samples varied from 4×10^{-4} to 8×10^{-4} dpa/sec.

C. Post-irradiation Analysis

1) Transmission Electron Microscope Sample Preparation

The range of irradiation damage in pure Mo or Mo-9.1 at.% Zr by 14-19 MeV Cu ions computed using the E-DEP-1 code of Manning and Mueller (31) was between 3 μm to 3.5 μm from the irradiated surface. Damage microstructure near 1 μm from the surface was examined in a JEOL 100B transmission electron microscope (TEM). As an example, Figure IV-10 shows the damage vs depth curve, the position of the implanted Cu ions, and the TEM analysis zone of 17 MeV Cu ion irradiated pure Mo. Similar damage vs depth curves for 18.8 MeV Cu ion irradiated Mo and 14 MeV Cu ion irradiated Mo-9.1 at.% Zr were computed using the Manning and Mueller code to determine the dpa value at the TEM analysis zone.

To prepare TEM samples, a surface layer was removed from the irradiated surface by electropolishing. The outer area of an irradiated sample was lacquered with "microstop" (Michigan Chrome and Chemical Company) to reserve an unpolished area used as a reference for determining the amount of material removed. The step height between the polished and unpolished areas was measured using an optical interference microscope. The surface layer of an irradiated pure Mo strip was removed using a 15% H_2SO_4 and 85% methyl alcohol at -20°C and 10 V. 3-mm discs were then cut from the irradiated spots. Mo-9.1 at.% Zr samples were irradiated in 3-mm discs which were polished to remove a surface layer in 12.5% H_2SO_4 and 87.5% methyl alcohol at -50°C and 20 volts. The polishing condition was adjusted such that the total polishing time to remove 1 μm was about 30 seconds, which was usually separated into two steps. The first step was a 15-sec electropolishing then measuring the amount of material removed with the interference microscope. The polishing rate in the first step measured was used to determine the polishing time in the second step under the same polishing conditions. The total amount removed in two steps was again measured using the interference microscope with an accuracy of ± 0.1 μm.

After surface removal the irradiated side of the sample was lacquered and then thinned from the other side to perforation in a Fischione jet electropolisher. Both pure Mo and Mo-9.1 at.% Zr were polished in 12.5% H_2SO_4 and 87.5% methyl alcohol at -50 ∿-55°C temperature and 70 volts. Due to the fact that alloy samples were hard and brittle, special care must be taken in handling the thin foil.

2) Transmission Electron Microscopy Procedure

The specimens were examined in a JEOL 100B electron microscope operated at 120 kV voltage. Voids were imaged under weak diffraction conditions and focused as precisely as possible to minimize the surrounding dark fringes for void size measurement. When the voids were small, however, it was desirable to use higher magnification and underfocus the voids slightly to produce a surrounding dark fringe.

Dislocations and loops were imaged under two-beam conditions with a small positive deviation from exact Bragg diffraction condition, i.e., the diffracted spot used to produce the bright field image was slightly outside the Ewald sphere in the reciprocal lattice ($s>0$). This diffraction condition under which dislocations were imaged as thin dark lines with a well defined $\vec{g}$ vector (reciprocal space vector from the transmitted spot to the diffracted spot) for data interpretation could be obtained by adjusting the positions of the Kikuchi lines on the diffraction spots. The Burgers vectors of the dislocation could then be determined using the $\vec{g} \cdot \vec{b} = 0$ criterion.

Transmission electron micrographs of voids, dislocation loops, and network dislocations were taken in different areas to observe the uniformity of their distribution. The foil thicknesses were measured using the stereo-pair technique. This was carried out by taking a pair of stereo-micrographs of the same area with identifiable structures on the top and bottom surfaces tilted symmetrically through an angle, $\pm\,\Theta$, about the horizontal foil position, then measure the parallax, P, with a stereo viewer. The foil thickness is given by

$$t = \frac{P}{2M \sin(\theta/2)} \tag{4.1}$$

where M is the magnification of the micrographs. The STEM attachment (scanning transmission electron microscope) can be used to focus the beam on a $\sim 200\text{Å}^2$ area in the foil without cooling the cold finger around the foil to produce spots of contamination on the top and bottom surfaces of the foil. This is done with the foil horizontal. Subsequent tilting through an angle ϕ separates the spots by a distance ℓ. The foil thickness is then given by the simple geometric relation

$$t = (\ell/M) \csc\phi \tag{4.2}$$

where M is the magnification of the micrograph. The loop size distributions and the void size distributions were determined using a Zeiss particle size analyser. The diameter inside of the dark fringe surrounding the void was measured (for Mo, the center of the dark fringe was used to measure the diameter). In the case of loops, the longer axis of the loop was used. The average void size and loop size are given by

$$\bar{d} = \sum_i n_i d_i / \sum_i n_i \tag{4.3}$$

and the number densities of the voids and loops are

$$\rho = \sum_i n_i/(1 - d_i/t) \quad . \tag{4.4}$$

The foil thickness is corrected to $t - d_i$ for not counting voids or loops in each size interval intersecting the foil surfaces by more than half. Assuming that voids are spherical as an approximation, the void volume fraction was computed by

$$\Delta V/V = (4/3)\pi\rho \sum_i n_i d_i^3/\sum_i n_i \quad . \tag{4.5}$$

One exception was the pure Mo sample irradiated at 1000°C. The edges of the large truncated cubic voids observed were measured and the geometry of the voids was taken into account to calculate the void volume fraction.

The composition of the two-phase Mo-9.1 at.% Zr alloy samples were measured by x-ray microanalysis using the STEM attachment to the JEOL 100B microscope. The energy spectra of x-ray emitted from atoms in the thin foil excited by the 120 KeV electron beam were recorded by a lithium drifted silicon detector. A thin film correction was used to compute the composition from the energy spectra analyzed by a multi-channel analyzer.

The Burgers vectors of dislocations were determined using the $\vec{g} \cdot \vec{b} = 0$ invisible (or residual contrast) principle. Analysis of the nature (vacancy or interstitial type) of some loops with diameters between 200 and 300 Å were carried out using the inside/outside contrast method following the principles of Maher and Eyre (97).

V. EXPERIMENTAL RESULTS

Samples of pure Mo and Mo-9.1 at.% Zr two-phase alloy were irradiated using the same irradiation facility described in Chapter IV. Defect microstructures and swelling in the alloy produced by copper ion bombardment were compared with that in pure Mo to study the effect of Zr solute addition. Phase stability of the two-phase alloy under irradiation was also investigated. The results are described here and discussed in Chapter VI.

A. Pure Molybdenum

The heavy-ion irradiation study on Mo was part of an interlaboratory correlation experiment termed "the Body-centered Cubic Ion Correlation Experiment" (98). This program was sponsored by the Materials and Radiation Effects Branch of the Division of Magnetic Fusion Energy of the Energy Research and Development Administration (ERDA) to investigate the reproducibility of the data obtained on a reference material by several laboratories using the heavy ion simulation technique.* At the University of Wisconsin, six samples of pure Mo from Pacific Northwest Laboratory were successfully irradiated and analyzed by transmission electron microscopy. The irradiation performed and the irradiation parameters of these six samples analyzed are listed in Table V-1.

---

*The participating laboratories were Argonne National Laboratory, Atomics International, Massachusetts Institute of Technology, Naval Research Laboratory, Oak Ridge National Laboratory, Pacific Northwest Laboratory, University of Cincinnati and the University of Wisconsin.

Table V-1
Samples and Irradiation Conditions for Molybdenum.

Run Number	Sample Code Number	Cu^{4+} Ion Energy (MeV)	Temperature (°C)	Vacuum (Torr)	Fluence** (10^{16} ion/cm^2)	Dose* (dpa)	Dose Rate* (dpa/sec)
1	T-40-00-2	18.8	1000	3×10^{-8}	0.58	1.3	6×10^{-4}
1	T-40-00-3	18.8	900	9×10^{-9}	0.51	1.0	6×10^{-4}
2	T-40-00-9	17.0	900	5×10^{-9}	0.95	1.9	4×10^{-4}
2	T-40-00-10	17.0	800	4×10^{-9}	1.0	2.2	3×10^{-4}
2	T-40-00-12	17.0	700	4×10^{-9}	0.45	1.0	6×10^{-4}
3	T-40-00-13	17.0	900	1×10^{-8}	7.5	19	3×10^{-4}

[*] At the region of TEM analysis (∿1μm from the sample surface).

[**] Beam uniformity ± 20%.

A temperature scan from 700°C to 1000°C was carried out for low dose samples (1∿2 dpa) to observe the temperature dependence of the formation of defect clusters. A limited dose scan from 1 dpa to 19 dpa was carried out at 900°C to observe the development of void microstructure during irradiation. The primary purpose of this study was to irradiate samples to the dose values and at the temperatures decided for the BCC Ion Correlation Program and to obtain data for damage in pure Mo as a reference to study the effect of Zr solute additions.

Voids were observed in all Mo samples irradiated in the temperature range 700°C - 1000°C. Dislocation loops were found only in the samples irradiated to ∿2 dpa at 700°C and 800°C and in the sample irradiated to 19 dpa at 900°C. A summary of the damage microstructure observed is given in Table V-2.

Figure V-1 contains a series of transmission electron micrographs of the voids formed in the Mo samples irradiated to 1.3 dpa at 1000°C, 1.9 dpa at 900°C, and 2.2 dpa at 800°C. Figure V-2 shows the dislocation structure and voids in Mo irradiated to 1 dpa at 700°C, which is near the threshold temperature for void formation. The voids in the sample irradiated at 1000°C were cubes with {100} faces and {110} facets as shown in the micrograph in Figure V-1a. The voids appeared to be more spherical at lower irradiation temperatures.

The average void size and the void number density of these low dose samples (1-2.2 dpa) are shwon in Figure V-3 as a function of irradiation temperature. The void size increased with temperature from

Table V-2

Damage microstructure in molybdenum irradiated with 17-19 MeV copper ions.

Temperature (°C)	Dose (dpa)	Average Void Size (Å)	Void Density (cm^{-3})	Void Swelling (%)	Average Loop Diameter (Å)	Loop Density (cm^{-3})	Total Disl. Density (cm^{-2})	Void Lattice Para. (Å)
1000	1.3	252	5.8×10^{14}	0.76	a	a	1×10^{9}	b
900	1.0	78	6.0×10^{15}	0.17	a	a	5×10^{9}	b
900	1.9	98	6.6×10^{15}	0.39	a	a	5×10^{9}	b
900	19	75	3.0×10^{16}	0.87	420	7×10^{12}	1×10^{9}	380
800	2.2	44	1.7×10^{16}	0.11	160	2×10^{13}	1×10^{9}	340
700	1.0	48	1.0×10^{16}	0.08	76	2×10^{15}	9×10^{9}	b

(a)- No dislocation loops observed.

(b)- Voids are randomly distributed.

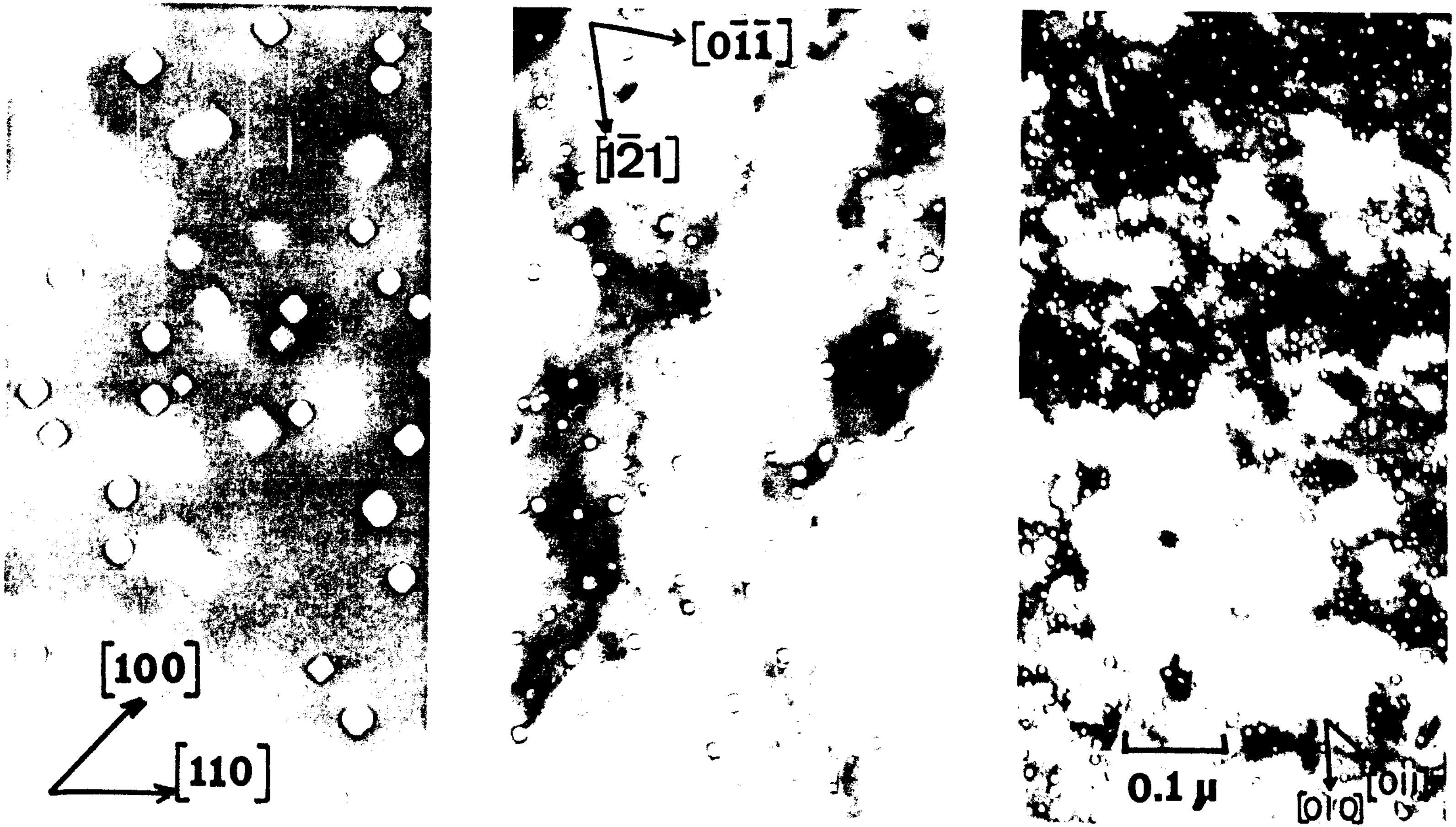

(a) **1000 °C**
1.3 dpa

(b) **900 °C**
1.9 dpa

(c) **800 °C**
2.2 dpa

Figure V-1. Voids in molybdenum irradiated with 17-19 MeV copper ions.

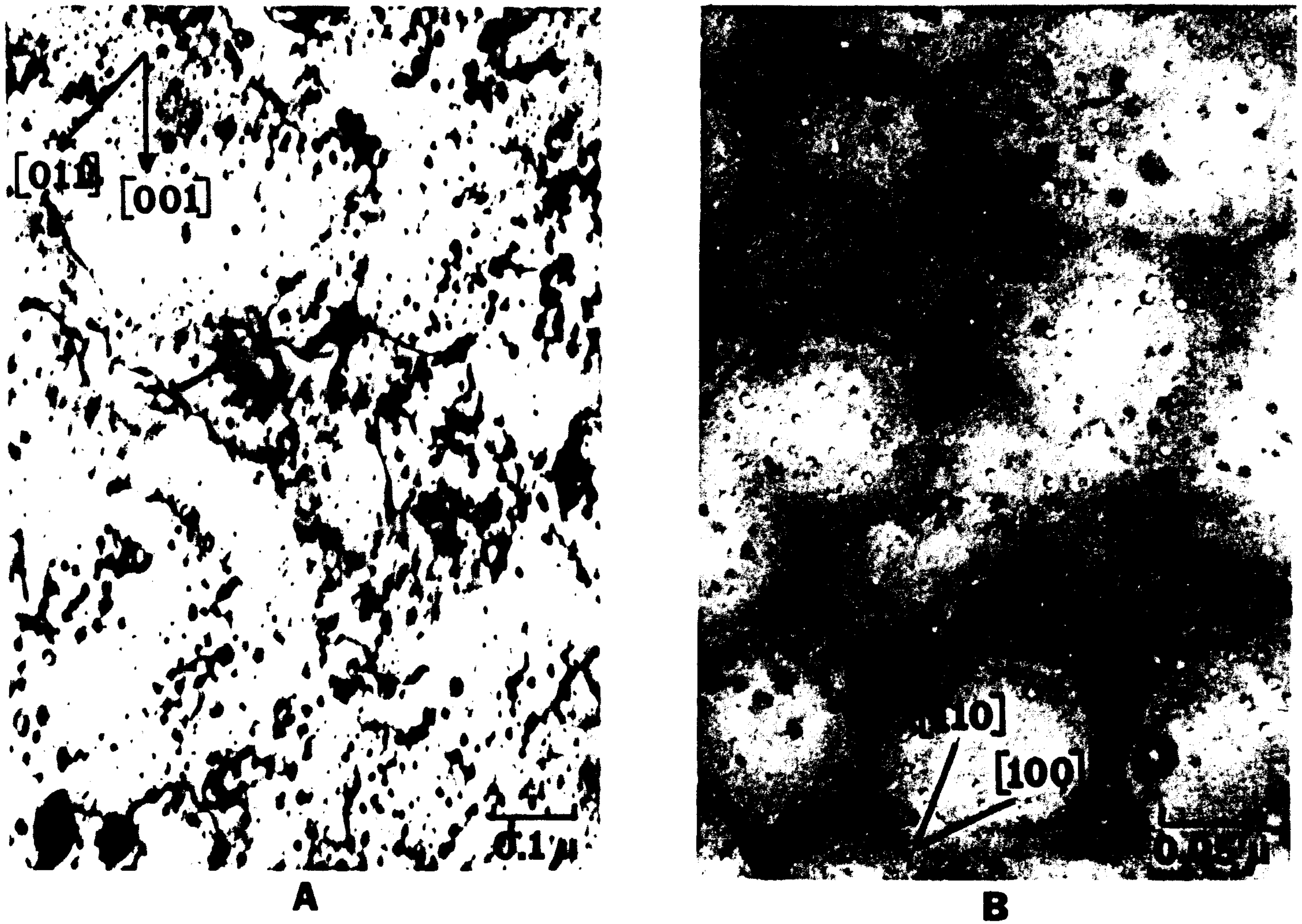

Figure V-2. Dislocation structure (A) and voids (B) in molybdenum irradiated with 17 MeV copper ions to 1 dpa at 700°C.

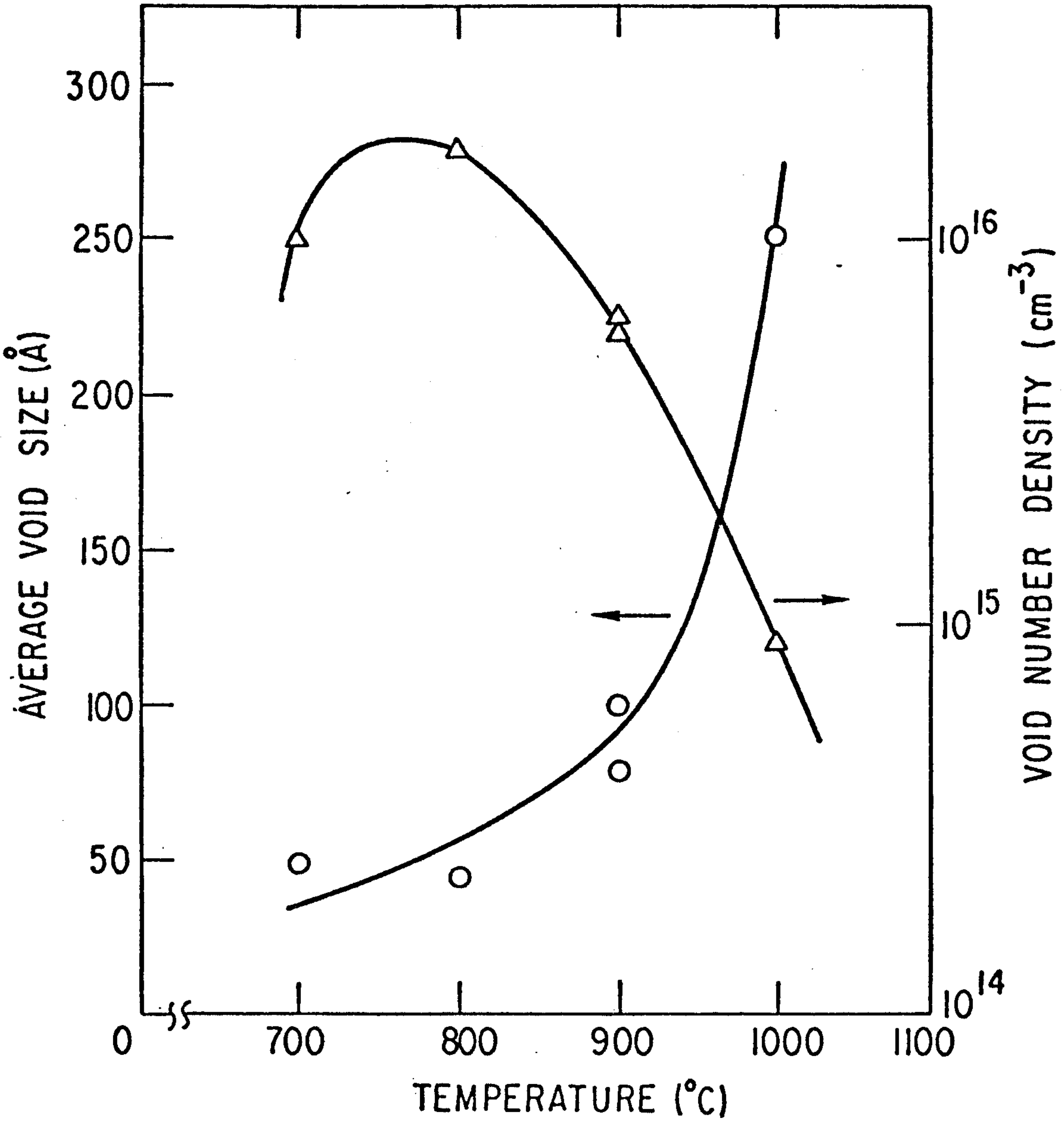

Figure V-3. Average void size and void density vs temperature for molybdenum irradiated with copper ions to 1 ∿ 2.2 dpa.

∿45 Å to ∿250 Å. At temperatures higher than ∿750°C, the void number density decreased as temperature increased. The temperature dependence of the void swelling at low dose (1-2.2 dpa) is shown in Figure V-4. A peak swelling temperature was not observed in the temperature range studied.

When Mo was irradiated to 19 dpa at 900°C, voids developed into an ordered superlattice as shown in Figure V-5b. The void superlattice was observed to be bcc parallel with the bcc crystal structure of the host metal. Void swelling increased with increasing dose at 900°C as shown in the swelling vs dose plot in Figure V-6. The average void size in the 19 dpa sample, however, was found to be smaller than that in the lower dose (1.9 dpa) sample. The larger void volume fraction at 19 dpa was due to a higher void number density than that at 1.9 dpa. A similar decrease in the void size with an increase in the void density as dose increased to a certain value in neutron irradiated molybdenum was reported by J. Bentley (79). This is probably associated with the formation of a void superlattice. Partial alignment of voids was also observed in the 800°C, 2.2 dpa sample. The void lattice spacing was ∿340 Å in the 800°C sample and ∿380 Å in the 900°C sample. A detailed discussion of the observations on void lattice formation in molybdenum will be given in Chapter VI.

Figure V-7 contains histograms of the void size distributions. The distributions in all the samples are approximately Gaussian indicating completion of nucleation in the early stages of irradiation. The voids were homogeneously distributed in all the samples except

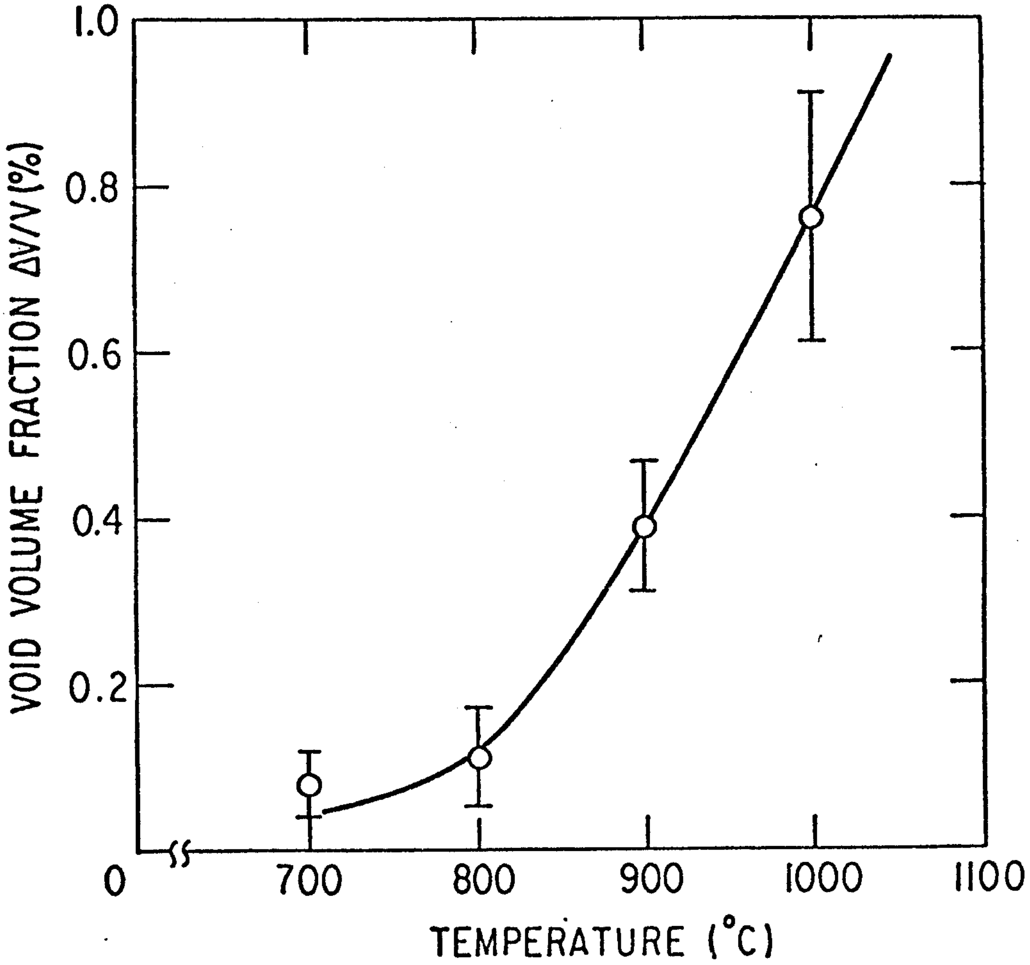

Figure V-4. Void swelling vs temperature for molybdenum irradiated with copper ions to 1 ∿ 2.2 dpa.

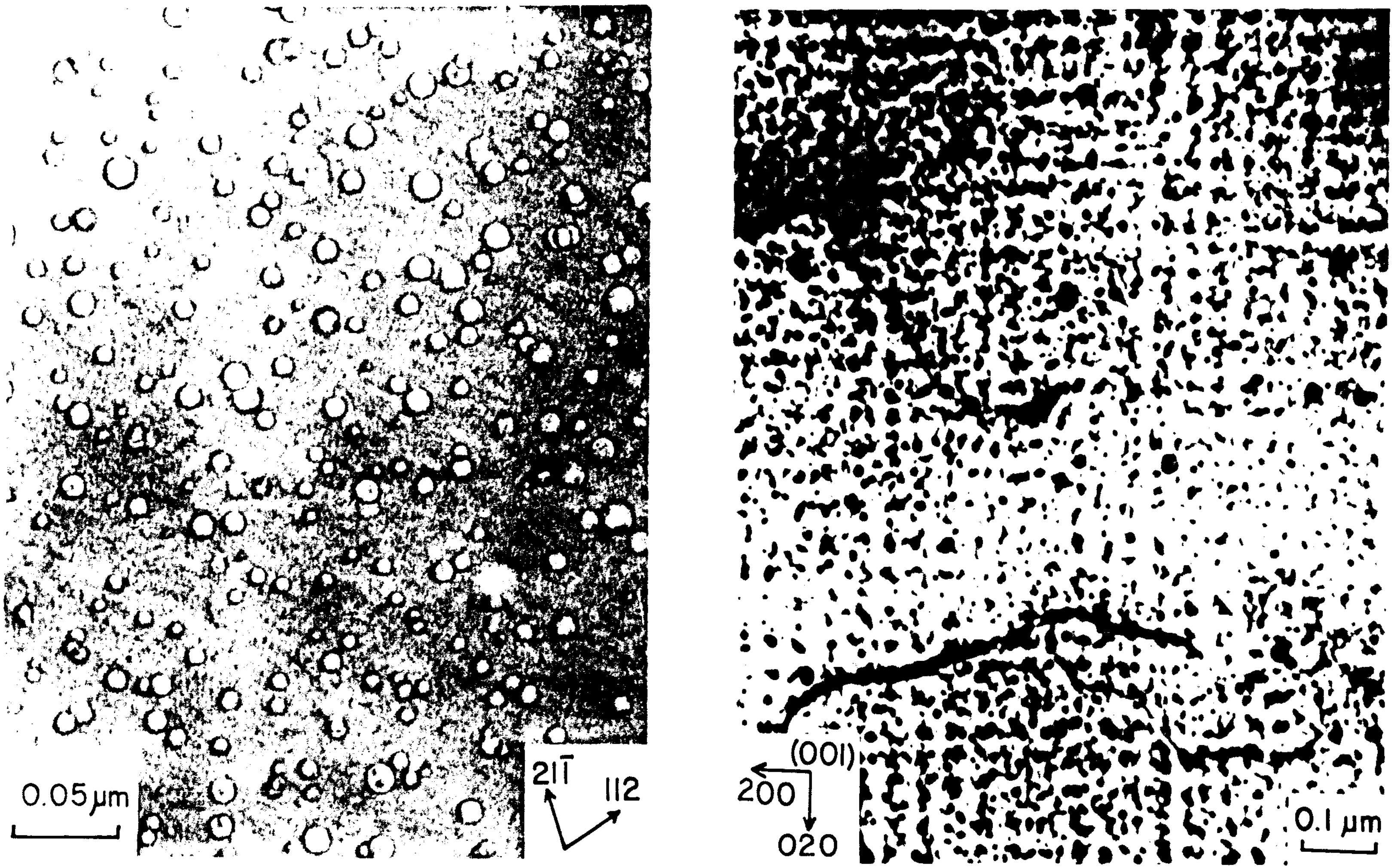

(a)

(b)

Figure V-5. Void microstructure (a) and the bcc void superlattice (b) observed in molybdenum irradiated to 19 dpa at 900°C.

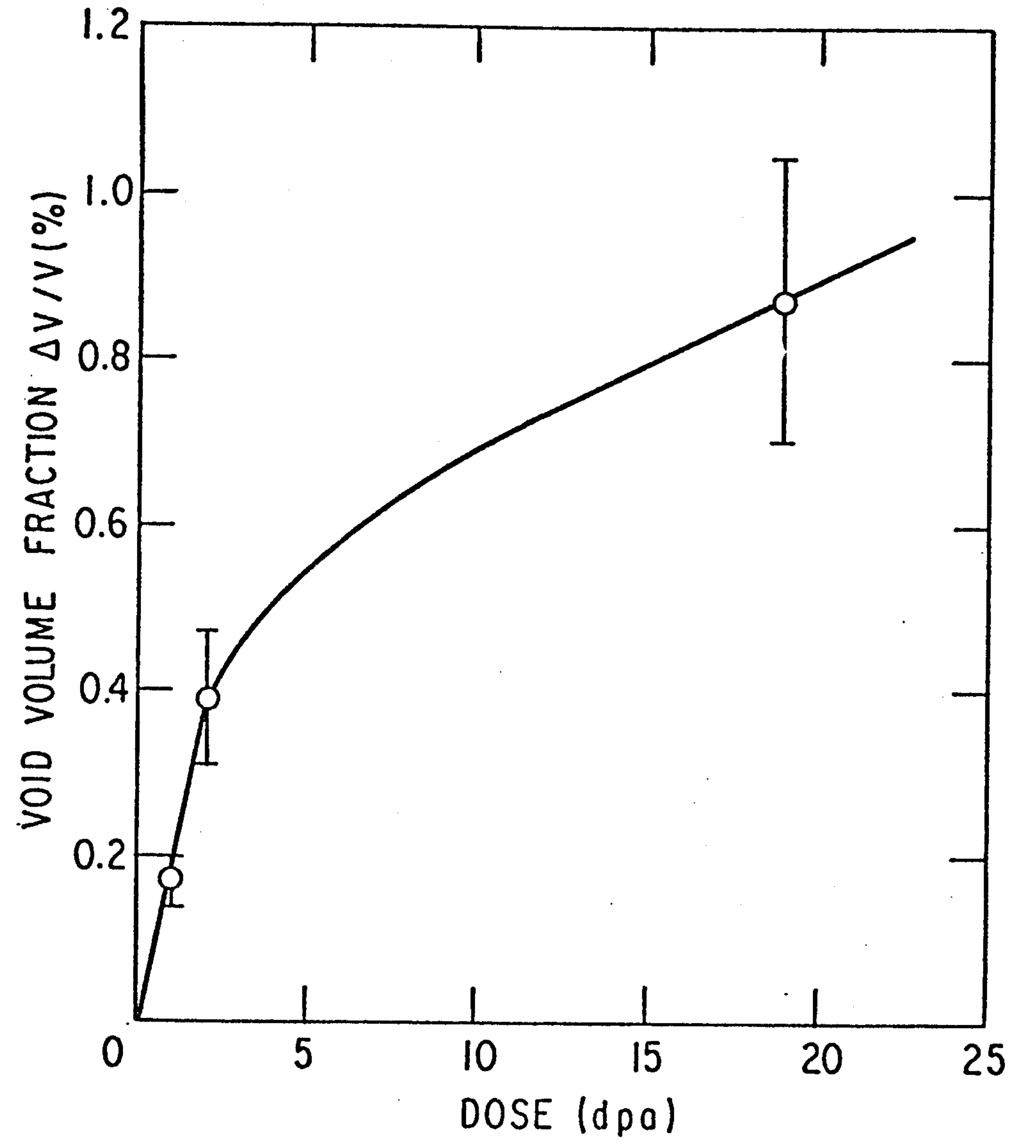

Figure V-6. Void swelling of molybdenum irradiated with 17 ∿ 19 MeV copper ions at 900°C.

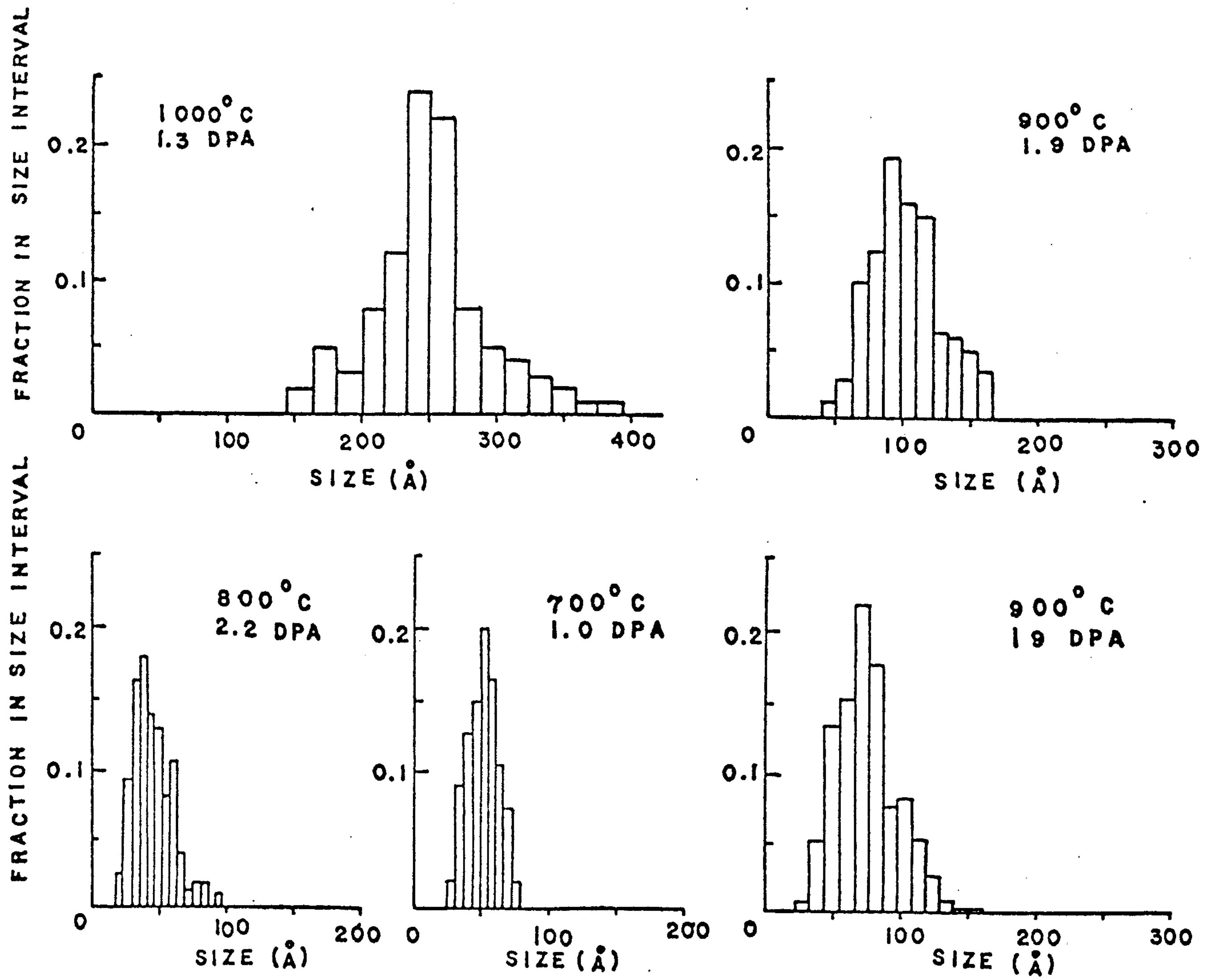

Figure V-7. Void size distributions in Mo samples irradiated with 17-19 MeV Cu ions.

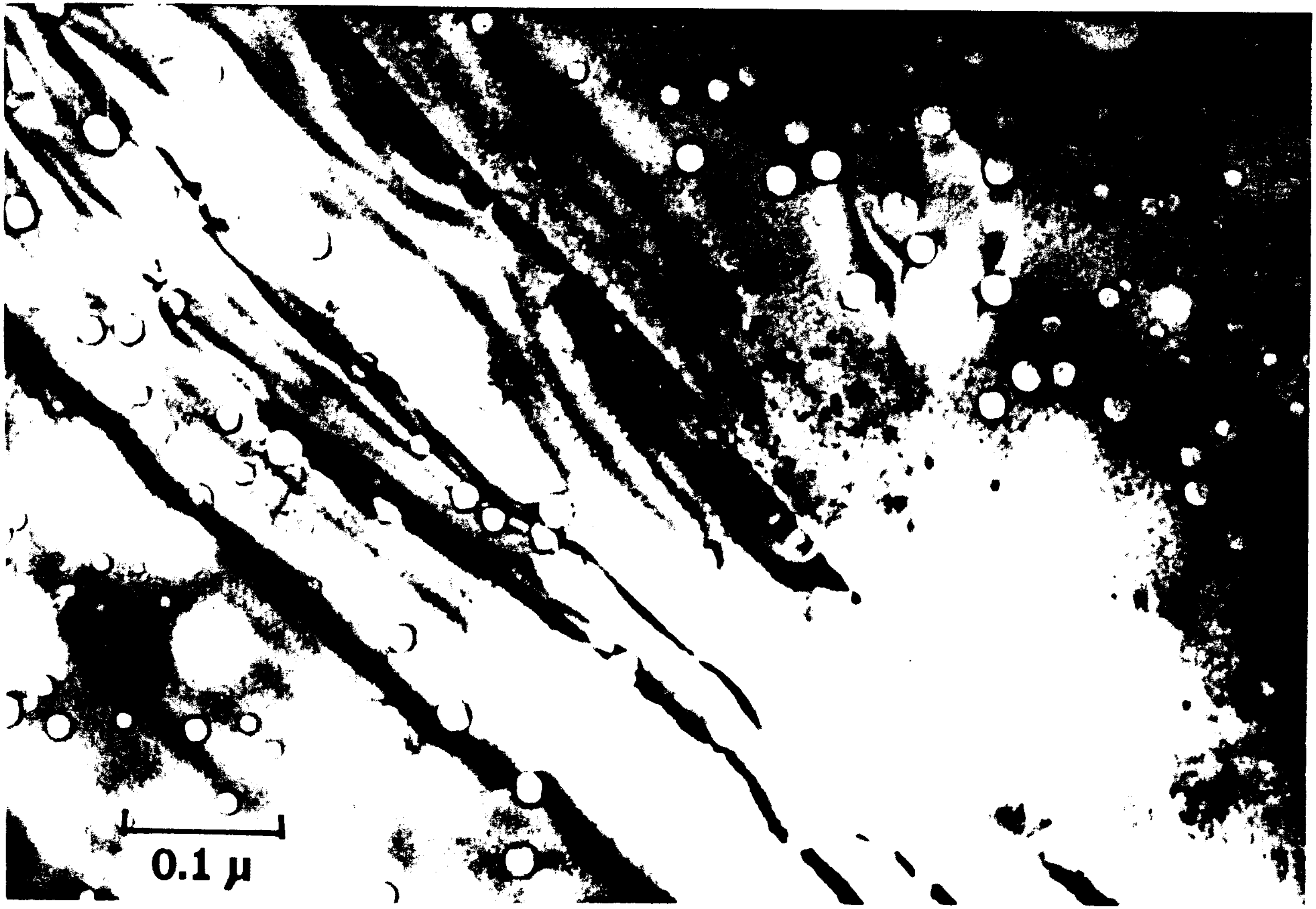

Figure V-8. Void denuding near grain boundaries in molybdenum irradiated at 900°C to 1.9 dpa.

near the grain boundaries. Some void depleted zones were observed at grain boundaries with widths varying from 300 Å to 700 Å at 900°C. One example is shown in Figure V-8. The increase in void sizes adjacent to the void depleted zone as shown in the micrograph is not clearly explained. The change in the void size is smaller for narrower depleted zones. This can be explained by differences in the effectiveness of the grain boundaries as defect sinks.

Loop and network dislocation densities observed are also given in Table V-2. The loop density decreased from $2 \times 10^{15} cm^{-3}$ at 700°C to $2 \times 10^{13} cm^{-3}$ at 800°C. At 900°C, loops were observed in the 19 dpa sample with a density of $7 \times 10^{12} cm^{-3}$. The change from voids as the major damage structure in Mo at temperatures higher than the void formation threshold, to loops near and below the threshold temperature and the formation of aggregates of small loops (Figure V-2a) are typical of ion or neutron irradiated molybdenum.

B. Mo-9.1 at.% Zr Alloy

The primary purpose of this study was to investigate the effect of the oversized Zr solute on the nucleation and growth of voids, and the phase stability of the alloy under irradiation (99). Heavy-ion bombardment was carried out at temperatures from 700°C to 900°C around the threshold temperature for void formation. The samples were pre-annealed then irradiated in the two-phase [$\gamma(Mo_2Zr)$ and bcc molybdenum solid solution] region but close to the phase boundary (Figure IV-1) so that any effects of irradiation on phase stability could be observed. A Mo-9.1 at.% Zr alloy was prepared by arc melting and heat treating in vacuum by the procedure described in Section IV-A2 to produce samples of a thermally equilibrated two-phase mixture at the irradiation temperatures. The transmission electron micrograph in Figure V-9 shows the typical pre-irradiation microstructure. γ-precipitates ($\sim$1 μm diameter) are uniformly distributed in a homogeneous matrix of Mo-rich solid solution. The dislocation density is low except for the structure dislocations at low angle grain boundaries typical of well annealed metals. The number density of γ-precipitates is small enough that a large region of matrix (Mo-7.5 at.% Zr between 700°C and 900°C) was available to observe damage structure produced by irradiation. The phase diagram (95) (Figure IV-1) indicates that the matrix contained 7.5 at.% Zr. This composition was varified using x-ray microanalysis with reasonable quantitative agreement.

Twenty-three samples were bombarded with 14 MeV Cu^{3+} ions using the U.W. tandem Van de Graaff accelerator in three irradiations. Special care was taken in sample handling because the material was hard and brittle. Eighteen samples were successfully analyzed in the JEOL 100B transmission electron microscope. The irradiation parameters of the analyzed samples are listed in Table V-3. A dose scan was carried out from 0.1 to 12 dpa at 850°C. Temperature scans from 700°C to 900°C were taken at 2 dpa and 7 dpa. Similar temperature range and irradiation parameters were chosen both for the alloy and for pure Mo to ensure comparable results. Data for the damage microstructure in the Mo-rich matrix ($\sim$Mo-7.5 at.% Zr) are summarized in Table V-4.

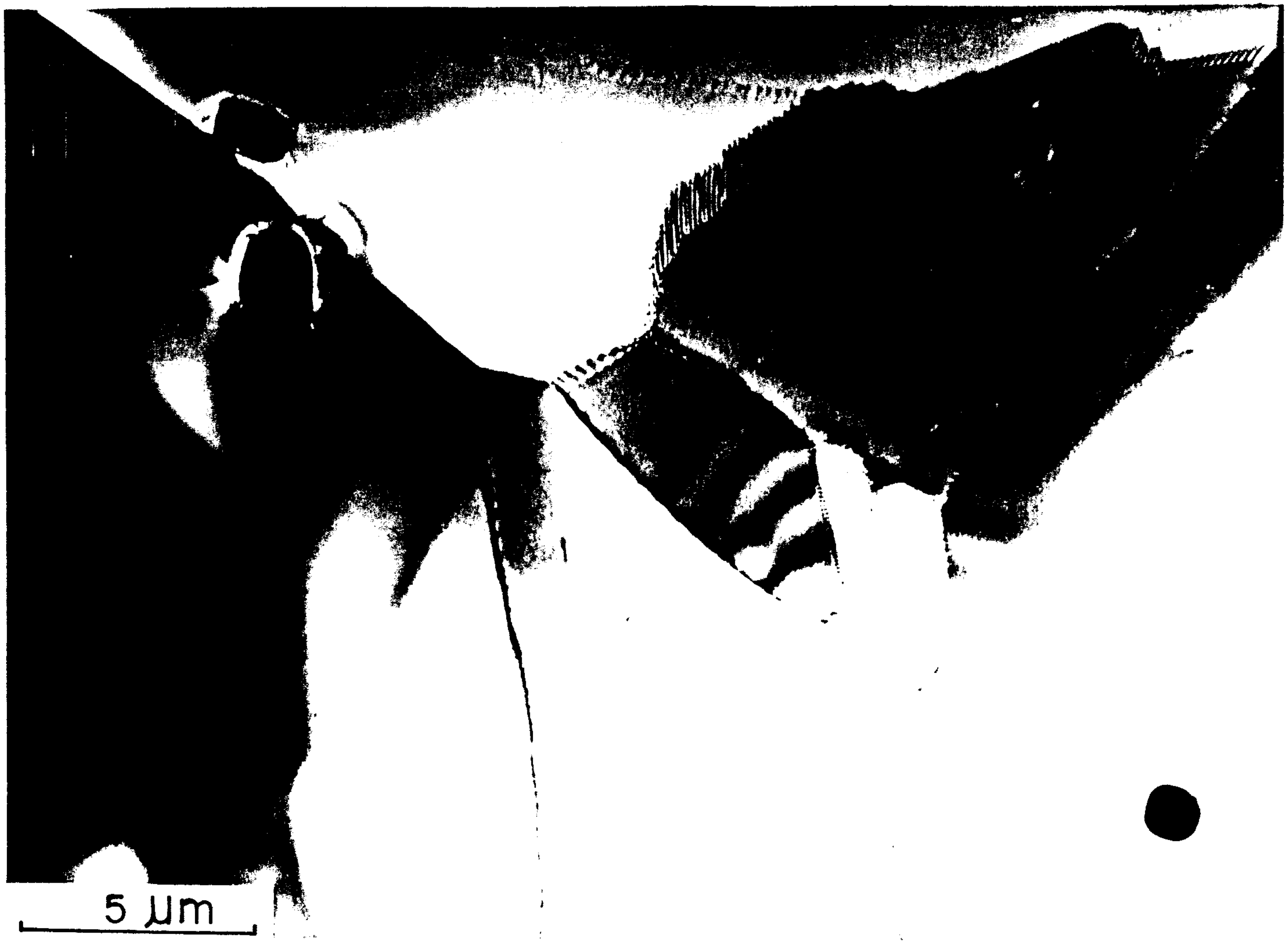

Figure V-9. Pre-irradiation microstructure of the as-annealed Mo-9.1 at.%Zr alloy.

Table V-3
Samples and irradiation conditions for Mo-9.1At.%Zr.

Run Number	Sample Code Number	Cu^{3+} Ion Energy (MeV)	Temperature (°C)	Vacuum (Torr)	Fluence* (10^{16}ions/cm^2)	Dose** (dpa)	Dose Rate** (dpa/sec)
4	T-41-00-1	14	900	1×10^{-8}	1.8	6	8×10^{-4}
4	T-41-00-3	14	900	1×10^{-8}	0.71	2	5×10^{-4}
4	T-41-00-4	14	900	1×10^{-8}	0.71	2	5×10^{-4}
4	T-41-00-6	14	700	7×10^{-9}	2.5	7	5×10^{-4}
4	T-41-00-7	14	700	7×10^{-9}	0.71	2	5×10^{-4}
5	T-41-00-9	14	800	7×10^{-9}	4.3	12	5×10^{-4}
5	T-41-00-10	14	800	6×10^{-9}	4.3	12	5×10^{-4}
5	T-41-00-11	14	800	6×10^{-9}	2.5	7	5×10^{-4}
5	T-41-00-12	14	800	5×10^{-9}	2.5	7	5×10^{-4}
5	T-41-00-13	14	800	5×10^{-9}	0.71	2	4×10^{-4}
5	T-41-00-14	14	800	6×10^{-9}	0.71	2	4×10^{-4}
5	T-41-00-16	14	800	6×10^{-9}	0.36	1	4×10^{-4}
6	T-41-00-17	14	850	1×10^{-8}	4.3	12	8×10^{-4}
6	T-41-00-19	14	850	1×10^{-8}	2.5	7	8×10^{-4}
6	T-41-00-20	14	850	1×10^{-8}	0.18	0.5	7×10^{-4}
6	T-41-00-21	14	850	1×10^{-8}	1.4	4	7×10^{-4}
6	T-41-00-22	14	850	1×10^{-8}	0.71	2	7×10^{-4}
6	T-41-00-23	14	850	1×10^{-8}	0.036	0.1	7×10^{-4}

---

*Beam uniformity ± 20%.

**At the region of TEM analysis (∿1μm from the irradiated surface).

Table V-4
Damage microstructure in Mo-9.1At.%Zr irradiated with 14 MeV copper ions.

Sample Number	Temperature (°C)	Dose (dpa)	Average Void Size (Å)	Void Density (cm^{-3})	Void Swelling (%)	Average Loop Diameter (Å)	Loop Density (cm^{-3})
1	900	6	195	2.3×10^{15}	1.4	b	$<1 \times 10^{13}$
3	900	2	45	1.3×10^{14}	0.00092	108	8.5×10^{15}
4	900	2	68	3.5×10^{14}	0.0074	116	7.7×10^{15}
6	700	7	a	a	0	53	1.1×10^{16}
7	700	2	a	a	0	59	1.5×10^{16}
9	800	12	99	7.2×10^{14}	0.056	115	1.3×10^{16}
10	800	12	85	2.8×10^{14}	0.012	84	7.5×10^{15}
11	800	7	a	a	0	81	1.4×10^{16}
12	800	7	99	1.3×10^{14}	0.0082	98	1.0×10^{16}
13	800	2	a	a	0	70	1.6×10^{16}
14	800	2	a	a	0	93	1.2×10^{16}
16	800	1	a	a	0	78	1.8×10^{16}
17	850	12	236	2.1×10^{15}	1.7	b	$<1 \times 10^{13}$
19	850	7	153	1.7×10^{15}	0.43	b	$<1 \times 10^{13}$
21	850	4	80	1.4×10^{15}	0.047	155	9.5×10^{14}
22	850	2	a	a	0	122	9.6×10^{15}
20	850	0.5	a	a	0	127	7.2×10^{15}
23	850	0.1	a	a	0	78	3.2×10^{15}

[a] No voids detected.

[b] Loops were replaced by network dislocations of densities $\sim 2 \times 10^{10} cm^{-2}$.

1) Void and Dislocation Structure

No voids were observed in samples irradiated at 700°C up to 7 dpa. A high density of dislocation loops ($\sim 1 \times 10^{16} \mathrm{cm}^{-3}$) was produced by irradiation. Small dislocation loops (<100 Å) are observable as "black spots" when they are imaged under kinematical diffraction conditions. Under dynamical conditions, however, small loops near the foil surface exhibit black-white contrast (100,101). This is shown in Figure V-10 in a transmission electron micrograph of loops at a bend contour where the contrast condition varies from dynamical condition at the center of the foil to kinematical condition at either side. Figure V-11 shows the typical damage structure in the samples irradiated at 700°C. Although some loops grew into network dislocations from 2 dpa to 7 dpa, new loops were still nucleating; therefore, the average loop diameter and the number density remained nearly the same.

At 800°C, voids were observed only at 7 dpa and above. Voids were observed in one of the two duplicate samples irradiated to 7 dpa but were not found in the other sample. Since the swelling value of the sample with voids was small (0.0082%), this was caused by the ± 20% uncertainity in the dpa value due to the beam uniformity and the uncertainity in the surface removal of the samples. Approximately 6 dpa is required for void nucleation at 800°C. Figure V-12a shows voids in the 800°C, 12 dpa sample imaged under weak diffraction conditions while V-12b shows loops in the same area of the sample imaged under two-beam condition. Figure V-13 contains a series of micrographs

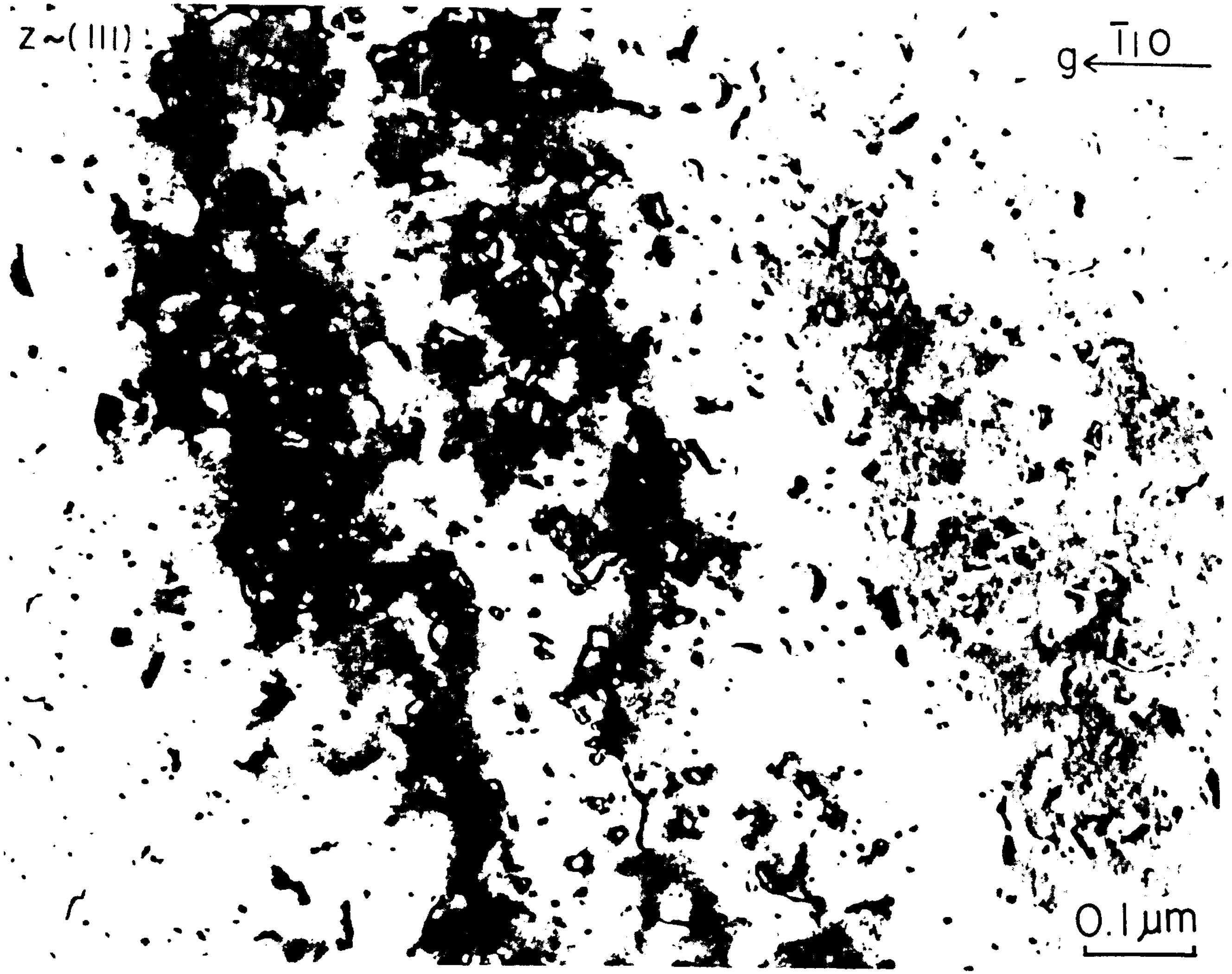

Figure V-10. Dislocation loops under different contrast conditions at a bend contour in Mo-9.1 at.%Zr irradiated to 7 dpa at 700°C with 14 MeV copper ions.

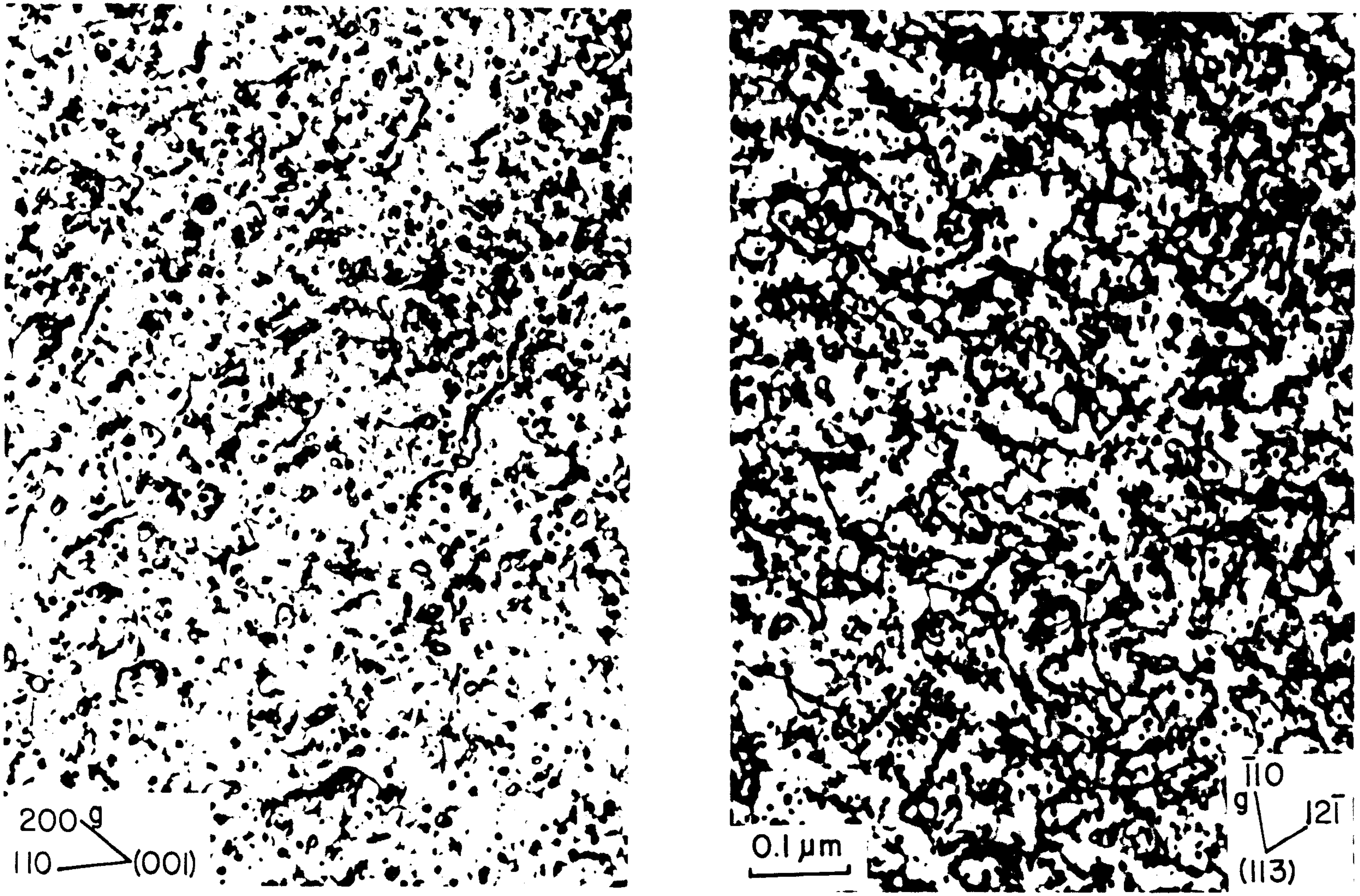

(a) 2 dpa (b) 7 dpa

Figure V-11. Dislocation loops and networks in Mo-9.1 at.%Zr irradiated with 14 MeV copper ions at 700°C.

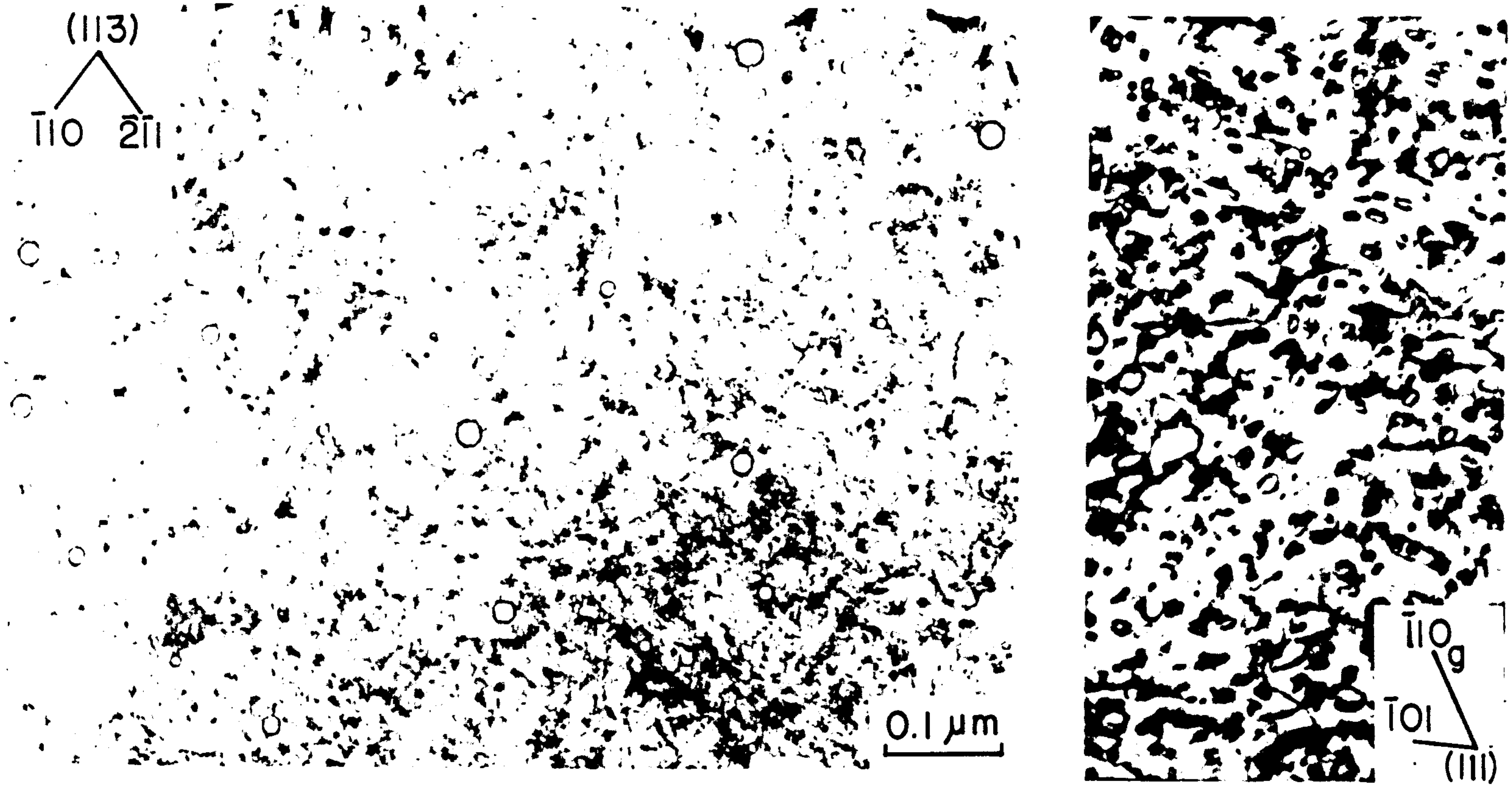

(a) Voids

(b) Loops

Figure V-12. Voids (a) and dislocation loops (b) in the same area of the Mo-9.1 at.%Zr sample irradiated at 800°C to 12 dpa.

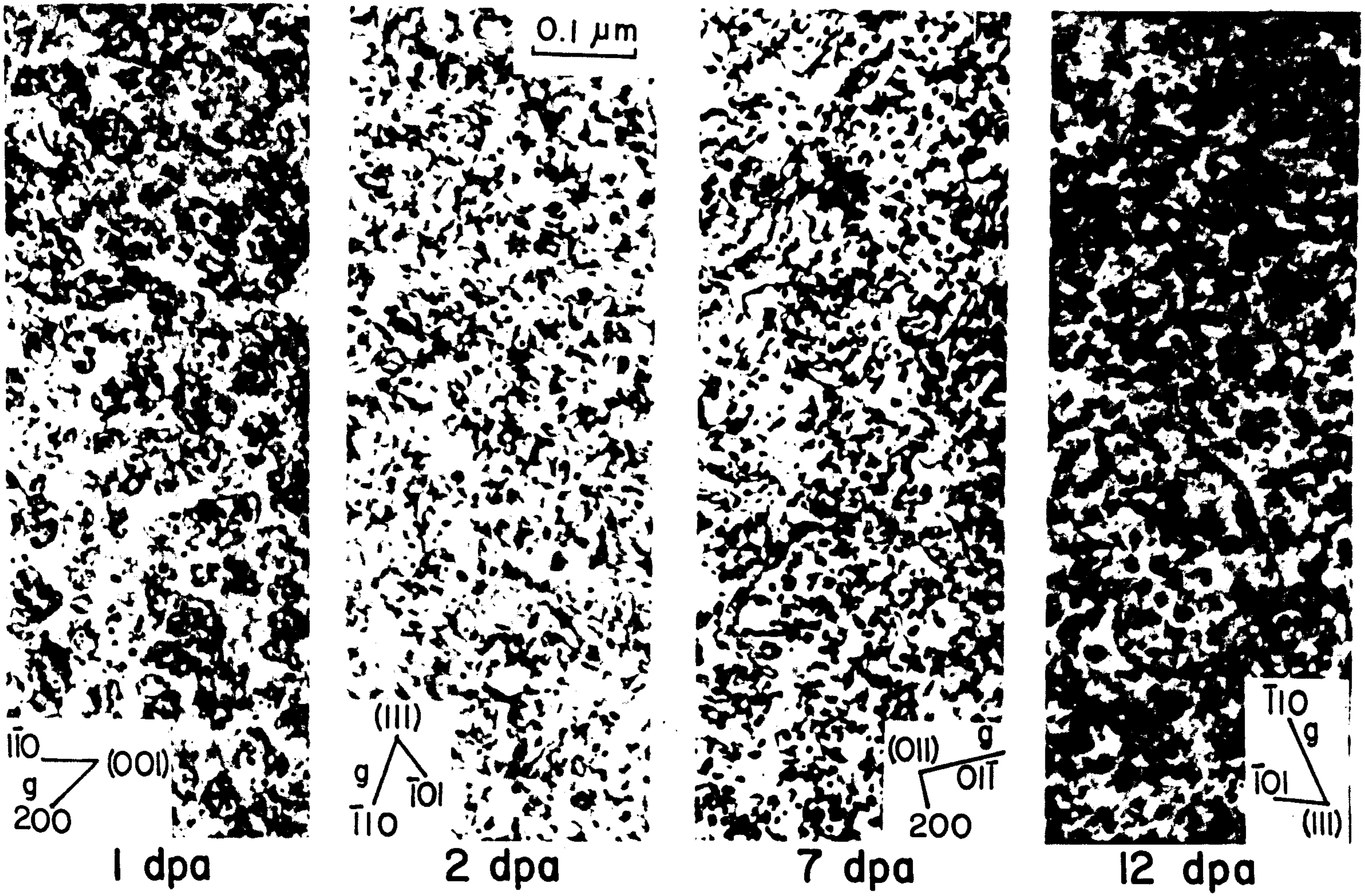

Figure V-13. Microstructure development in Mo-9.1 at.%Zr irradiated with 14 MeV copper ions at 800°C. Voids were observed at dose $\geq$ 7 dpa.

showing dislocation structures in Mo-9.1 at.% Zr irradiated at 800°C to doses from 1 dpa to 12 dpa. The average loop diameter increased slightly from ∿75 Å at 1 dpa to ∿100 Å at 12 dpa due to the growth of loops into networks while new loops were nucleating. The variation in loop densities around 1 x 10^{16}cm^{-3} was within experimental error (± 15% uncertainty in foil thickness and ± 5% in the magnifications of micrographs).

A dose scan from 0.1 dpa to 12 dpa at 850°C showed that loops formed in the early stage of irradiation grew mostly into network dislocations at 7 dpa. Nucleation of loops became negligible at 7 dpa and above. The loop density increased from 3.2 x 10^{15}cm^{-3} at 0.1 dpa to 9.6 x 10^{15}cm^{-3} at 2 dpa then dropped to 9.5 x 10^{14}cm^{-3} as shown in the density vs dose curve in Figure V-14a. Almost all the loops grew into network dislocations giving line densities of ∿2 x 10^{10}cm^{-2} at 7 dpa and above while the loop number densities became negligible ($<10^{13}$cm^{-3}). The increase in the average loop diameter with dose is also shown in Figure V-14a. Voids were observed only in the 4 dpa, 7 dpa, and 12 dpa samples irradiated at 850°C. The incubation dose for void nucleation was estimated to be 3 dpa. Though void nucleation became difficult with the addition of 7.5 at.% Zr to Mo (the saturated solid solution), void growth rate became faster than in pure Mo once voids were nucleated. Figure V-15 contains a series of micrographs showing the development of damage microstructure in the alloy during irradiation at 850°C.

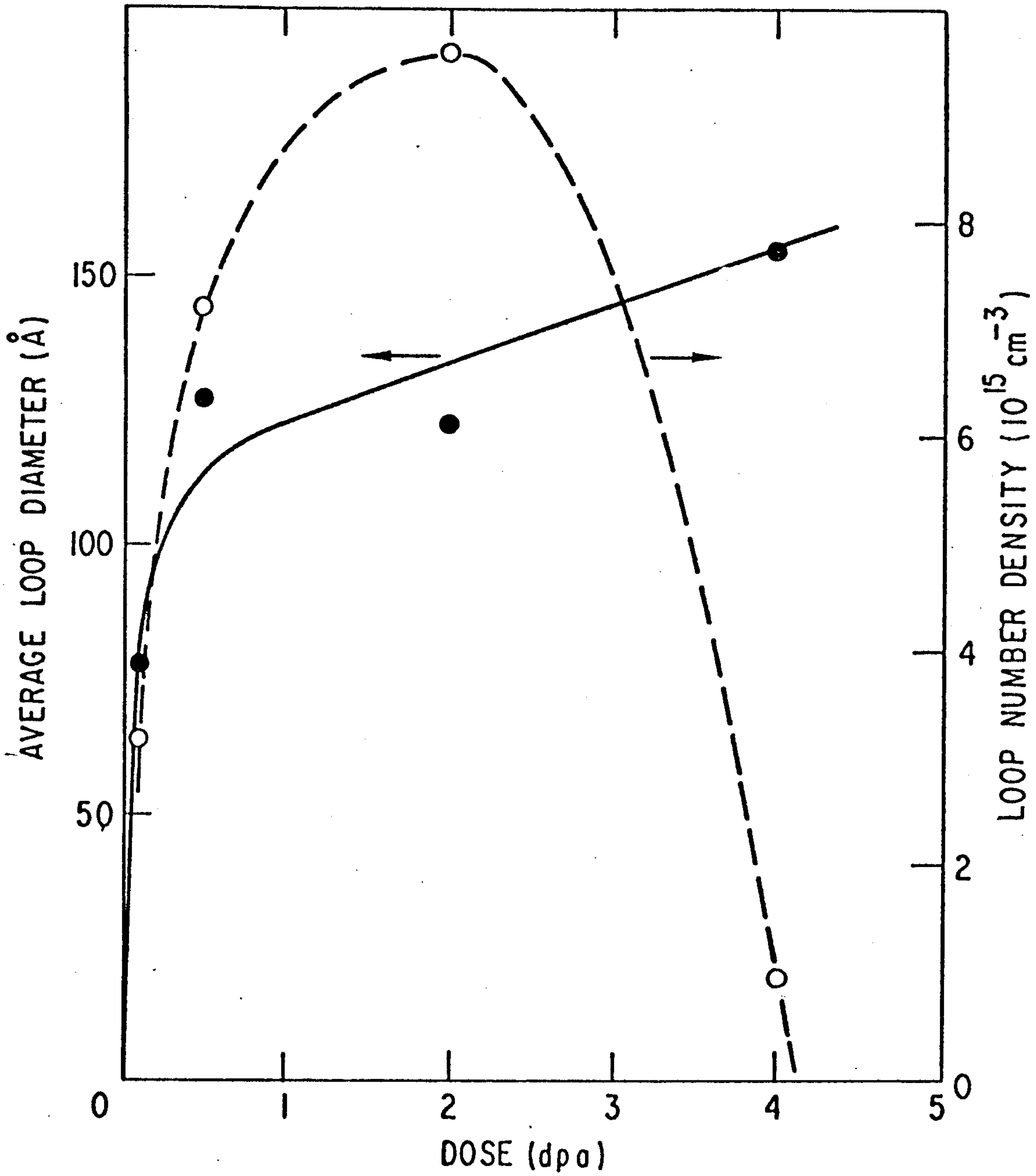

Figure V-14a. Average loop diameter and loop density vs dose for Mo-9.1at.%Zr irradiated with 14 MeV copper ions at 850°C.

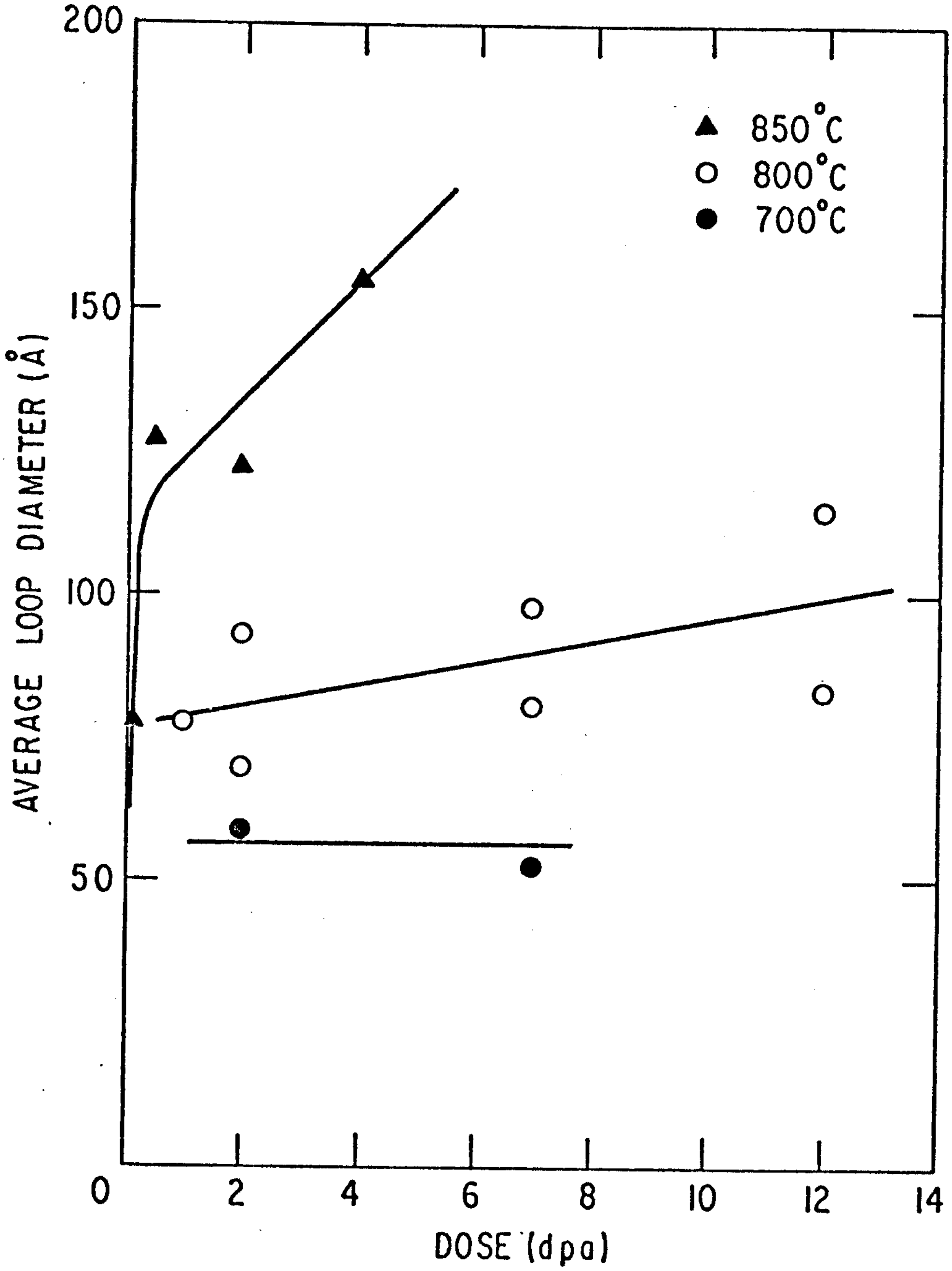

Figure V-14b. Average loop diameter vs dose for Mo-9.1at.%Zr irradiated with 14 MeV copper ions.

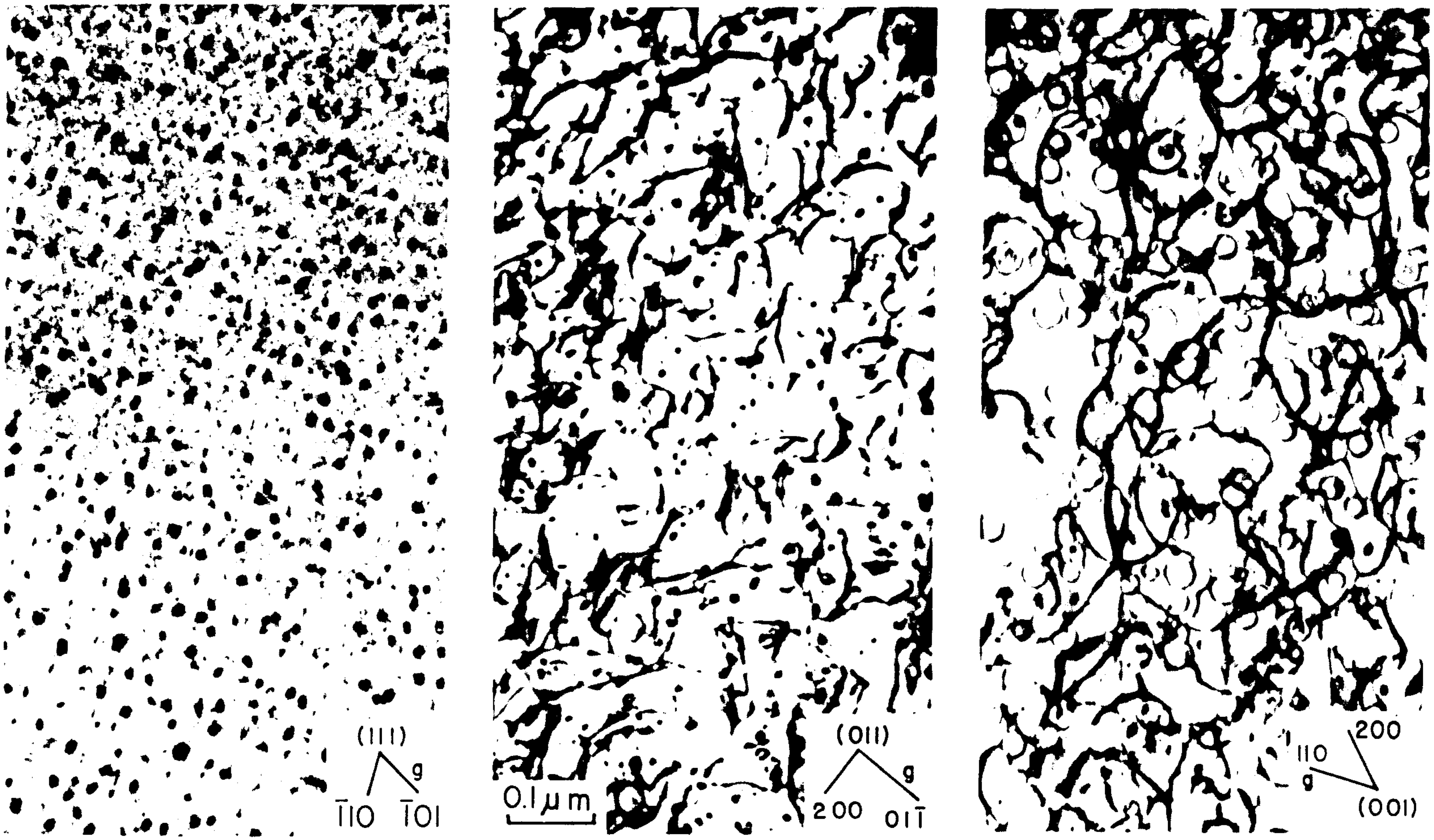

0.1 dpa 4 dpa 12 dpa

Figure V-15. Microstructure development in Mo-9.1 at.%Zr irradiated with 14 MeV copper ions at 850°C. Voids were observed at dose $\geq$ 4 dpa.

Although the dose dependence of the average loop diameter is dependent on the nucleation rate of new loops and the rate at which large loops intersect and become part of the network, the average loop diameter vs dose data are shown in Figure V-14b. In general, the loop growth rate increases and the dose at which loop nucleation is complete decreases as temperature increases. The incubation dose for void nucleation also decreases with increasing temperature. This temperature effect is clearly illustrated by samples irradiated to 2 dpa and 6 dpa at 900°C. Voids at a density of $\sim 2.5 \times 10^{14} \mathrm{cm}^{-3}$ were found in the 2 dpa sample. The void density increased by an order of magnitude ($2.3 \times 10^{15} \mathrm{cm}^{-3}$) at 6 dpa and nucleation still continued. The average void size increased from ∿55 Å at 2 dpa to ∿200 Å at 6 dpa. This is shown in the micrographs in Figure V-16. Small voids observed in the 2 dpa, 900°C sample are shown in Figure V-17a, while the sample is imaged under two-beam conditions in Figure V-17b to show dislocation structure in the same area of the sample. Figure V-18 is a micrograph of the 900°C, 6 dpa sample at lower magnification showing voids and tangled dislocations developed from uniformly distributed loops at lower dose.

The dramatic temperature effect on the microstructural development is shown in the micrographs in Figure V-19 of samples irradiated to ∿7 dpa at 700°C, 800°C, and 900°C. Void size and void density data are given in Figure V-20. No voids were observed at 700°C up to 7 dpa. The incubation doses necessary to observe voids were estimated to be 6 dpa at 800°C, 3 dpa at 850°C and 1.5 dpa at 900°C in contrast

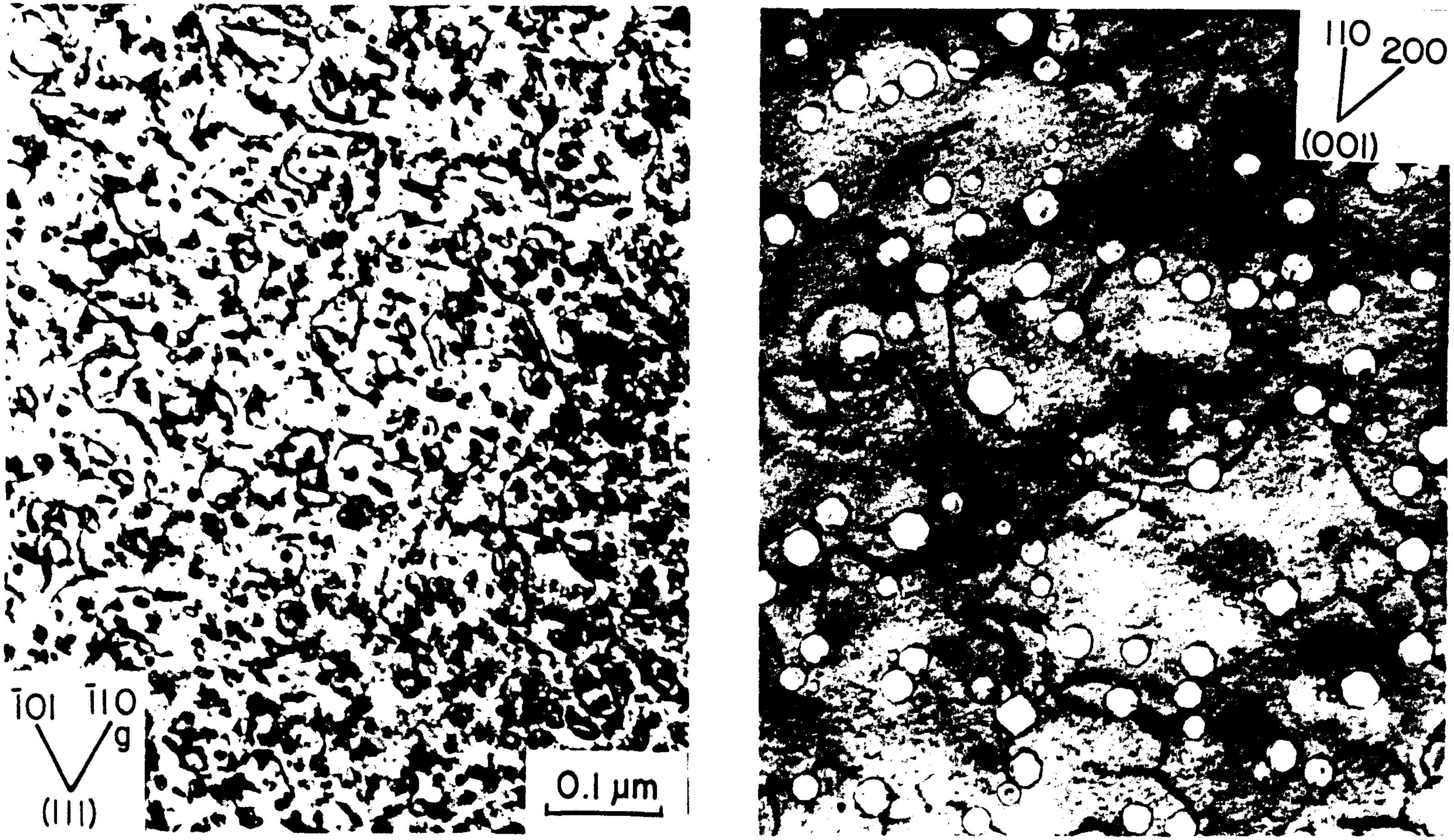

Figure V-16. Microstructure development in Mo-9.1at.%Zr irradiated with 14 MeV copper ions at 900°C.

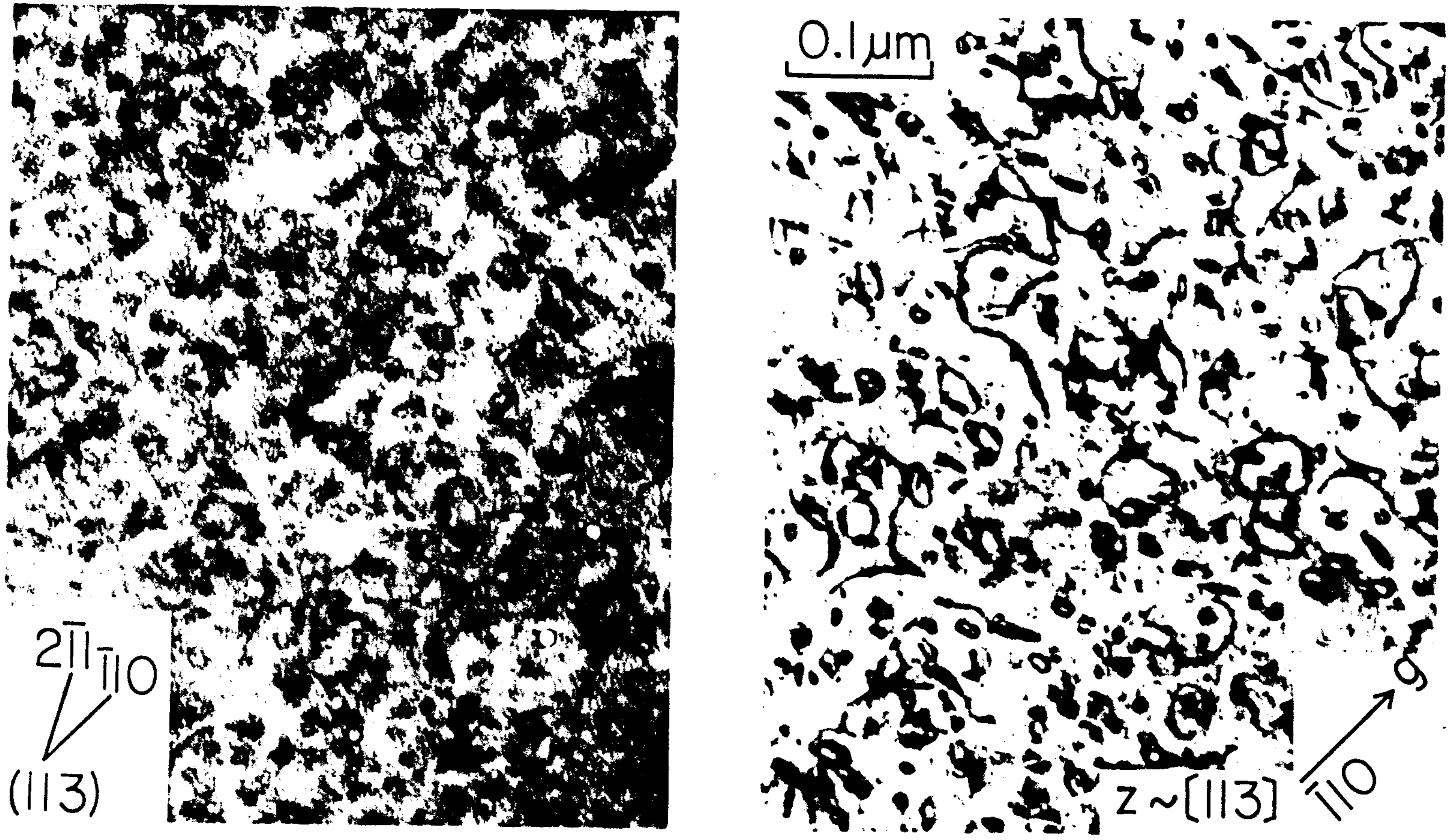

(a) Voids

(b) Dislocation Loops

Figure V-17. Voids (a) and dislocation loops (b) in the same area of the Mo-9.1 at.%Zr sample irradiated to 2 dpa at 900°C.

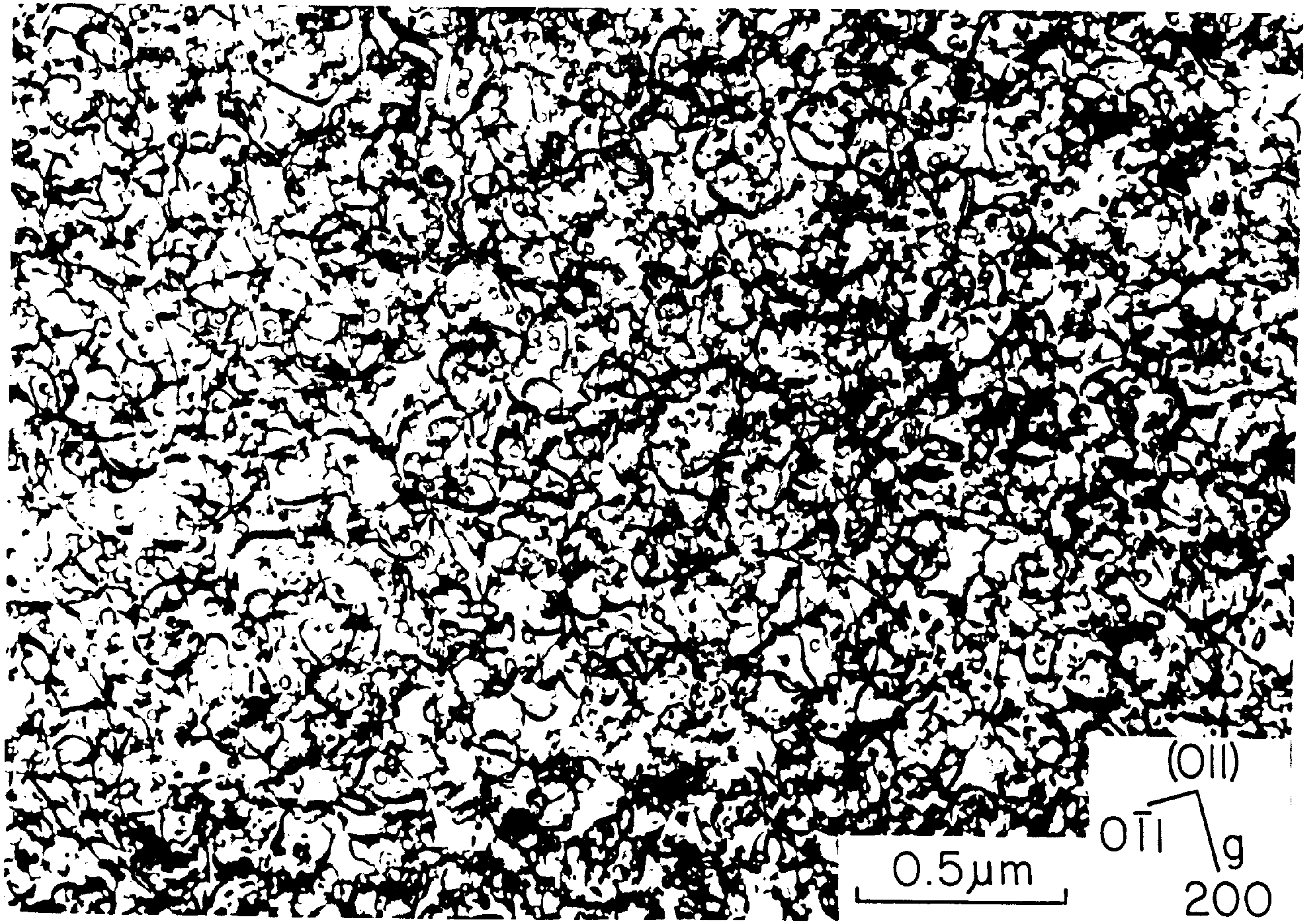

Figure V-18. Typical damage microstructure of voids and dislocations in Mo-9.1 at.%Zr irradiated at 900°C to 6 dpa with 14 MeV copper ions.

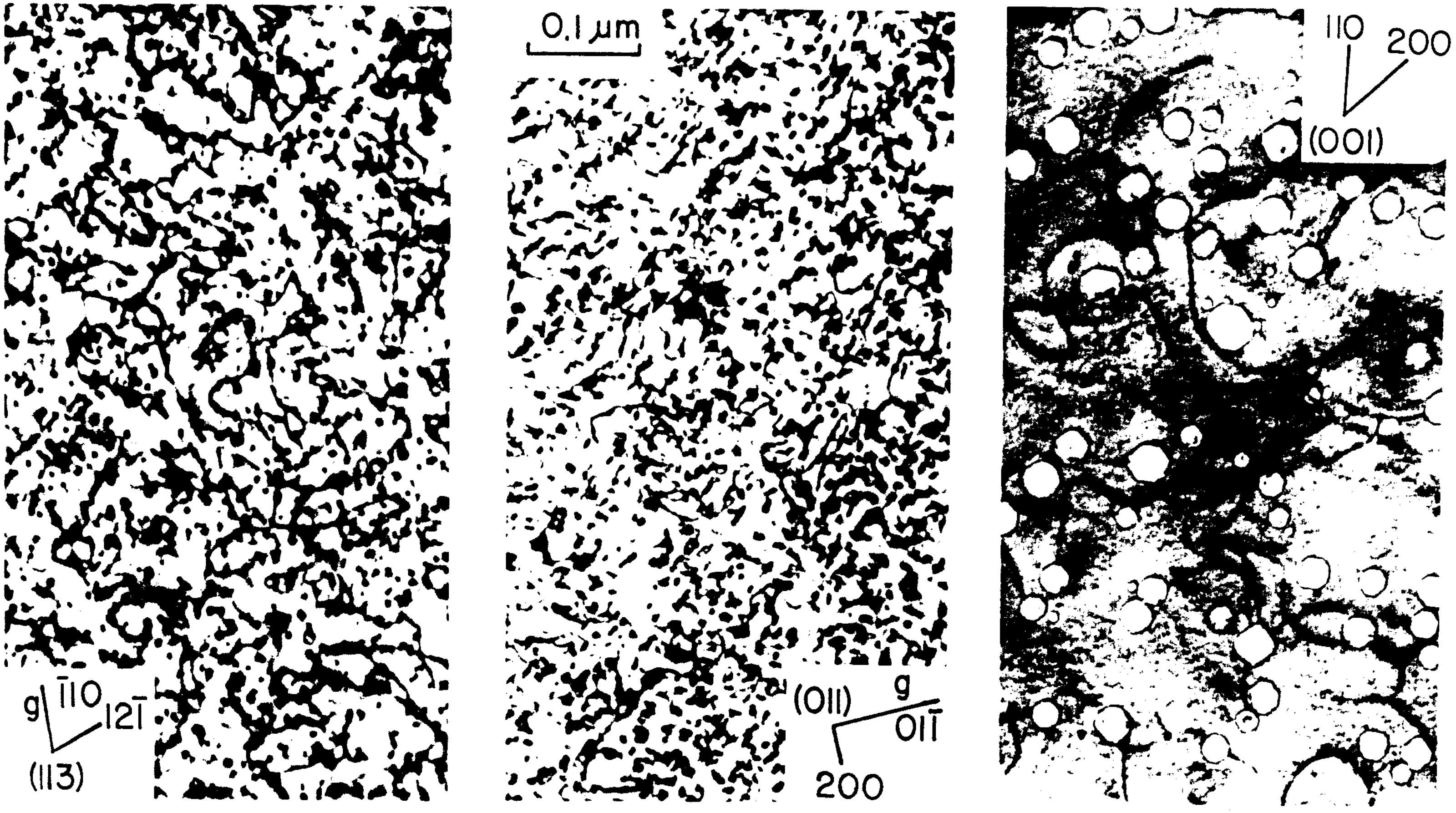

(a) 700°C (b) 800°C (c) 900°C

Figure V-19. Temperature dependence of defect microstructure in Mo-9.1 at.%Zr irradiated with 14 MeV copper ions to ∿7 dpa.

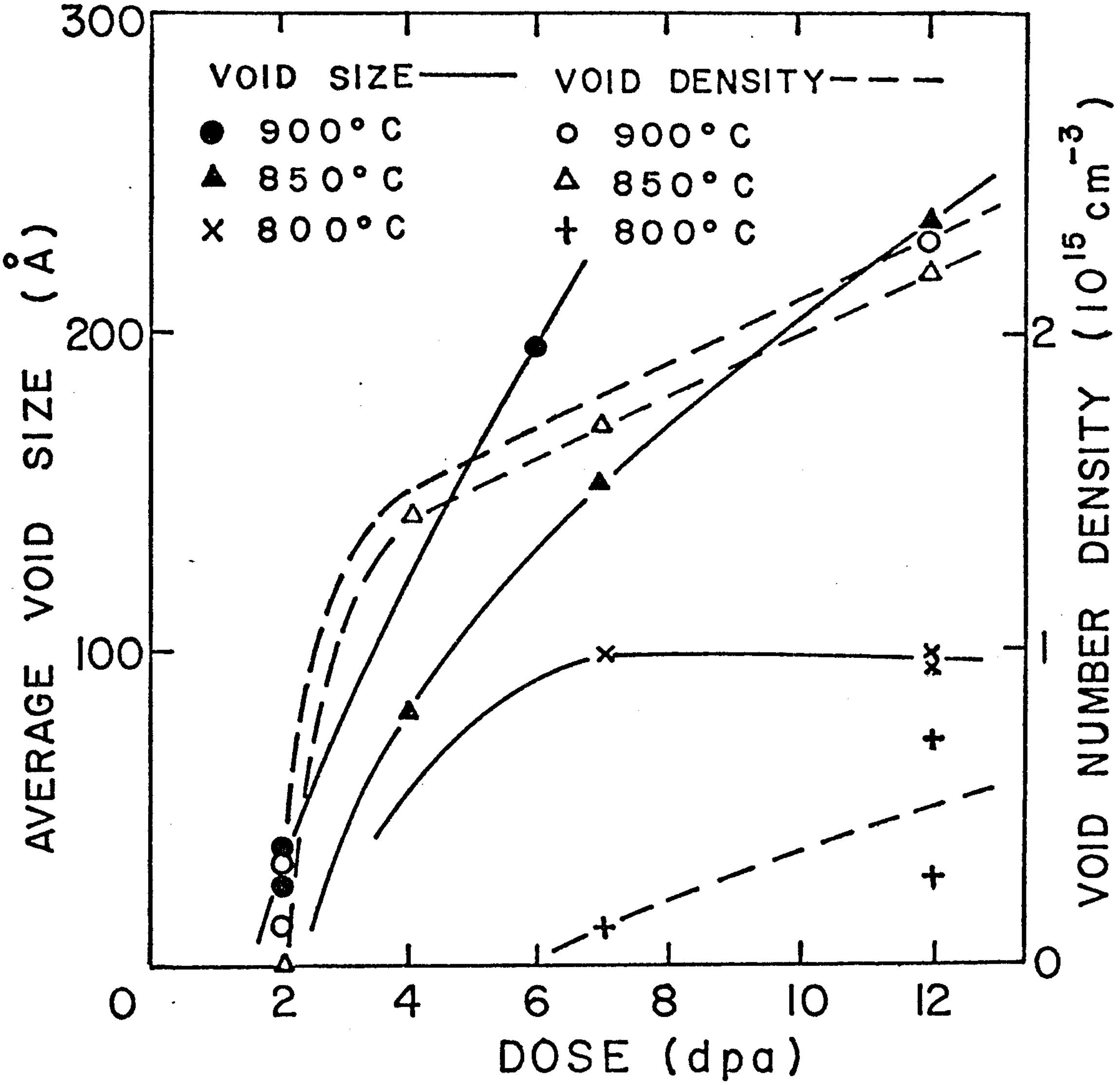

Figure V-20. Void density and average diameter vs dose for Mo-9.1at.%Zr irradiated with 14 MeV copper ions.

to the very short incubation dose in pure Mo. Void nucleation periods were long in the alloy. The saturation of the average void size vs dose curve for the irradiation at 800°C between 7 and 12 dpa is due to the continuation of void nucleation. Void swelling data in the alloy are shown in Figure V-21. Swelling in pure Mo irradiated at 900°C using the same facility is also shown in the figure. Although swelling in the alloy was reduced at lower doses or lower temperatures, the high growth rate observed resulted in larger swelling than Mo at higher doses.

The void size distributions are shown in the number density per size interval vs void size plots in Figures V-22a and b. Measurements of diameters of voids near 20 Å are not accurate and voids smaller than that are not resolved in the microscope. This happened in the case of the samples irradiated at 800°C up to 12 dpa and at 900°C to 2 dpa as can be seen in Figure V-22a. The void number densities in these samples are therefore underestimated and the average void size are overestimated. Continuation of void nucleation and growth in samples irradiated at 850°C to doses from 4 dpa to 12 dpa while a decrease in the nucleation rate from 7 dpa to 12 dpa can be seen in Figure V-22b.

The addition of Zr to Mo promoted dislocation loop formation. Analysis of the loop nature was difficult because of the high loop densities and the small loop sizes. Though the number of loops in the foil was smaller at thinner areas near the edge of the hole which made the identification of loops easier, the foil was quickly bent by

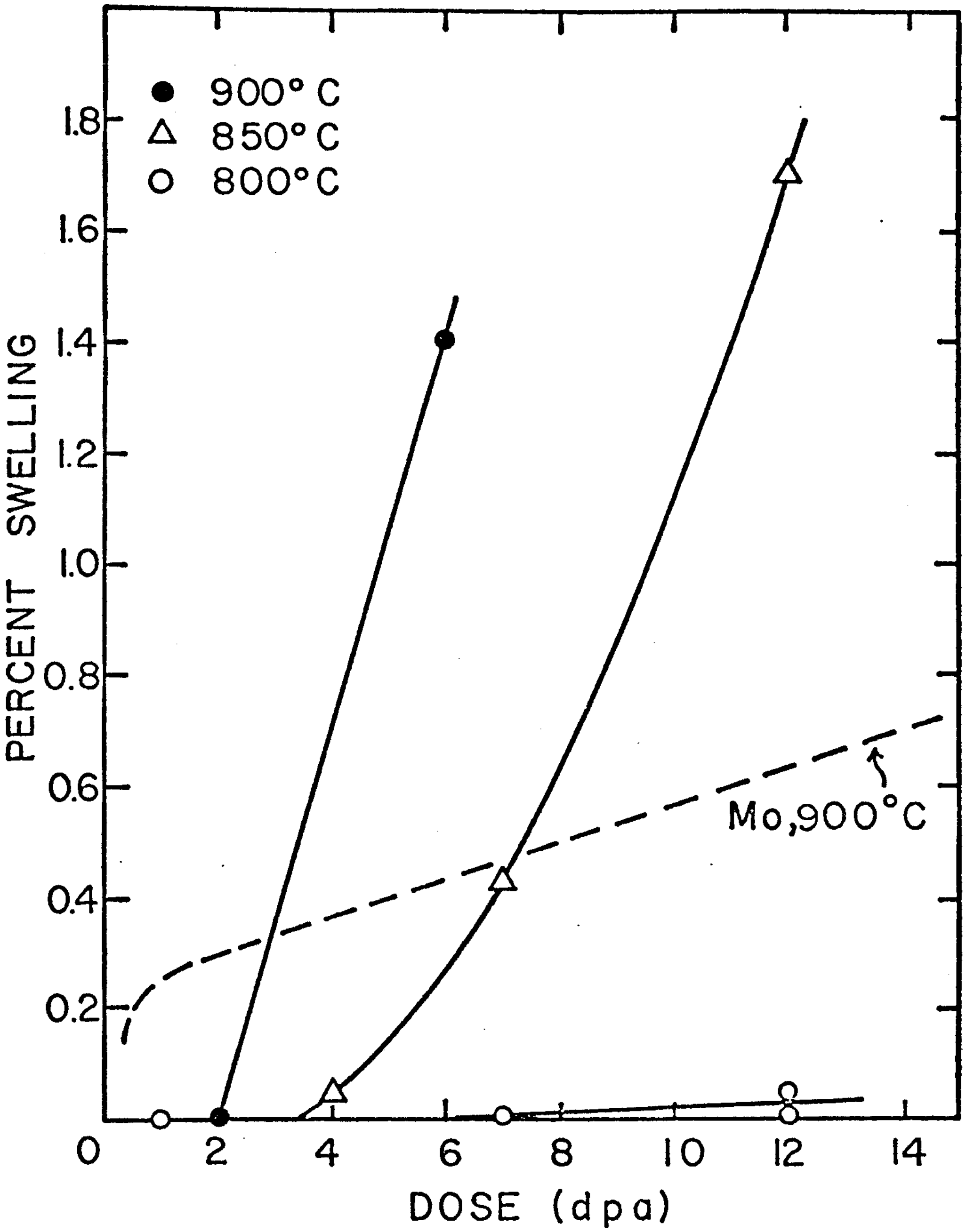

Figure V-21. Irradiation swelling of the Mo-7.5at.%Zr matrix at 800°C, 850°C and 900°C. The swelling of pure Mo at 900°C is included for comparison (dashed line).

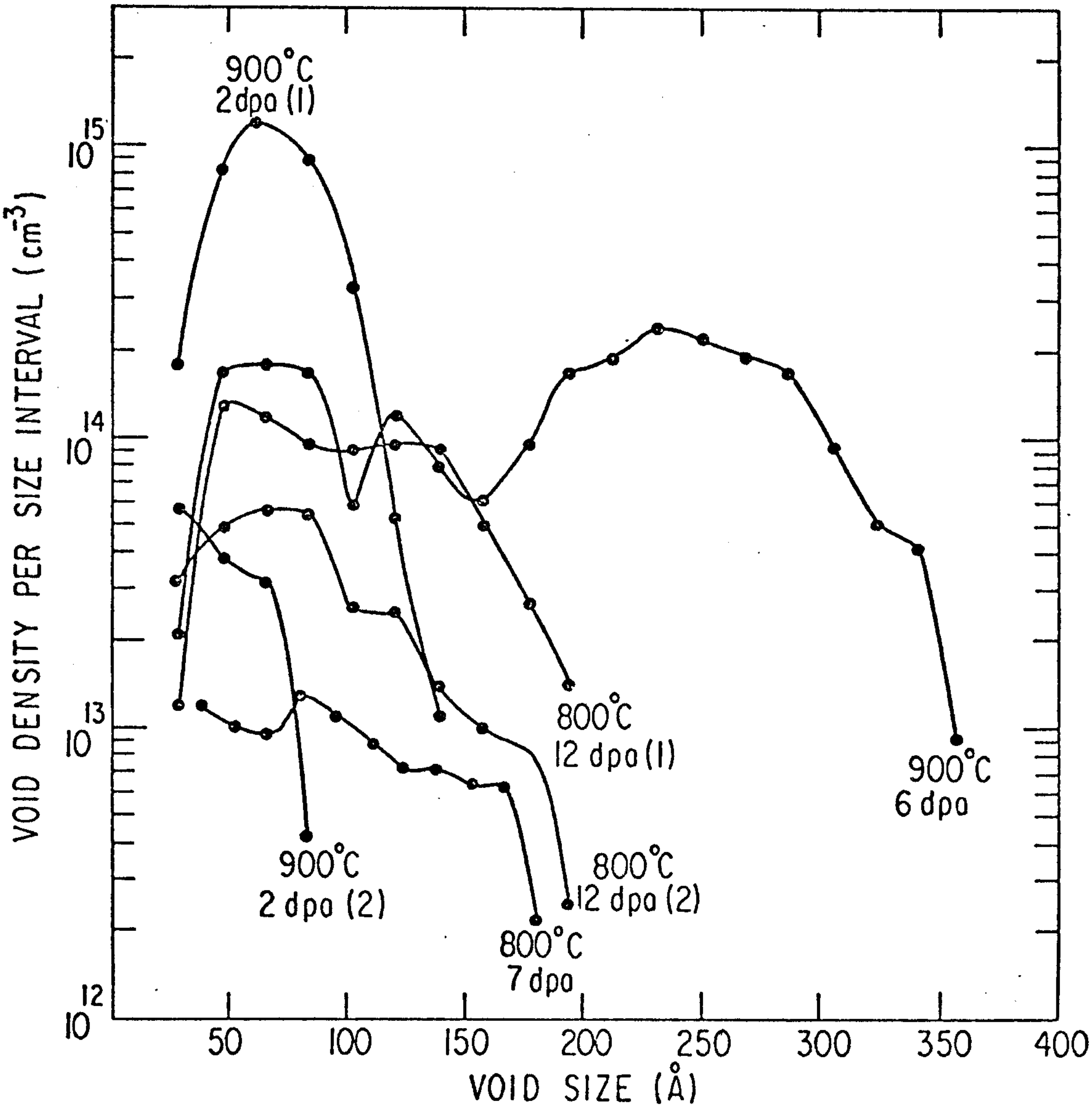

Figure V-22-a. Size distributions of voids in Mo-9.lat.%Zr irradiated with 14 MeV copper ions at 800°C and 900°C.

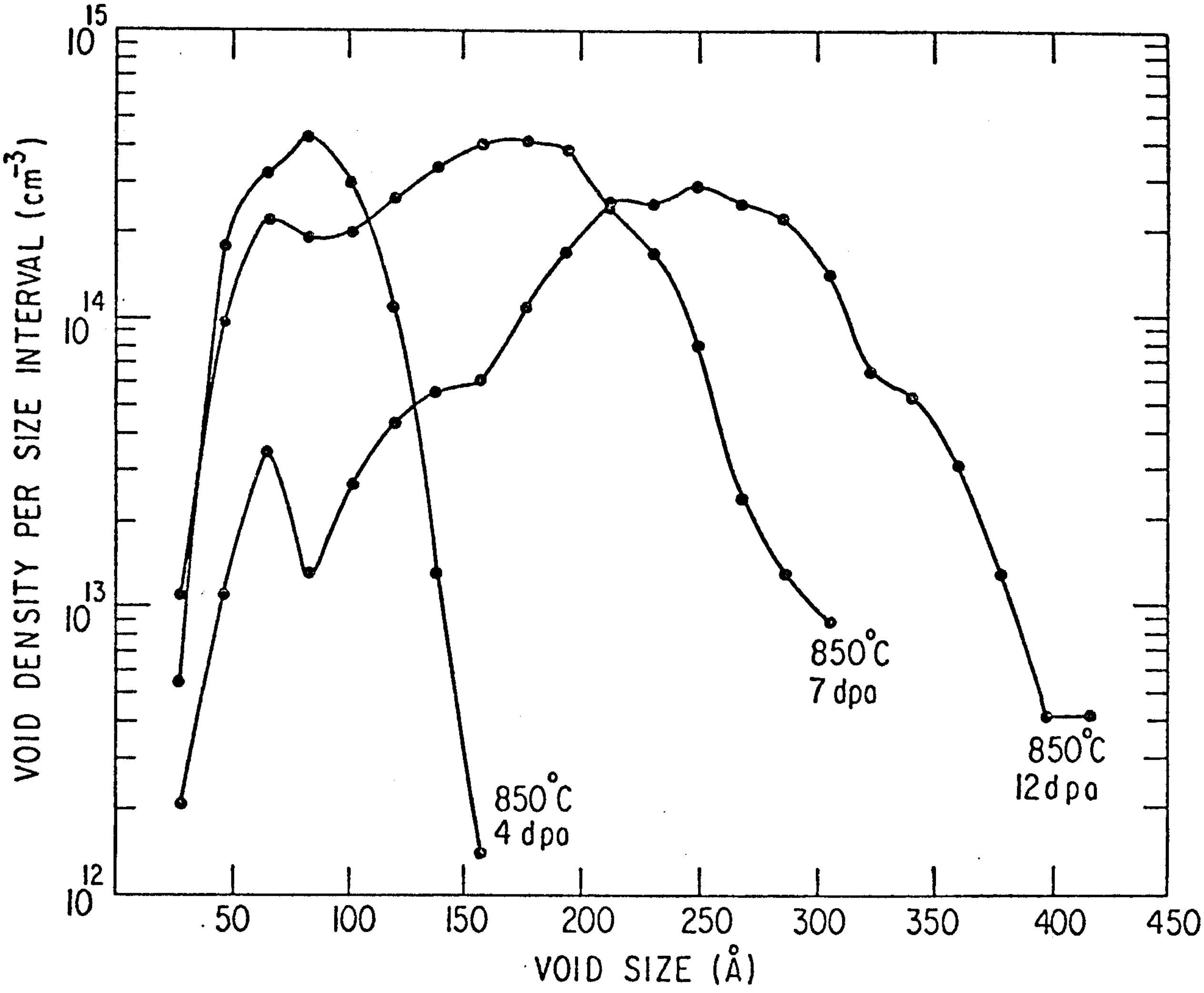

Figure V-22-b. Size distributions of voids in Mo-9.1at.%Zr irradiated with 14 MeV copper ions at 850°C.

an electron beam. Loops scarcely grew larger than $\sim$500 Å without intersecting other loops due to the high density. However, some loops (200-300 Å) which were recognizable during tilting were analyzed; they were all of the interstitial type. <110>, <112> and <002> diffraction vectors were used to determine the Burgers vectors $\pm$ b using the $\vec{g} \cdot \vec{b} = 0$ invisibility (or residual image) method. b = a/2 <110> were found for the loops analyzed. This implies that the loops were faulted. Analysis of the loop nature was carried out using the inside-outside contrast method (97). The analysis procedure is illustrated in the micrographs contained in Figure V-23 for two loops among the ten loops analyzed, all of which turned out to be interstitial type. Dislocation loops in micrographs (a) and (b) in Figure V-23 are imaged with $\vec{g} = [1\bar{1}0]$ and $[\bar{1}10]$, respectively, and positive deviation from Bragg condition ($S > 0$). The two loops indexed A and B are in inside contrast in (a) while they are in outside contrast in (b) as can be seen from the change in the loop sizes. The Burgers vectors of the two loops were determined to be $\pm$ a/2 $[\bar{1}01]$. Since $\vec{g} \cdot \vec{b}$ is positive in (b) for outside contrast, $\vec{b} = a/2\ [\bar{1}01]$ for loops A and B. (b) - (f) in Figure V are a series of micrographs taken with the same reflection $\vec{g} = [\bar{1}10]$ in a tilting sequence of the sample from near (001) to near (111). The loop habit plane is determined from the shape of the projected loop image and the sense of rotation of the major axis of the loop. The upward drawn normal to the habit planes of the two loops are then determined to be $\vec{n} \simeq [\bar{1}01]$. The product $\vec{n} \cdot \vec{b} > 0$, therefore, A and B are both interstitial loops.

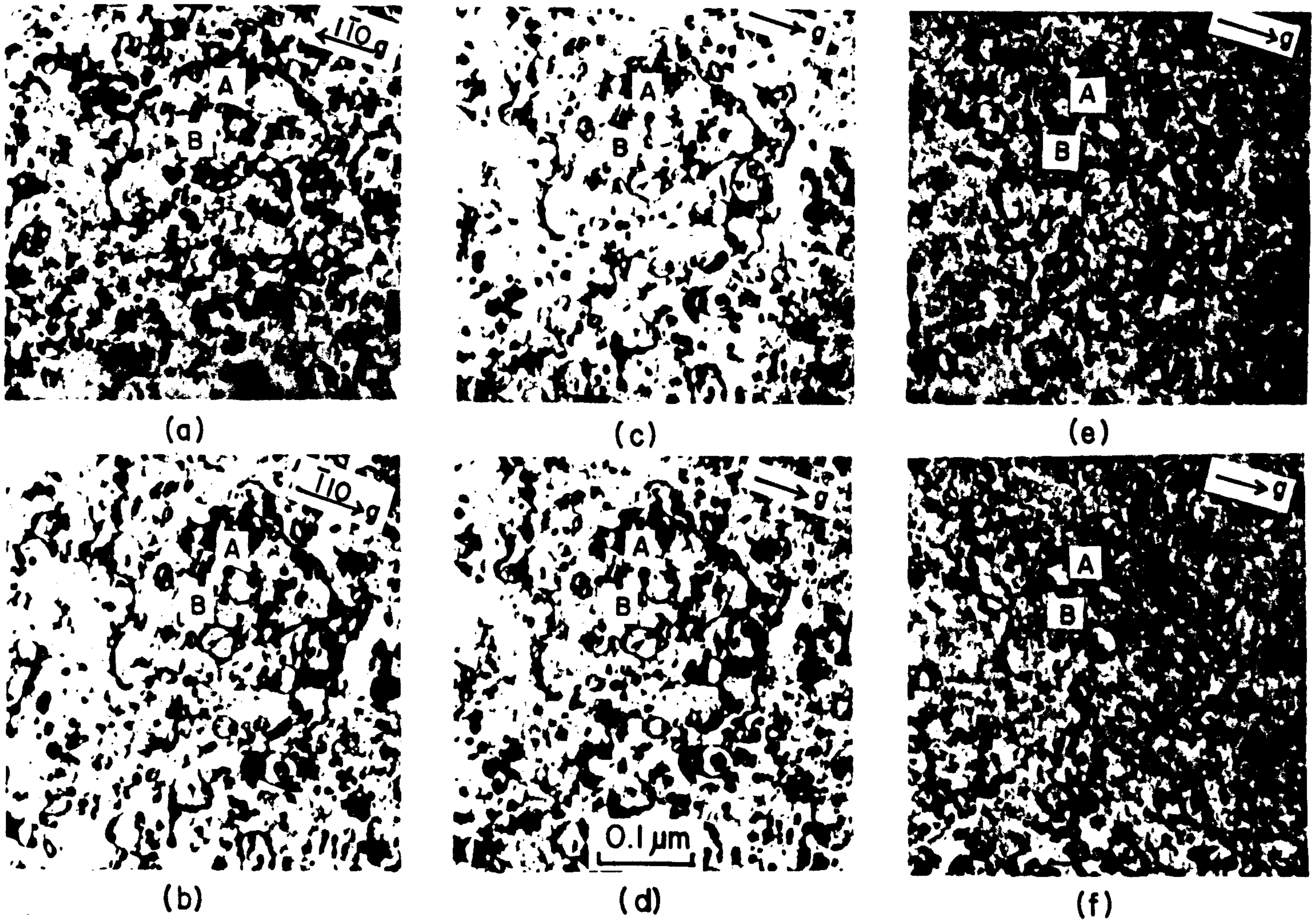

Figure V-23. Micrographs for analysis of the nature of the two large loops A and B. Loops A and B in inside contrast (a), and outside contrast (b) imaged with g = ± [1$\bar{1}$0]. (b)-(f) shows loops A and B observed during a tilting sequence from near (001) to near (111) using the same [$\bar{1}$10] reflection.

Because of the high stacking fault energy in bcc metals, interstitial loops tend to unfault to $\vec{b} = a/2\langle 111\rangle$ after nucleation with $\vec{b} = a/2\langle 110\rangle$. The observation of faulted loops in the alloy indicates that stacking fault energy is lowered by Zr solute addition. This is also evidenced by the higher density of uniformly distributed loops (as opposed to rafting) in the alloy than in pure molybdenum since a reduction in stacking fault energy promotes nucleation of interstitial loops which are sessile and unable to aggregate into rafts if they remain faulted.

2) Phase Stability

The thermal equilibrium $\gamma(Mo_2-Zr)$-precipitates produced by the pre-irradiation annealing were not transparent to the electron beam in the microscope. A stereo-pair of micrographs showed that they are spherical particles ($\sim$1μm in diameter) held by the surrounding thin foil after electropolishing. With this geometry, it was difficult to observe void or loop denuding, if it was present, near the incoherent precipitate-matrix interface. Figure V-24 shows the γ-particles after irradiation; one in the grain interior (a) and one at the grain boundary (b). In addition, shown in Figure V-24b is a void denuded zone at the grain boundary but no loop denuded zone; this is general at all other grain boundaries observed. No variation in the loop structure was observed from the grain boundary to the grain interior. It should be pointed out that the two grains in Figure V-24b were imaged under different contrast conditions to show voids in one grain and the dislocation structure in the other.

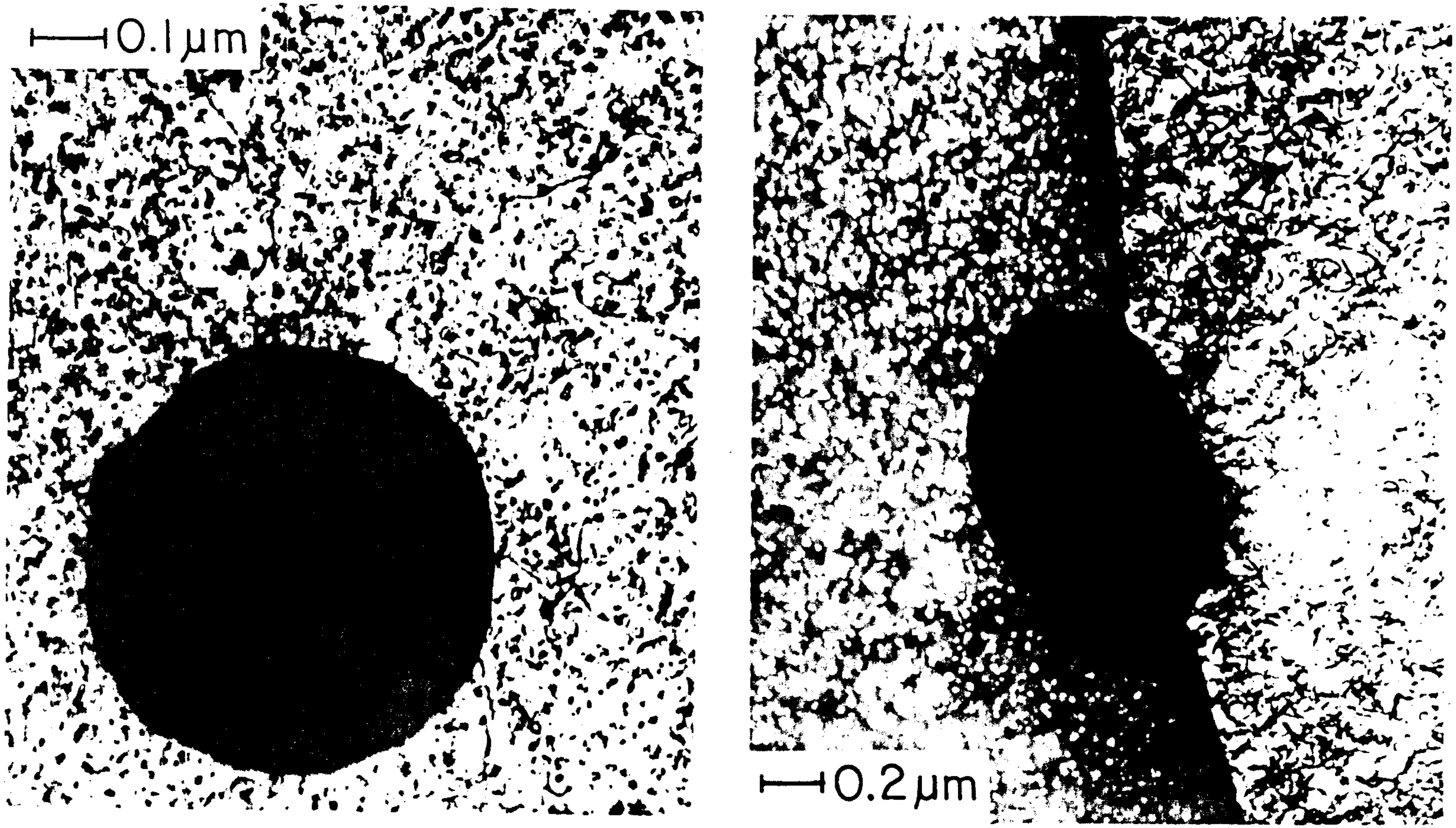

(a) 800°C, 12 dpa (b) 900°C, 6 dpa

Figure V-24. Equilibrium γ-phase (Mo_2Zr) particles in Mo-9.1 at.%Zr after irradiation with 14 MeV copper ions.

No preferential formation of γ-particles at the grain boundary was observed in the alloy before irradiation. Except for some large γ-particles (∼1μm in diameter) occasionally found at grain boundaries, the boundaries were clean in the annealed samples. After irradiation, however, small new precipitate particles were observed at grain boundaries. Figure V-25 shows a grain boundary with a void denuded zone in the sample irradiated at 900°C to 6 dpa. The black particles uniformly distributed on the grain boundary were identified from the extra electron diffraction spots to be γ-phase (Mo_2Zr). The bright field and dark field micrographs in Figure V-26 shows a shifted void denuded zone at a grain boundary in the 900°C, 6 dpa sample due to the migration of the grain boundary during irradiation. The formation of γ-particles during irradiation can be seen, especially in the dark field micrograph imaged using a precipitate reflection. Because of the large grain size (∼200 μm) in the alloy samples, not many grain boundaries were present in the thin areas of the samples. Radiation induced grain boundary precipitation was also observed in samples irradiated to 1 dpa at 850°C, 2 dpa at 800°C, 2 and 7 dpa at 700°C. The number densities of γ-particles at grain boundaries in the lower temperature samples were smaller than that in the 900°C, 6 dpa sample by a factor of 10∼50.

The radiation induced γ-precipitation at the grain boundaries could be caused by the enrichment of the over-sized Zr atoms due to the coupling between the point defect fluxes and the solute flux to the grain boundaries which are sinks for point defects. A further

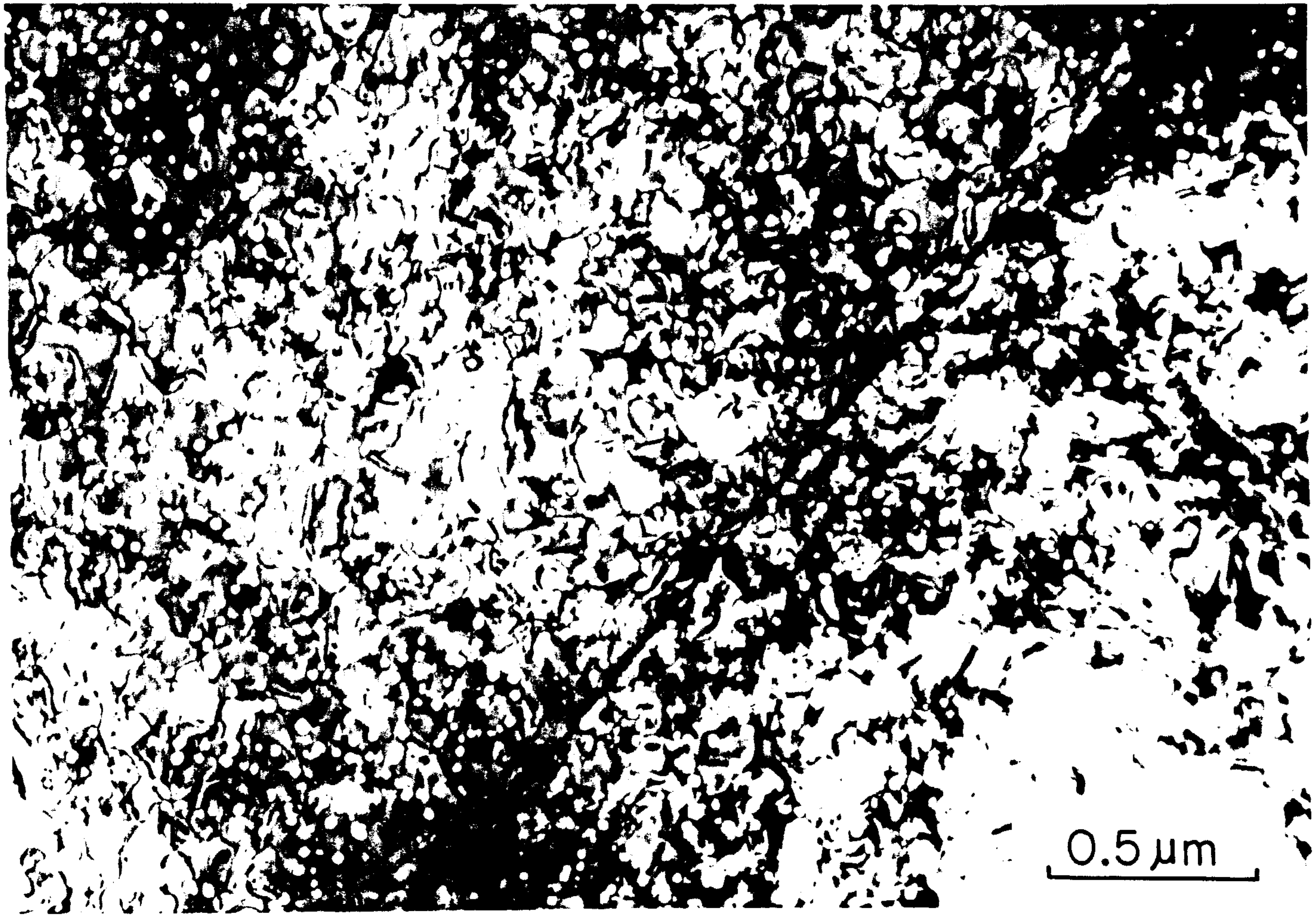

Figure V-25. Irradiation induced $\gamma(Mo_2Zr)$-precipitates at the grain boundary in Mo-9.1 at.%Zr alloy irradiated at 900°C to 6 dpa.

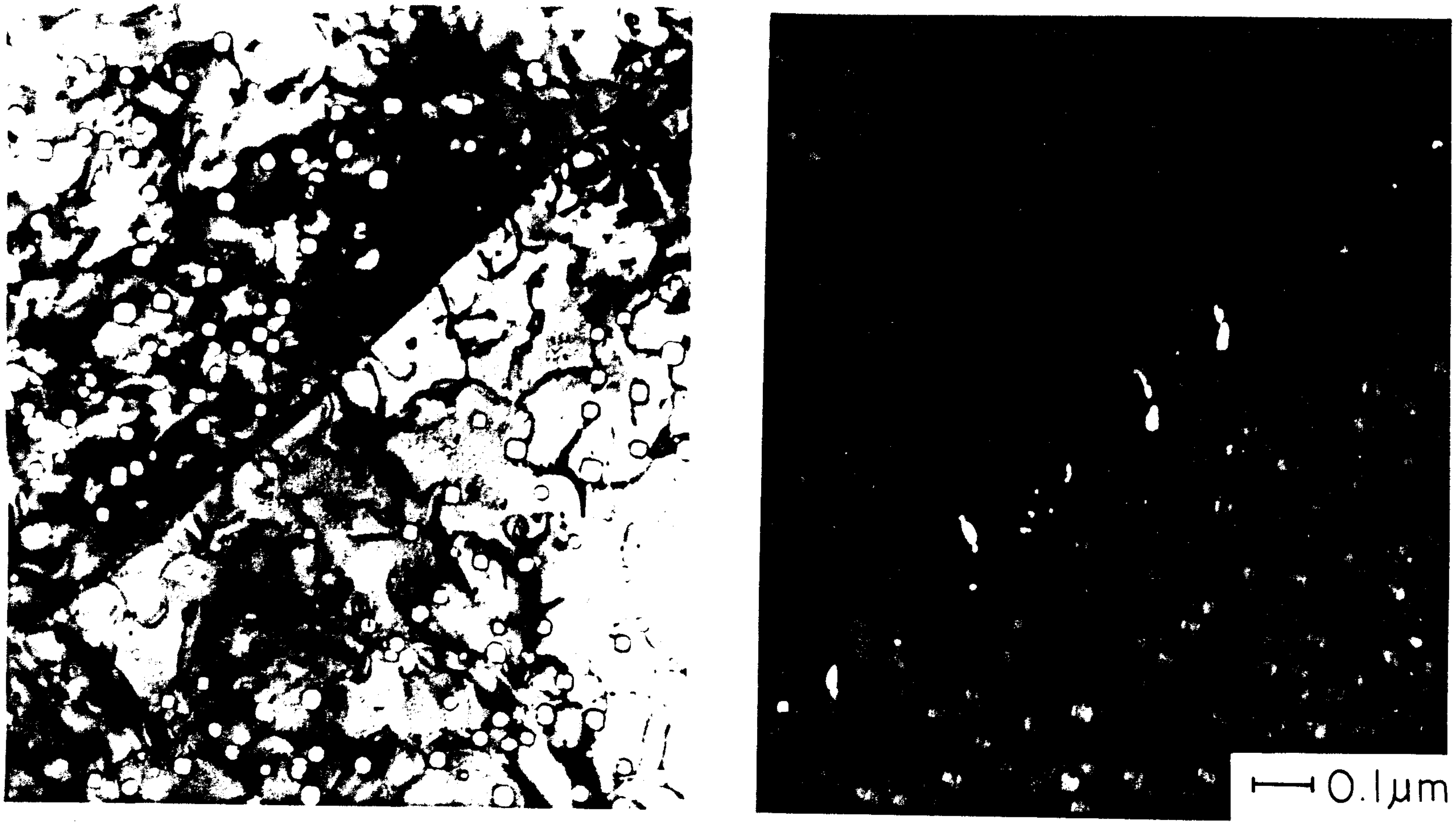

(a) **Bright Field** (b) **Dark Field**

Figure V-26. Grain boundary precipitation of $\gamma(Mo_2Zr)$, (a) bright field and (b) dark field, using a precipitate reflection. Note that the boundary has moved during irradiation at 900°C to 6 dpa, causing elongation of the precipitates.

discussion will be given in Chapter VI. In the samples irradiated to 2 and 7 dpa at 700°C, small γ-particles with low densities were observed only at some of the grain boundaries present. This could be due to the different effectiveness of grain boundaries as sinks for the point defects. Radiation induced γ-precipitation was not observed at low angle boundaries which were not efficient sinks for the point defects.

The grain interior was searched for electron reflection spots from small γ-particles induced by irradiation and dark field images using reflection from grain boundary precipitates were searched for similar precipitate particles in the grain interior. No evidence of radiation induced γ-precipitation in the grain interior, at void surfaces or at dislocations was found. A detailed discussion of the observation of γ-precipitation at grain boundaries during irradiation will be given in Chapter VI.

VI. DISCUSSION

A. Pure Molybdenum

1) BCC Ion Correlation Experiment

In this interlaboratory comparative experiment, a reference specimen of molybdenum was irradiated with different ions at different energies using the irradiation facilities at four participating laboratories listed in Table VI-1. The results were compiled by Brimhall in reference (73). In addition to the variation in the ion species, energies, and dose rates used, the vacuum during irradiation varied from 2 x 10^{-6} to 4 x 10^{-9} torr.

Figure VI-1 shows the temperature dependence of void swelling reported by participating sites. Straight lines are connected between points because there are only limited data. Error bars are shown for the results of the University of Wisconsin. The data in general agrees when experimental errors are considered. However, some scattering due to different ion species and dose rates can still be seen. The void nucleation rate increases with dose rate according to the nucleation model (102). This qualitatively agrees with the higher void densities but smaller void sizes found at PNL and NRL than at AI and UW where the dose rates used were lower.

The swelling vs dose at 900°C is plotted in Figure VI-2. Irradiations were carried out only to 2 dpa and ∿20 dpa. The irradiation with protons gave a larger swelling and a significantly higher swelling rate than with the heavy ions. This could be due to the different PKA spectra produced by proton compared to heavy ion

Table VI-1
Comparison of ion beams used at the participating sites in the BCC ion correlation experiment.

Sites	Ions	Energy (MeV)	Dose Rate (dpa/sec)
Atomic International (AI)	H^+	0.5	2×10^{-4}
Naval Research Lab. (NRL)	Mo^+	2.7	2.5×10^{-3}
Pacific Northwest Lab. (PNL)	Ni^{2+}	5	3×10^{-3}, 1×10^{-2}
Univ. of Wisconsin (UW)	Cu^{4+}	17, 19	4×10^{-4}

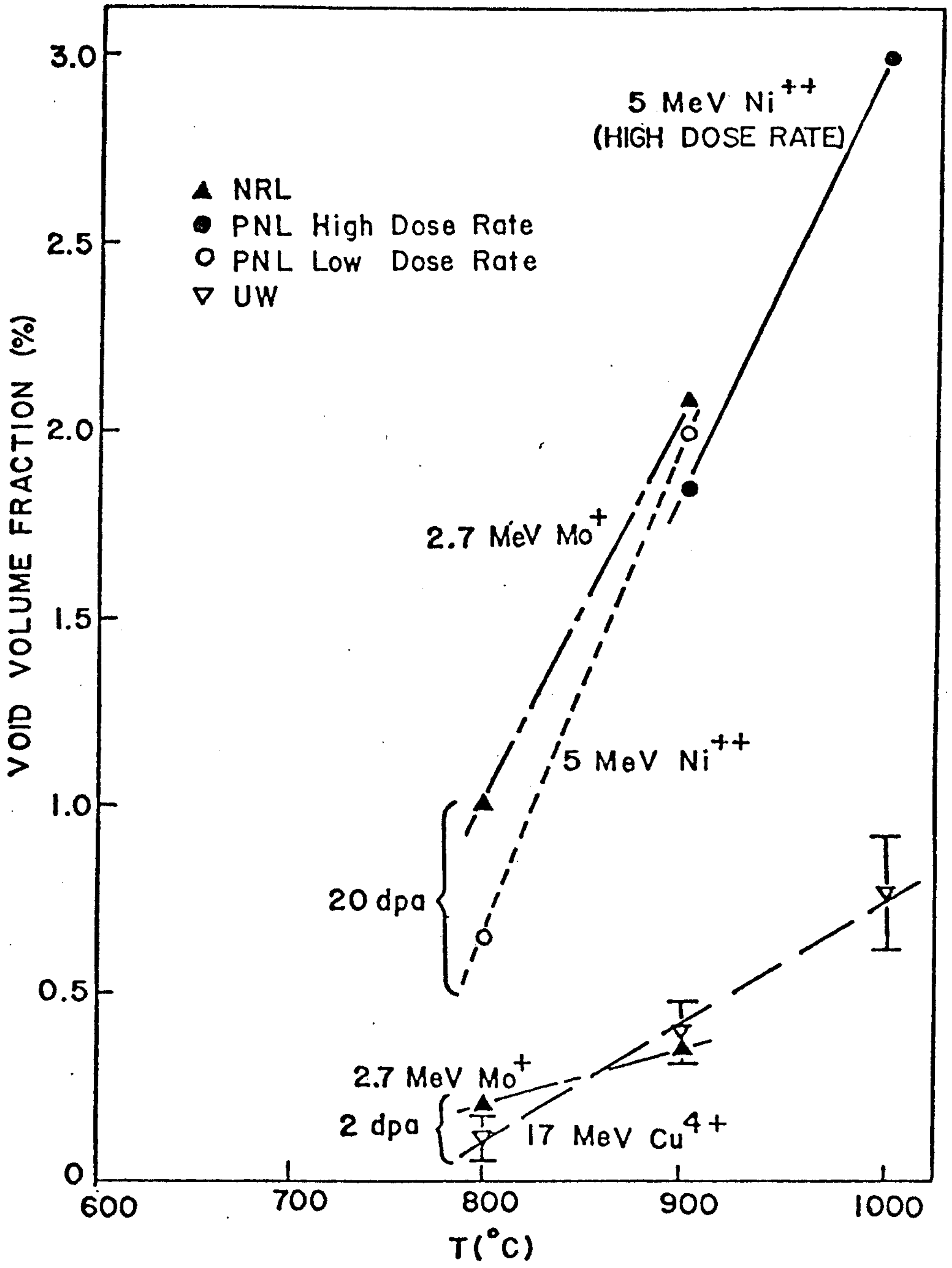

Figure VI-1. Temperature dependence of swelling in Mo bombarded by different ions in the BCC Ion Correlation Experiment. Error bars for the UW data are added.

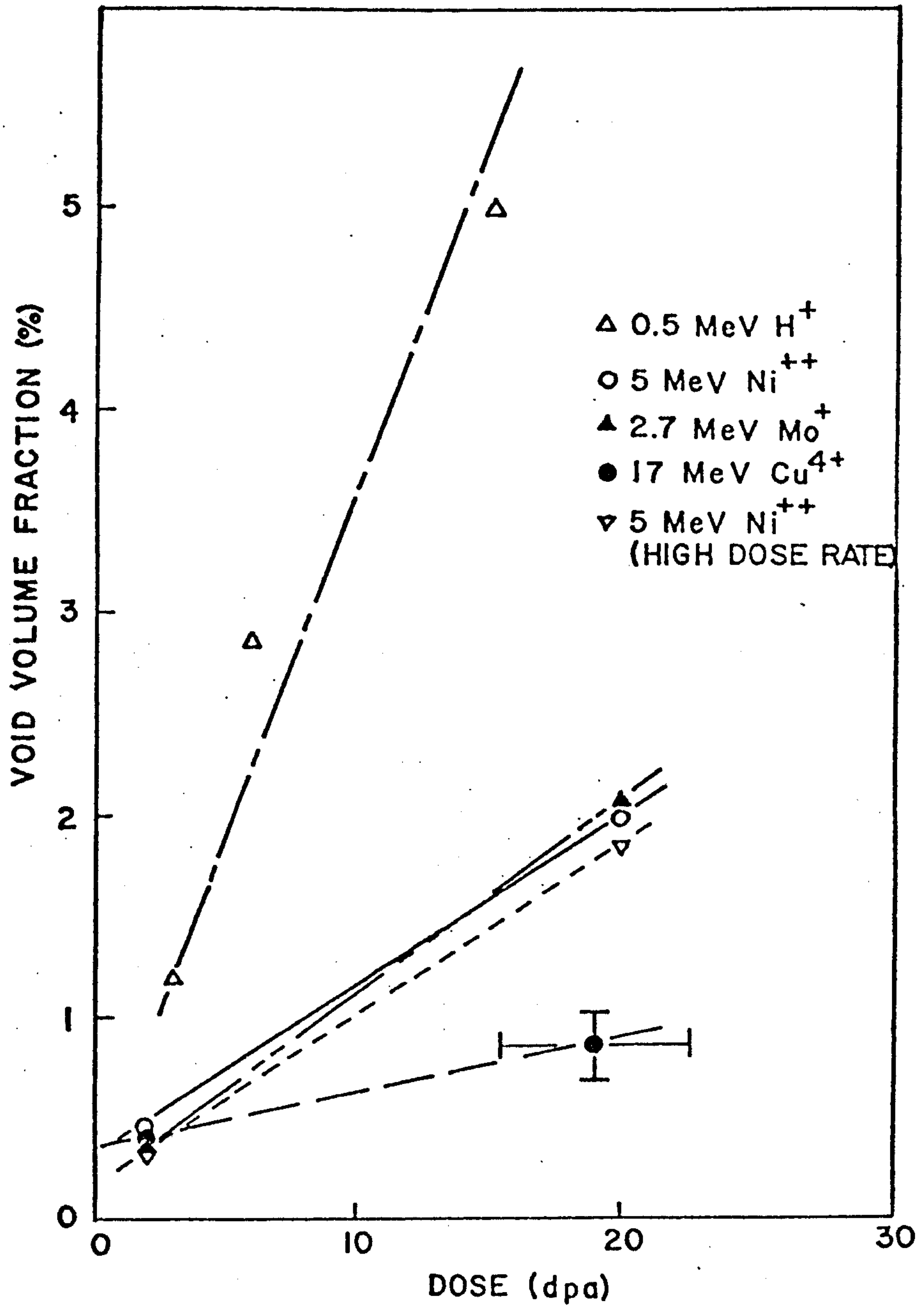

Figure VI-2. Dose dependence of swelling in Mo bombarded by different ions at 900°C. Error bar for the UW 2 dpa result is approximately the size of the data point.

irradiation or to gas effects. There is reasonable agreement between data obtained by irradiations with Ni, Cu or Mo ions except for the 19 dpa, 900°C point of UW. If the smaller swelling rate at 900°C observed at UW is not due to the lower dose rate than at PNL and NRL, another possible factor could be the difference in the amount of contamination of the samples in different vacuum or concentrations of the implanted foreign ions back diffusing to the sample analysis zone when the irradiations were carried out to high doses.

The scattering in ion irradiation data due to different transmission electron microscopy (TEM) procedure and data handling procedure was also investigated in the BCC Ion Correlation Experiment. Measurements on duplicate copies of a common micrograph supplied by NRL were made at all participating sites. The standard deviation in the average void size was 2.7% about the average value. Even though the foil thickness and the magnification of the micrograph were given, a 5.2% spread in the void number densities were found resulting in a 10.6% standard deviation in the void swelling value. This deviation could be reduced if the interpretation of void images is agreed between different laboratories. When comparison of void microstructure data of a transmission electron microscope specimen pass from site to site was made, a much larger scattering was found, as would be expected. The standard deviations were 9.6% in the average void size and 36% in void number density. The uncertainty in the foil thickness measured contributes to the large scatter in the number densities. Together with other differences in microscopy conditions, a standard deviation in the void swelling of 18% was found. Since the spread between the maximum and minimum swelling value measured on the same TEM sample was approximately 70%, it was concluded by Brimhall (73) that differences in the void volume fraction of less than 35% between two ion simulation experiments are probably not meaningful.

2) Formation of Ordered Void Lattices in Molybdenum

In the pure molybdenum samples irradiated at 900°C with 17-19 MeV copper ions in this study, random voids were observed at 1 dpa and 1.9 dpa but a void superlattice was observed in the 19 dpa sample (Table V-2). Since the void sizes in the low dose 1 dpa and 1.9 dpa samples were above the resolution limit of the transmission electron microscope, this indicates that voids are not nucleated in an ordered array, and that a dose threshold exists for voids to align into a superlattice. A partial void alignment which was the beginning of a void lattice formation was observed in the Mo sample irradiated at 800°C to 2.2 dpa. The void alignment in the later sample was not perfect and seemed to be two-dimentional. Experimental evidence therefore shows that the degree of alignment increases with increasing dose and the threshold dose is temperature dependent.

Void alignment and/or the void superlattice have been previously reported in both neutron irradiated and ion bombarded molybdenum (66-68,70-74,103-106). Much of this experimental work was recently reviewed by Brimhall (107). Because of the lack of experimental data, little success has resulted from efforts to understand the superlattice formation itself. As discussed by Stoneham in his review papers (108-109), theoretical efforts to understand the void superlattice have centered on its stability once formed. The discussion in this section will compare the results of the present experiment and those already in the leterature with the predictions of the various theoretical models and if possible eliminate those which contradict the data (94).

The data for heavy-ion bombarded molybdenum reported in the literature are summarized in Figures VI-3 and VI-4. Previous observations of no voids, random void arrays, void ordering, and void superlattices are given in plots of dose vs irradiation temperature (T_{irr}) in Fig. VI-3 and dose vs effective temperature (T_{eff}) in Fig. VI-4. The effective temperature is the irradiation temperature normalized to a dose rate of 1 x 10^{-3} dpa/sec by using

$$T_{eff}^{-1} = T_{irr}^{-1} + (k/Q_m^v) \ln (K_{irr}/10^{-3}) \qquad (6.1)$$

where k is the Boltzman constant, Q_m^v is the vacancy migration energy (=1.5 eV), and K_{irr} is the dose rate during the irradiation (7). It was well established that doses near 10 dpa are required to form the void superlattice. The present measurements, along with the previous observations, support the existence of a dose threshold near 2 dpa for the beginning of void alignment.

The approximate boundaries between the region of void superlattice formation and void ordering (solid curve) and between the random void and void ordering regions (dashed curve) are indicated in Figures VI-3 and 4. These boundaries were drawn to represent the trend of the

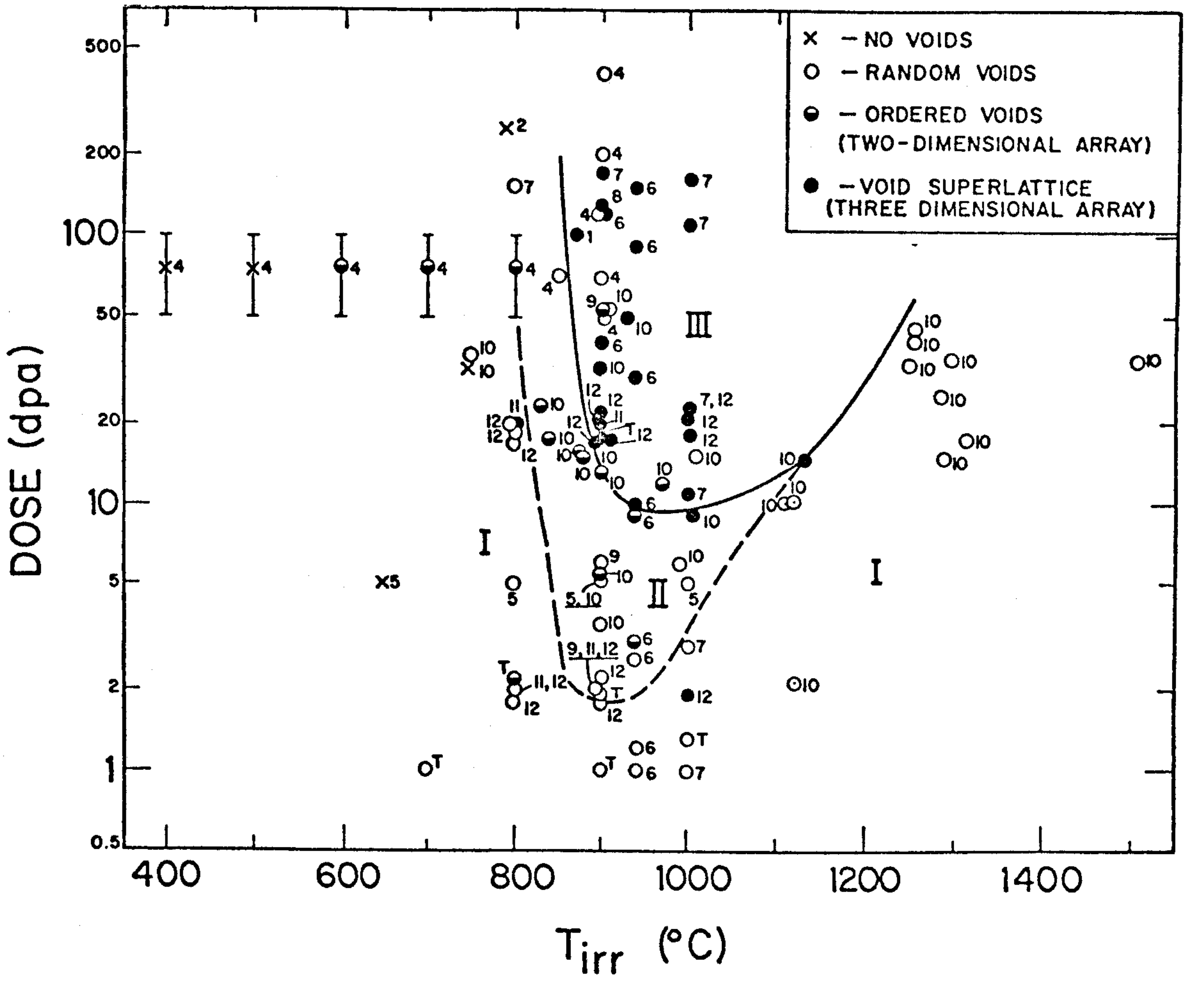

Figure VI-3. Experimental observations of the void superlattice (filled circles), void ordering (half-filled circles), random voids (open circles) and no voids (crosses) in heavy-ion irradiated molybdenum plotted in dose-irradiation temperature (T_{irr}) space. The references from which the labelled data points were taken are: 1(103), 2(104), 3(105), 4(68), 5(67), 6(70), 7(71), 8(106), 9(74), 10(72), 11(66), 12(73). The results from this study are marked with a T.

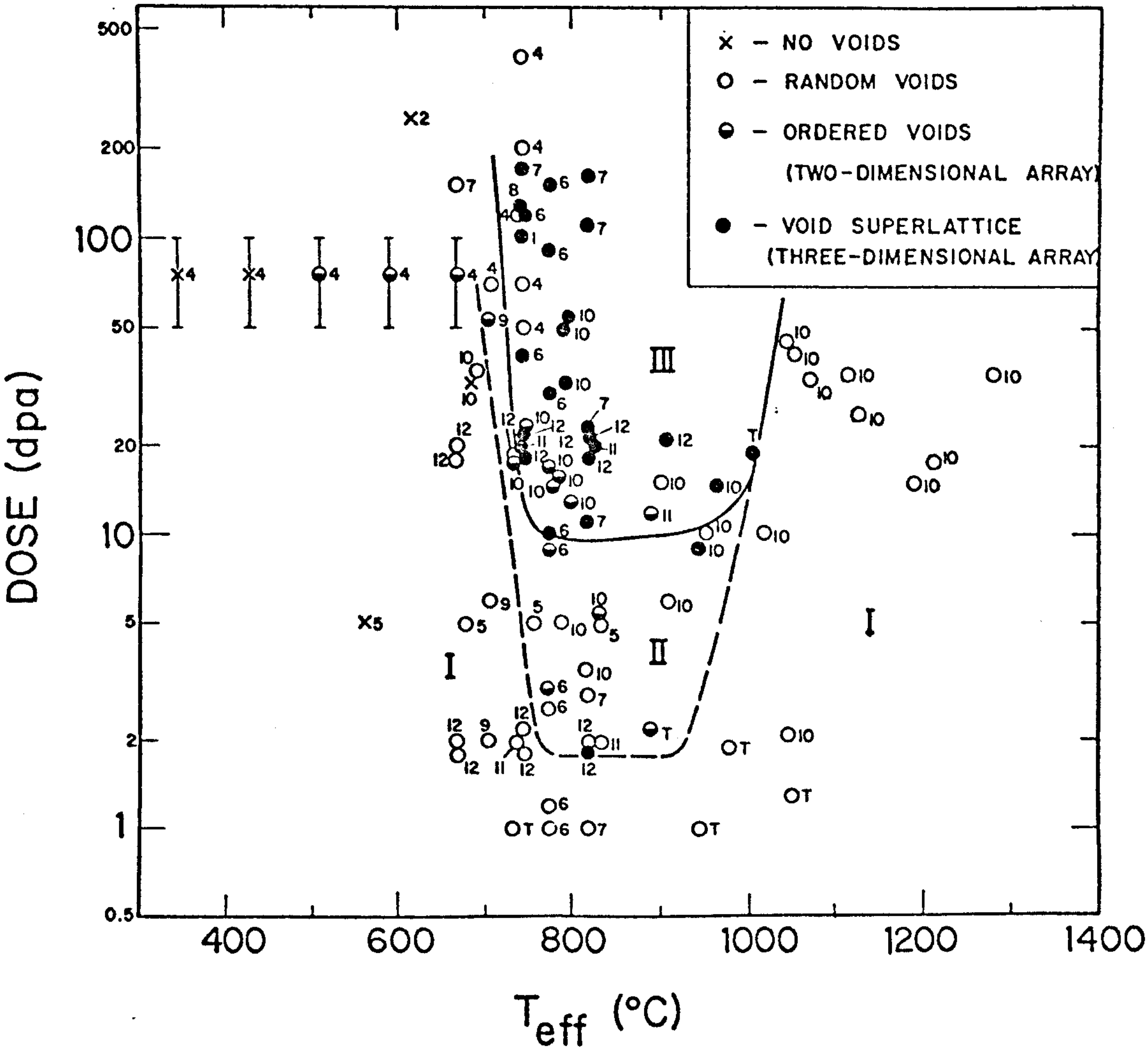

Figure VI-4. Same as Fig. VI-3 except the abscissa is T_{eff} (the irradiation temperature normalized to a dose rate of 1×10^{-3} dpa/sec using Eq. (6-1).

data. The data of Evans (68) was disregarded in drawing these boundaries since his molybdenum was preinjected with He whereas all the others included in the compilation were not. At temperatures near 0.4 T_M(900°C) where T_M is the absolute melting point, a random void array is formed as irradiation commences (Figures VI-3 and 4). As the dose level approaches 2 dpa, some void ordering occurs, primarily in one- and two-dimensional arrays (region II of Figures VI-3 and 4). As the dose is increased further, the void alignment improves until approximately 10 dpa where a three-dimensional array is formed (region III of Figs. VI-3 and 4). As the dose is increased above 10 dpa the perfection of the void superlattice increases. The experimental evidence for molybdenum shows that the initial void nuclei are formed in random array. Thus, the theories which include alignment of void nuclei as a requirement, such as spinoidal decomposition (110) or nucleation on an ordered impurity gas array (105), are not relevant for molybdenum.

Stoneham (108) suggested the following sequence for void superlattice formation: 1) initial formation of many small, randomly-distributed voids; 2) growth of voids, possibly with coarsening from the growth of large voids at the expense of small ones; 3) appearance of local ordered regions where the void distribution happens fortuitously to be favorable; followed by 4) spread of order to adjacent regions. The compilation of measurements for molybdenum given in Figs. VI-3 and 4 support Stoneham's suggestions, provided the irradiation temperature is near 0.4 T_M. A theory of void superlattice creation must also explain why random voids form easily but void alignment and/or the superlattice does not at doses above 2 dpa outside regions II and III in Figures VI-3 and 4.

Unlike niobium (111), the creation of the superlattice in molybdenum appears not to be sensitive to small amounts of interstitial impurity since the material used in this and other (66,73) studies readily forms the superlattice even though it contains $\lesssim$ 70 at.ppm of C, N, or O (Table IV-2b). Samples in this study were irradiated in pressure $\lesssim 1 \times 10^{-8}$ torr. This molybdenum is pure enough that Nolfi's solute segregation mechanism (112) is probably not applicable. Thus, the comments of Chen and Ardell (113) on the role of solute segregation in nonrandom nucleation of voids in nickel alloyed with small (∿1%) amounts of aluminum are probably not relevant. Benoist and Martin's model (114) may qualitatively explain the observed dose dependence, but Brailsford (115) has recently estimated that a dose level of ∿300 dpa for molybdenum is needed to form the void superlattice with the mechanism proposed in (114).

The formation of a void superlattice has an analogy in the alignment of precipitates during coarsening to minimize strain field interactions. (116) This involves motion of the precipitates by one side "coarsening" at the expense of the other. Given the similar interaction between voids (117,118) surface migration of atoms from higher to lower energy sides of the void would readily explain how voids move. Since this mechanism requires preexisting voids, it does not contradict the data presented in Figures VI-3 and 4.

Foreman's suggesion of a flux of interstitials along specific crystal directions can also explain the formation of the void lattice out of a random array. (119) Any such array will contain localized regions where a few voids are ordered. The interstitial flux out from this region will be peaked along the channels (close packed direction) of the ordered region according to Foreman's model. A corresponding decrease in the interstitial flux along a line of voids will also occur. Since the vacancy flux is isotropic, this could give rise to net shrinkage of neighboring voids not aligned with the void rows and growth of those which are aligned. Voids will either move in response to the anisotropic interstitial flux or nucleate and grow preferentially on lattice positions adjacent to the lattice "nucleus" causing it to grow. One drawback of this model, however, is the formation of void lattice under electron irradiation observed by Fisher and Williams (120). Interstitial flux by crowdion mechanism is unlikely to induce void alignment under electron bombardment due to the short length of the replacement sequence.

Both of the above models explain the lack of ordering at high temperatures as being due to the larger inter-void spacing implied by larger void sizes and lower nucleation rates. This would make a strain interaction, which is dependent on distance, too weak to be effective. In Foreman's model the larger distances would be beyond the range of long range interstitial motion. As has frequently been pointed out, such interstitial motion does not seem likely except at cryogenic temperatures. Nevertheless until such crowdion motion is experimentally eliminated, the model remains viable to explain the molybdenum data.

In summary, the present measurements, along with those previously published, indicate a threshold for both void ordering (∿2 dpa) and for void superlattice formation (∿10 dpa) in molybdenum. Theoretical attempts to deal with the creation of the superlattice in molybdenum are thus constrained not to use either void nucleation on a preexisting solute atom array or void nucleation in an ordered array. Instead, the voids must first form in random arrays from which void ordering and finally the void superlattice evolve. Presently this sequence can be described to be either selective growth and void motion in response to a void-void interaction (118) or to Foreman's crowdion mechanism (119) but these theories must be formulated on a more quantitative basis before detailed comparison with experiment can be accomplished.

B. Mo-9.1At.%Zr Alloy

Zr behaves as an over-sized solute in the Mo-rich solute solution. This is shown in the lattice parameter versus Zr concentration plot in Fig. VI-5 measured by Rudy (95). The effective atomic radius of Zr, R^*_{Zr} and the effective atomic volume, Ω^*_{Zr}, when Zr is added to Mo can be evaluated using the following equations from Ref. (121)

$$(R^*_{Zr} - R_{Mo}) / R_{M_o} = (1/R_{Mo}) (\partial R/\partial C_{Zr}) \qquad (6.2)$$

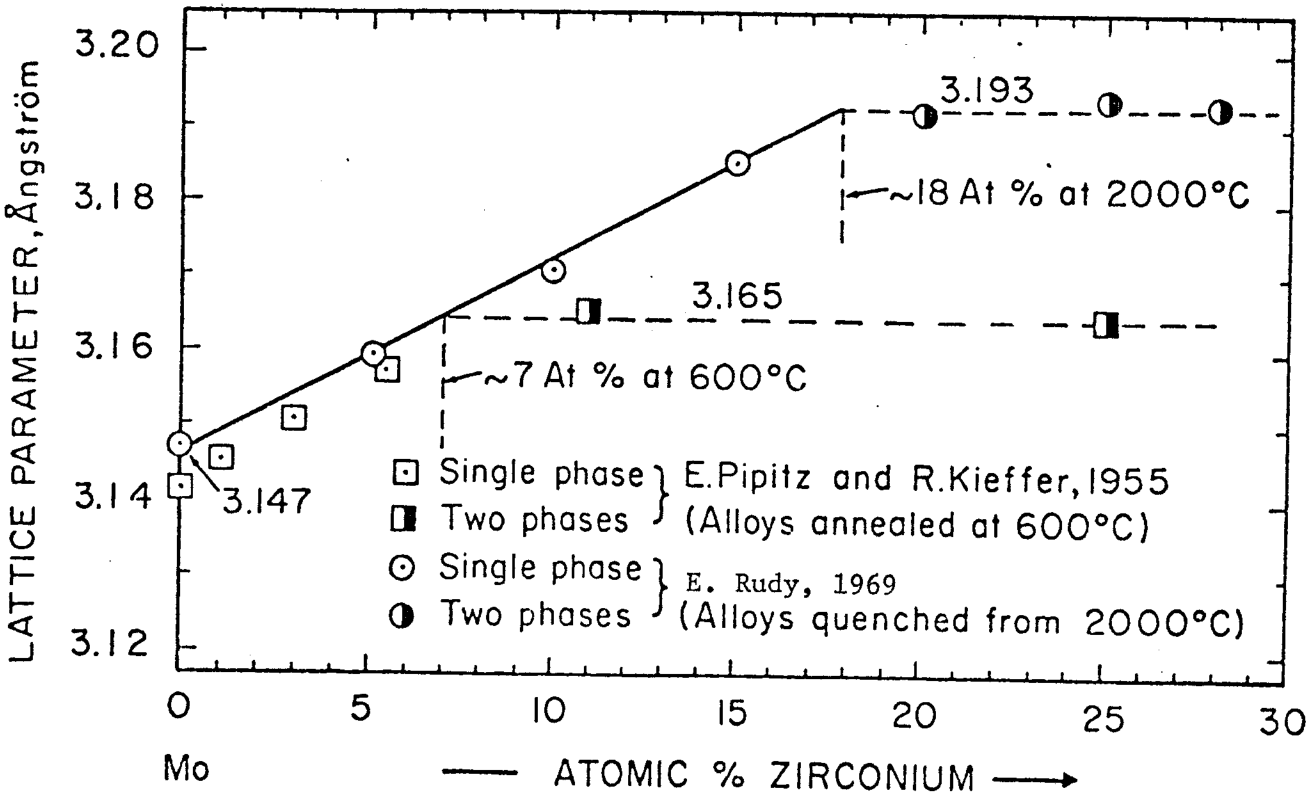

Figure VI-5. Lattice parameters of the bcc Mo-rich solid solution in the Mo-Zr system. (From Ref. 95).

$$\Omega^*_{Zr} = (R^*_{Zr} / R_{Mo})^3 \, \Omega_{Mo} \quad , \tag{6.3}$$

where R is the atomic volume of the alloy. $(\partial R/\partial C_{Zr})$ is given by the slope in Fig. VI-5.

The effective atomic volume of Zr is 26% larger than the Mo atom. This large volumetric misfit results in the formation of a Laves phase, $\gamma(Mo_2Zr)$, beyond the solute solubility limit.

In addition, Zr is an active getter which could reduce the effective concentration of interstitial impurities in the alloy. Damage microstructures that are sensitive to impurity level may therefore be affected by the presence of the ∿7.5at.%Zr in the saturated Mo-rich matrix of the two-phase alloy.

The effect of Zr solute on the damage microstructure and the phase stability of the alloy will now be discussed in terms of the above physical and chemical properties of Zr.

1) Effect of Zr Addition on Damage Microstructure

Comparing the results of the alloy to pure Mo shows that Zr:

a) Causes faulting of dislocation loops

b) Promotes dislocation loop formation

c) Introduces incubation period for void nucleation, and

d) Increases void growth rate.

The dislocation loops analyzed were all of the interstitial type, which form by nucleation from the supersaturated interstitials. Interstitial loops in pure Mo have been observed to unfault from a faulted configuration at an early stage after nucleation (44) due to the high stacking fault energy of loops in bcc Mo. The observation of faulted interstitial loops in the alloy indicates that the stacking fault energy is reduced by Zr addition. The nucleation of loops is therefore promoted, resulting in the high loop densities observed in the alloy. Loops are sessile when they remain faulted. "Rafting" of small loops is therefore prohibited in contrast to pure Mo. This can be seen in the stable loop structure from the nucleation stage until coarsened into a uniformly distributed dislocation network observed in the alloy.

Growth of interstitial loops is controlled by the dislocation bias and vacancy emission [Eq. (2.39)]. The former depends on the diffusion of vacancies and interstitials and their concentrations which depend on the instantaneous defect sink density and the displacement rate. Emission of the vacancies from interstitial loops is a thermodynamic process which depends exponentially on the negative sum of the elastic energy and the stacking fault energy of the loop devided by the temperature. Increasing stacking fault energy decreases the loop growth rate especially at high temperatures where loop growth is emission controlled. The reduced stacking fault energy of the loops in the alloy could actually decrease the loop growth rate because the loops are allowed to remain faulted. This agrees with the experimental observation that a higher temperature is necessary for a significant loop growth rate in the alloy.

The reason for the reduction in the stacking fault energy is not understood at this time. In general, undersized impurity atoms are attracted to interstitial loops and the stacking fault energy is reduced when the under-sized substitutional impurity segregates to the loops. This is not the case for the over-sized Zr. The decrease in the stacking fault energy may be due to an intrinsic effect in the solid solution affecting the interatomic potential.

When Zr is added to Mo($\sim$7.5at.%Zr in the saturated solution), the void volume swelling is supressed or reduced at lower temperatures or lower doses. At higher temperatures ($\geq$ 850°C) and doses ($\geq$ 4dpa), however, a significantly higher swelling rate resulted in a larger void swelling of the alloy than pure Mo. The reduced swelling at low doses is due to the difficulty of void nucleation in the alloy while the larger swelling at higher doses is caused by the large void growth rate.

The incubation dose for void nucleation in pure Mo, if it exists, is very small. However, an incubation period is required for the formation of observable voids. Binding between the vacancies and the over-sized Zr atoms could reduce the mobility of the vacancies and therefore enhance the defect recombination rate, resulting in lower concentrations of free point defects. Defocusing of focussed replacement sequences due to the lattice distortion at the positions of the over-sized solute atoms has also been proposed to decrease the spatial separation between the vacancies and the interstitials in the displacement cascade. This correspondingly decreases the concentrations of point defects escaping the cascade (43). The void nucleation rate would then be reduced by the effect of the over-sized Zr. An enhanced defect recombination rate, however, also decreases the void swelling. Since the total void swelling was observed to increase significantly compared to pure Mo at higher doses at 850°C and 900°C, this can not be the case. A lower loop nucleation rate caused by the same defect recombination is also in contradiction with the experimental observation.

It is more likely that the Zr is gettering a necessary impurity for easy void formation (probably oxygen), so delaying void nucleation. The larger void growth rate compared to pure Mo is probably due to the higher dislocation density, which provides a larger biased sink strength for the point defects.

Formation of a void lattice was not observed in any of the irradiated Mo-9.1at.%Zr samples. Interstitial impurities have been found to be necessary for void superlattice formation in niobium (111). Though void alignment in molybdenum seems to be not sensitive to impurities as discussed in Section VI-A2, the Zr could be gettering small amounts of interstitial impurities which help void alignment. If this is not the case, defocusing of focussed replacement sequences by the over-sized Zr atoms could render void alignment by Foreman's crowdian mechanism (119) ineffective. Also, the elastic constants may change due to the addition of the over-sized Zr atoms and therefore void alignment by the mechanism of selective growth and void motion due to void-void elastic interaction (118) is affected.

2) Radiation Induced Solute Segregation and Precipitation on Grain Boundaries

Experimental evidence presented in Section V-B2 shows that γ-phase (Mo_2Zr) particles formed on the grain boundaries during irradiation with 14 MeV copper ions. The precipitation is unlikely to be related to the implanted copper ions because it was observed in low dose samples in which the irradiation times were not long enough for the implanted copper ions to diffuse back to the TEM analysis zone even under irradiation-enhanced grain boundary diffusion conditions.

The new precipitate particles on the grain boundary were identified to be γ-phase (Mo_2Zr). Since the alloy was previously equilibrated in the two-phase region, the precipitation of γ-particles implies Zr enrichment of the grain boundary during irradiation. This may be explained by radiation-induced solute segregation if a large binding energy between the vacancy and the over-sized Zr atom is assumed (18).

The kinetic models of solute segregation under irradiation have been reviewed in Section II-E2. A binding energy between the vacancy and the solute atom of 0.1 eV was estimated to be necessary for solute enrichment at defect sinks using the model of Johnson and Lam (58) applied to dilute fcc alloys. Although the description of defect-solute interaction by a binding energy becomes less applicable as the solute concentration increases, an attractive interaction between the vacancies and the Zr atoms can still be expected due to the large 26% volumetric misfit.

A more general approach for concentrated alloys is to describe solute segregation at grain boundaries as being due to a coupling between the flux of Zr atoms and the vacancy flux to grain boundaries which are sinks for the point defects. The enrichment of solute atoms at a defect sink builds up a solute concentration gradient, resulting in a back diffusion of solute away from the sink. A steady state is attained when the solute back diffusion is balanced by the solute flux to the sink. The formation of the second phase γ-particles when the grain boundary is supersaturated with Zr reduces the solute concentration; therefore, a net solute flux to the grain boundary continues. The grain boundary is generally a large collecting plane for solute atoms and a fast diffusion path which eases the nucleation and growth of new γ-particles.

Void surfaces and dislocations are also sinks for the point defects but no irradiation-induced γ-phase precipitation was detected there. Nucleation of induced γ-phase could be more difficult at void surfaces or dislocations. If both the void surface and the incoherent grain boundary are considered as infinite natural sinks for the point defects, the grain boundary will be getting more solute atoms per unit area than the void surface because the former is subjected to solute fluxes from both sides while the latter has solute flux only from one side of the surface. The void surfaces might not be getting sufficient solute supersaturation at the irradiation rates in this study for nucleation of the γ-phase to occur.

Not all of the grain boundaries are equally effective sinks for the point defects. No γ-precipitation under irradiation was observed at low angle boundaries. After irradiation, the structure dislocations at the low angle boundaries were usually mixed with the irradiation-induced dislocations since no dislocation loop denuded zone was found at grain boundaries in the alloy.

Further studies of the kinetics of precipitation due to the segregation modification of local solute concentration is needed to understand the whole picture. This experimentally established phenomenon must be considered in other models of irradiation-induced phase instability by different mechanisms.

C. Summary

1. Voids form at the early stage of copper ion irradiation in pure Mo. Nucleation is completed at higher doses and further swelling is caused by void growth. The peak swelling temperature is higher than the temperature range investigated (700°C∿1000°C).

2. At temperatures near or just below the void formation threshold (∿700°C) in pure Mo, voids are replaced by small dislocation loops as the major damage feature showing a tendency to loop "rafting".

3. Voids are randomly nucleated in pure Mo before they align into a bcc superlattice in a temperature and dose range inside the void swelling region. The threshold dose is ∿2 dpa for void ordering and ∿10 dpa for void superlattice formation at temperatures near 0.4 Tm (Tm = absolute melting point).

4. An incubation period was required for void nucleation in Mo-7.5at.%Zr alloy (the saturated matrix of the two-phase alloy). This may be due to Zr gettering a gas impurity which stabilizes voids. Total swelling is increased at higher temperatures and doses in the alloy due to the higher dislocation loop density. The addition of 7.5-at.%Zr may have supressed the tendency of void superlattice formation.

5. The stacking fault energy of interstitial loops in the alloy is reduced; therefore dislocation loop formation was promoted. Unlike pure Mo, the loops remained faulted before intersecting each other and were not able to glide.

6. Solute-defect flux coupling effects were observed in the form of incoherent precipitation of $\gamma(Mo_2Zr)$ at the grain boundaries during irradiation.

VII. THEORY OF RADIATION INDUCED DISORDER AND PHASE INSTABILITY

A. Introduction

Experiments have shown that under irradiation precipitates may either grow or shrink, that equilibrium phases may dissolve and be replaced with non-equilibrium phases and that precipitation sequences may be altered. The situation is evidentally very complex and several different mechanisms are operating to modify microstructural phase stability under irradiation.

The mechanisms that have been proposed and in some cases demonstrated, can be classified.

a) Radiation Enhanced Diffusion. The increase in point defect population caused by atomic displacements causes an increase in diffusion rates (12). This often permits sluggish phase transformations to proceed to completion under irradiation when thermal reaction had apparently ceased.

b) Radiation Induced Segregation (18). During irradiation, large numbers of point defects are generated, diffuse to sinks and annihilate. Any coupling between solute atoms and this flux of defects will induce a flux of solute towards or away from the sinks. The segregation induced by the solute flux can cause the composition of local regions to cross the phase boundary so that precipitation can occur (55). Elsewhere in the matrix a corresponding depletion of solute can cause precipitate dissolution.

c) Other Flux Coupling Phenomena. A coupling between defect fluxes and solute atoms may occur near precipitates to aid the defect annihilation. For example (64), an incoherent precipitate may annihilate vacancies at its sourface only if the resultant volume strain is relieved by transfer of solute into or out of the precipitate (depending on the relative solute - atom sizes in the matrix and precipitate). Alternatively Martin (122) has proposed that solute concentration fluctuations may attract defects and enhance recombination. The resultant depletion of defects induces a further defect flux into the region and this may drag more solute and enhance the intensity of the fluctuation to the point where precipitation can occur.

d) Cascade and Displacement Effects. The damage process may directly affect precipitates by removing solute atoms from a precipitate by energetic knock-on or by cascade dissolution at the surface of a precipitate (13,14,17).

e) Defect Concentration Effects. In contrast to the effect of defect fluxes which are involved in a), b) and c). It has been proposed (123) that the steady-state defect concentration under irradiation may itself destabilize a phase and permit an alternative phase to precipitate instead.

This Chapter represents a new approach to mechanism e). The steady-state defect concentrations under irradiation are generally too small to produce the $\sim$10-100 kj/mol in internal energy required to destabilize equilibrium phases.

However, in ordered alloys in addition to vacancy and interstitial defects caused by atom displacements, there are anti-structure atoms caused by atom replacements. Since the replacements often exceed the displacements by between one and two orders of magnitude the steady-state concentration of anti-structure atoms can be much larger than for other defects. If the ordered phase has a high ordering energy and a slow reordering rate, the energy involved in radiation-induced disordering can easily reach the levels required to modify phase stability.

A detailed model (45) for the disordering of phases by irradiation and the calculation of radiation modified phase diagrams will be presented here.

B. Radiation Induced Disorder

There is abundant evidence that radiation induces disorder (124-127). An irradiation process which creates atomic displacements will also create replacements. In an ordered alloy both events produce point defects; displacements producing frenkel pairs and replacements producing anti-structure atoms. Since these events are caused by the incident particles with energies much greater than the thermal energy per atom, the defect production itself is independent of temperature (except for any temperature induced defocussing of collision sequences).

Any disordered alloy will return to its equilibrium degree of order provided the appropriate diffusion process can operate. The radiation-produced vacancies and interstitials enhance diffusion (provided that they are mobile) so that radiation can also enhance the reversion to the equilibrium degree of order.

In an ordered alloy under irradiation we therefore have two opposing processes continuing, a disordering and a reordering, with some steady-state degree of order being established when the two rates balance. The purpose of this section is to describe a simple model for calculating this steady-state order. Only long range order of stoichiometric ordered phases is considered here.

The Bragg-Williams definition of the long range order parameter for a binary alloy with atoms arranged on two sublattices α and β is

$$S = \frac{f_{A\alpha} - X_A}{1 - X_A} \tag{7.1}$$

where $f_{A\alpha}$ is the probability of an A atom being at an α lattice site, and X_A is the atomic fraction of A atoms. $S = 1$ when the alloy is completely ordered and $S = 0$ when it is completely random. When the ordered alloy is irradiated, a rate equation can be written for the balance between the disordering and reordering rates

$$\frac{dS}{dt} = \left(\frac{dS}{dt}\right)_{Irr} + \left(\frac{dS}{dt}\right)_{Th'} \quad . \tag{7.2}$$

The second term on the right-hand side is the irradiation enhanced thermal reordering rate.

The solution of this steady-state equation gives the steady-state degree of order under irradiation. In order to find this we must first express the ordering and disordering rates in terms of the irradiation and material parameters and to this we now turn.

1) Irradiation Disordering

The unit of radiation damage, displacement per atom (dpa), which has been commonly used for void swelling studies, is not appropriate for radiation induced disorder. We need instead the total number of atoms replaced by other atoms during irradiation. A replacement event can be either a direct replacement or the production of an interstitial which recombines with a vacancy or migrates to a defect sink. If we assume that atoms are randomly replaced by other atoms, it can be easily shown by probability considerations that

$$\left(\frac{dS}{dt}\right)_{Irr} = -\left(\frac{\nu_r}{\nu_d}\right) kS \tag{7.3}$$

where k is the dpa rate, ν_r is the number of replacements and ν_d is the number of displacements.

There are different mechanisms by which an ordered alloy can be disordered by irradiation. In the case of disordering due to focused replacement sequences (or dynamic crowdions), disordering depends on crystallographic directions and Eq. (7.3) should be multiplied by a geometric factor. Disordering can occur locally in displacement spikes by uncorrelated recombinations of frenkel pairs or by formation of defect clusters (vacancy loops formed by cascade collapse for example). The mixing of atoms in these regions is probably random and can, therefore, be approximated by Eq. (7.3). In general, we can introduce a disordering efficiency ε and write

$$\left(\frac{dS}{dt}\right)_{Irr} = - \varepsilon kS \quad . \tag{7.4}$$

The parameter ε is of the order of the ratio (ν_r/ν_d).

2) Irradiation Enhanced Thermal Reordering

Nowick and Weisberg (128) consider an order-disorder transition as a chemical reaction in which a pair of A-B atoms at the wrong lattice sites is interchanged to give an A-B pair at the right lattice sites,

$$(AB)_w \underset{K_2}{\overset{K_1}{\rightleftharpoons}} (AB)_r \quad . \tag{7.5a}$$

The rate constants for the reaction are given by

$$K_1 = \nu_1 \exp (-U/k_B T) \tag{7.5b}$$

$$K_2 = \nu_2 \exp [-(U+V)/k_B T] \tag{7.5c}$$

where U is the energy barrier for the reaction and the activation energy V is the energy reduction when a wrong A-B pair transforms into a right A-B pair. V depends on the instantaneous configuration of atoms (or the degree of order), ν_1 and ν_2 are frequency factors.

Nowick, et al. (128) show that at low temperatures where S approaches unity, the solution of the chemical rate equation reduces to

$$\frac{1-S}{1-S_e} = \coth\,(xt+y) \tag{7.6a}$$

where S_e is the equilibrium order parameter, y is a constant.

For our purpose we require the time derivative of S which is

$$\left(\frac{dS}{dt}\right)_{th} = \frac{x(1-S)^2}{(1-S_e)} - (1 - S_e)x \tag{7.6b}$$

with the rate constant x in the absence of irradiation being (128),

$$x = (\nu_r\nu_w)^{1/2}\left[\frac{X_A}{X_B}\right]^{1/2} Z_\beta \exp\,[-(U+V_o/2)/k_BT] \tag{7.7}$$

where V_o is the activation energy when S = 1. Z_β is the number of β sites which are nearest neighbors to an α site while ν_r and ν_w are the frequency factors for a right and a wrong pair, respectively. If the activation entropy is neglected, these frequencies are close to the Debye frequency. Although Eq. (7.6a) is derived for S close to one, it has been shown to fit experimental data from Cu_3Au and Ni_3Mn quite well for the whole range of order (128-132). This mass reaction model, however, does not relate the kinetics of order-disorder transition to the point defects. To modify the model for alloys under irradiation, one simply considers vacancies and interstitials as species of catalyst for the chemical reaction in Eq. (7.5a).

Consider first the vacancy mechanism, there are different paths for the order-disorder reaction of an A-B pair. Figure VII-1 shows the most probable path which consists of two successive jumps of the A and B atoms involving only one vacancy. By this reaction path, the Boltzmann factor with the energy barrier U can be written as

$$\exp\ (-U_v/k_BT) = C_v\ \exp(-2E_v^m/k_BT)\ (Z_\alpha + Z_\beta - 2) \qquad (7.8)$$

where C_v is the concentration of vacancies and E_v^m is the vacancy migration energy. Z_α is the number of the nearest neighbor α sites to a β site, and Z_β is the number of nearest neighboring β sites to an α site. Transition from a wrong A-B pair to a right A-B pair by this reaction path can begin with a vacancy either at one of the Z_α sites or at one of the Z_β sites. The total number of such reaction paths for the A-B pair considered, is therefore, $(Z_\alpha + Z_\beta - 2)$. In both CsCl and $AuCu_3$ type superlattices, $Z_\alpha + Z_\beta - 2 = 14$. The pre-exponential factor for the reaction path of non-successive jumps involving two vacancies is $(C_V)^2$. This and other less probable paths are, therefore, negligible compared to the most probable path of two successive jumps involving only one vacancy.

Order-disorder by an interstitialcy mechanism is less understood because of the complicated interstitial migration process. Experimental evidence (133-135) and theoretical calculations (136,137) show that interstitials in pure metals (Al, Cu, Ni, Mo, Fe) are in

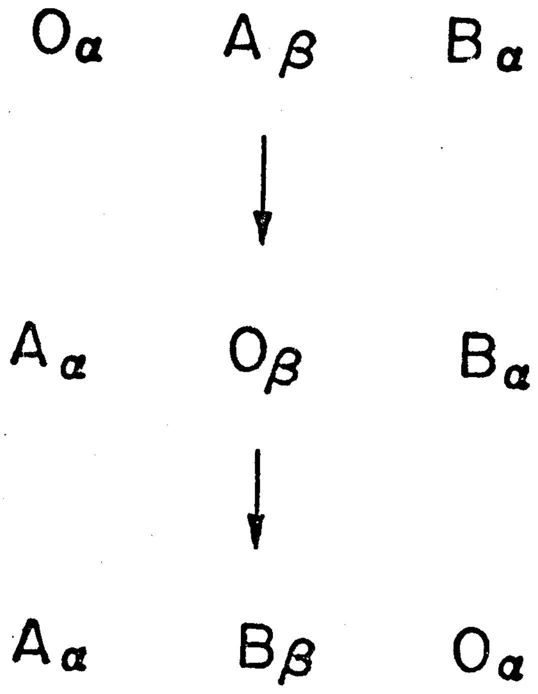

Figure VII-1. The motion of a vacancy (o) jumping from left to right in a lattice made up on two sublattices (α and β sites) can order a disordered lattice. The top line (before the jump) is disordered with B atoms on α sites and A atoms on β sites. After two jumps (bottom line) the atoms are ordered on the sites (A on α and B on β).

the configuration of <100> dumbbells for fcc and <110> dumbbells for the bcc structure. These self-interstitials migrate by combined rotational and translational jumps as shown in Figure VII-2 (138). In such cases, an A-B pair on the wrong sites can be transferred to right sites by three successive jumps involving one dumbbell. This dumbbell must contain the appropriate atom necessary to give a right atom in its final jump. An example in fcc is shown in Figure VII-3. Other reactions for the A-B pair involving more than one interstitial can be neglected compared to the most probable path involving only one interstitial.

However, migration of dumbbell interstitials may be different in alloys. When there is a large difference between the effective atomic volumes of the alloying elements the undersized atoms are preferentially accommodated at the dumbbells. As a result only the undersized atoms are diffusing by this mechanism and the order-disorder reaction is little affected. In general, each reaction path containing three successive jumps should be weighted by a geometric factor and a size dependent, probability factor. While the kinetics of order-disorder transition by the interstitialcy mechanism is still under study, we can introduce an interstitialcy reordering efficiency, σ, and express the Boltzmann factor with the energy barrier U in Eq. (7.8) as,

$$\exp\left(-U_i/k_B T\right) = \sigma\, C_i \exp\left(-3\, E_i^m/k_B T\right) \qquad (7.9)$$

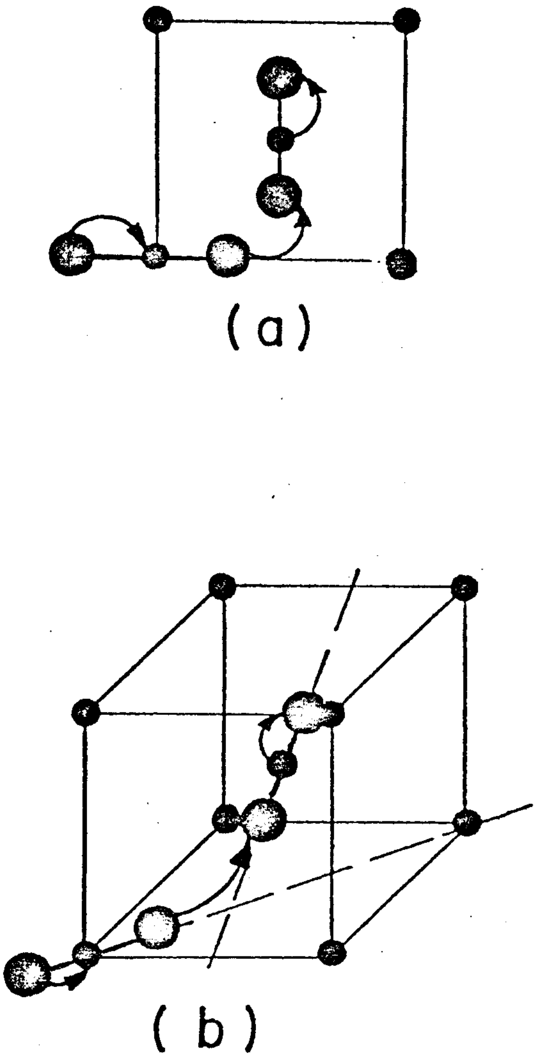

Figure VII-2. Interstitialcy motion in fcc (a) and bcc (b).

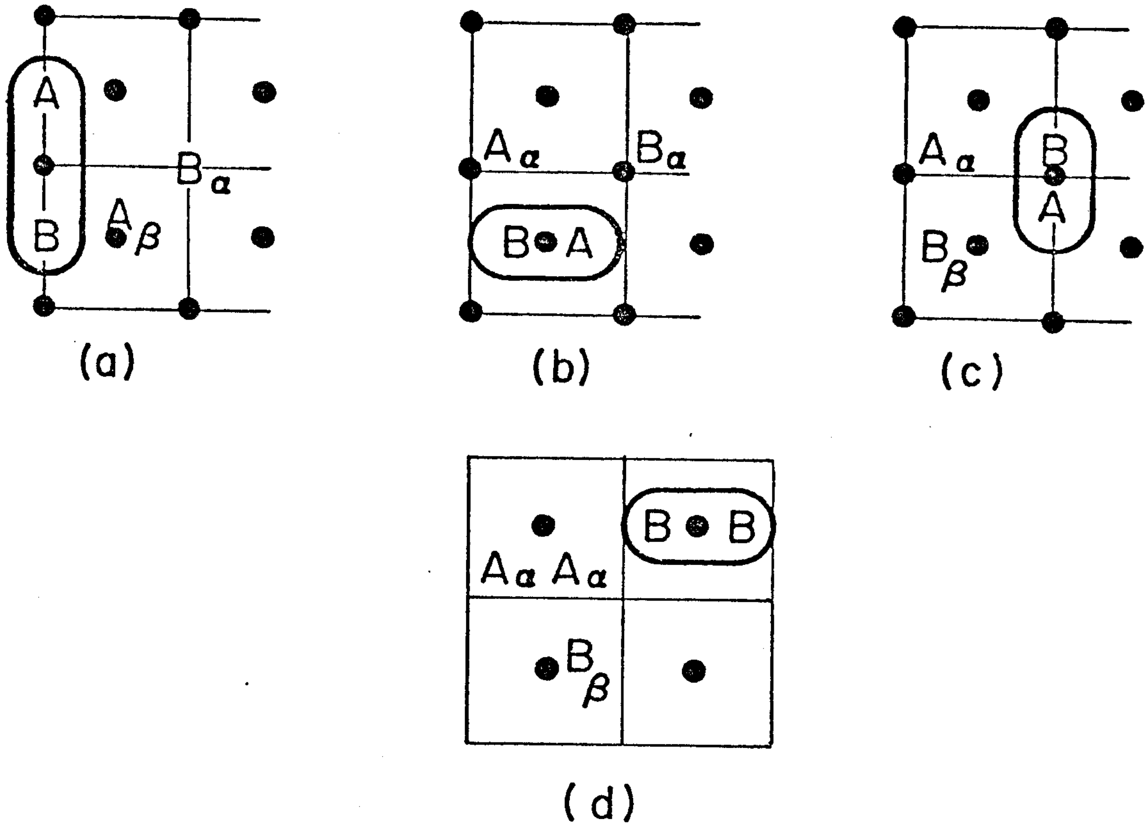

Figure VII-3. Interstitial motion in the Cu_3Au type lattice. The interstitial dumbbell is ringed. Note that its motion causes an ordering with A atoms on the α sites (linked by lines) and B atoms on the β (face centered) sites.

where C_i is the concentration of the interstitials and E_i^m is an effective migration energy of the dumbbell. The parameter σ contains geometric factors determined by the numbers of the reaction paths and the probability factors for reactions to take place by these paths.

By combining Eqs. (7.8) and (7.9), Eq. (7.7) can be written as

$$x = \{\nu_v C_v \exp(-2E_v^m/k_B T)(Z_\alpha + Z_\beta - 2) + \nu_i \, \sigma \, C_i \exp(-3E_i^m/k_B T)\} \left[\frac{X_A}{X_B}\right]^{1/2} Z_\beta \exp(-V_o/2k_B T) \qquad (7.10)$$

where

$$\nu_v = (\nu_r \, \nu_w)_v^{1/2}$$

$$\nu_i = (\nu_r \, \nu_w)_i^{1/2}$$

$$V_o = \begin{Bmatrix} -14\Omega \text{ for bcc} \\ -\ 6\Omega \text{ for fcc} \end{Bmatrix} \text{using the quasi-chemical model for the}$$

$$\text{ordering energy } \Omega = V_{AB} - \frac{V_{AA}+V_{BB}}{2} .$$

By inserting x from Eq. (7.10) into Eq. (7.6b) the radiation enhanced ordering rate can now be determined in terms of the material parameters. The steady-state defect concentrations (C_v and C_i) can be calculated, following Brailsford and Bullough (6), from their dependence on the irradiation and material parameters and temperature.

3) The Order-disorder Transformation Under Irradiation

Having obtained both the ordering and disordering rates from the previous sections we can now determine the steady-state order by inserting them in the rate Eq. (7.2).

The general solution to this rate equation with an initial condition $S = S_o$ at $t = 0$ is

$$S(t) = 1 - p + \frac{p-q}{1 - \left(\frac{S_o+q-1}{S_o+p-1}\right) \exp\,(Zt)} \tag{7.11a}$$

where

$$Z = \varepsilon^2 k^2 + 4 x [x + \varepsilon k/(1 - S_e)]^{1/2},$$

$$p = (-\varepsilon k + z)\ (1 - S_e)/(2x)\ ,$$

$$q = (-\varepsilon k - z)\ (1 - S_e)/(2x)\ ,$$

S_e is the equilibrium long range order parameter and x the reaction constant to be determined. The steady-state solution when Eq. (7.2) is set equal to zero is obtained by $t \to \infty$ in Eq. (7.11a). This gives

$$S = 1 - p = 1 + \frac{(\varepsilon k - z)\ (1 - S_e)}{2x} \tag{7.11b}$$

with the dose in dpa, $\phi = kt$. Equation (7.11b), therefore, gives the steady-state order as a function of dose rate.

Expression (7.11b) contains the equilibrium order parameter in the absence of irradiation (S_e) which can be obtained from order-disorder transition theory (see Ref. 139,140 for reviews). Using the quasi-chemical model of Fowler-Guggenheim (141,142) and Takagi (143), the free energy as a function of the long-range order parameter for the CsCl type superlattice is given by

$$\begin{aligned} F(S) = F(1) + \frac{k_BT}{2} \Bigg\{ & (1+S)\ \ell n\ (1+S) + (1-S)\ \ell n\ (1-S) - 2\ \ell n\ 2 \\ & + Z/2 \left[(1+s)\ \ell n \left(\frac{\xi+S}{1+S}\right) + (1-S)\ \ell n \left(\frac{\xi-S}{1-S}\right) - 2\ \ell n \left(\frac{\xi+1}{2}\right) \right] \Bigg\} \end{aligned} \qquad (7.12)$$

where $\xi = [1 + (1-S^2)\ (\exp(-2\Omega/k_BT)-1)]^{1/2}$ and Z is the coordination number. For the $AuCu_3$ type superlattice, however, this approach, using nearest neighbor pairs fails to predict an order-disorder transition. The pair theory was modified by Yang and Li (144,145) who considered a group of four atoms at a tetrahedral quadruplet of sites as the basic unit and applied the quasi-chemical model to the $AuCu_3$ type superlattice. They successfully predicted a stable superlattice below a given critical temperature. An equivalent calculation by McGlashan (146) using Yang and Li's approach for an AB_3 superlattice is summarized below.

$$\frac{F(S)}{k_BT} = (1/4)(3S+1)\ \ell n\left(\frac{3S+1}{4}\right) + (3/2)(1-S)\ \ell n\ \frac{3(1-S)}{4} + (3/4)(S+3)\ \ell n$$

$$[3/4\ (S+3)] - 3\ \ell n\ 3 + \ell n\ (a/a^*) + 3\ \ell n\ (h/h^*) + 3\ S\ \ell n$$

$$(cf^*/c^*f) - \frac{X_A+3X_B}{k_BT}\ . \tag{7.13}$$

The constants are

$$a^* = (3S+1)\ (1-S)^3/256$$

$$c^* = (3S+1)\ (1-S)\ (S+3)^2/256$$

$$f^* = 3(1-S)^3\ (S+3)/256$$

$$h^* = 3(1-S)\ (S+3)^3/256\ .$$

The parameters a, c, h and f are determined by the equations

$$a = \frac{3S+1}{4} - 3b - 3c - d$$

$$h = 3/4\ (1-S) - 3g - 3f - e$$

$$\frac{a}{\zeta^3} = \frac{b\eta^3}{\zeta^2} = \frac{c\eta^4}{\zeta} = d\eta^3 \tag{7.14}$$

$$\frac{e\eta^3}{\zeta^3} = \frac{f\eta^4}{\zeta^2} = \frac{g\eta^3}{\zeta} = h$$

with ζ given by the solution of

$$\frac{3S+1}{1-S} = \frac{(1-3\zeta^2\eta^{-4}-2\zeta^3\eta^{-3})\ (1+3\zeta^{-1}\eta^{-3} + 3\zeta^{-2}\eta^{-4} + \zeta^{-3}\eta^{-3})}{(1+2\zeta^{-1}\eta^{-3} + \zeta^{-2}\eta^{-4})\ (1+3\zeta\eta^{-3} + 3\zeta^2\eta^{-4} + \zeta^3\eta^{-3})} \tag{7.15}$$

and where $\eta = \exp(\Omega/k_BT)$.

The thermal equilibrium long-range order parameter S_e can, therefore, be determined by minimizing F(S) with respect to S using one or the other of these models as appropriate.

4) Application to Cu_3Au

The present model of order-disorder transition under irradiation is here applied to the $AuCu_3$ superlattice. The resulting long-range order parameter as a function of temperature for a series of dose rates is shown in Figure VII-4, and the variables for this calculation are shwon in Table VII-1. The interstitialcy reordering mechanism is neglected by setting $\sigma = 0$ because of the large difference between the effective atomic volumes of copper and gold. The defect parameters for pure Cu are used in this calculation. The ordering energy Ω (used in calculating S_e) is fixed such that the critical temperature predicted coincides with the experimental value, T_c = 663°K. As shown in Figure VII-4, a dose rate as low as 10^{-15} dpa/sec is able to disorder the $AuCu_3$ superlattice below ∿430°K. A dose rate of $k \geq 1 \times 10^{-5}$ dpa is necessary to completely disorder the ordered alloy at all temperatures. A partial phase diagram under irradiation, based on these results, is shown in Figure VII-5. The low temperature limit of the ordered phase is taken from Figure VII-4. The remaining boundaries of the ordered region are assumed to diverge smoothly from their equilibrium positions as shown.

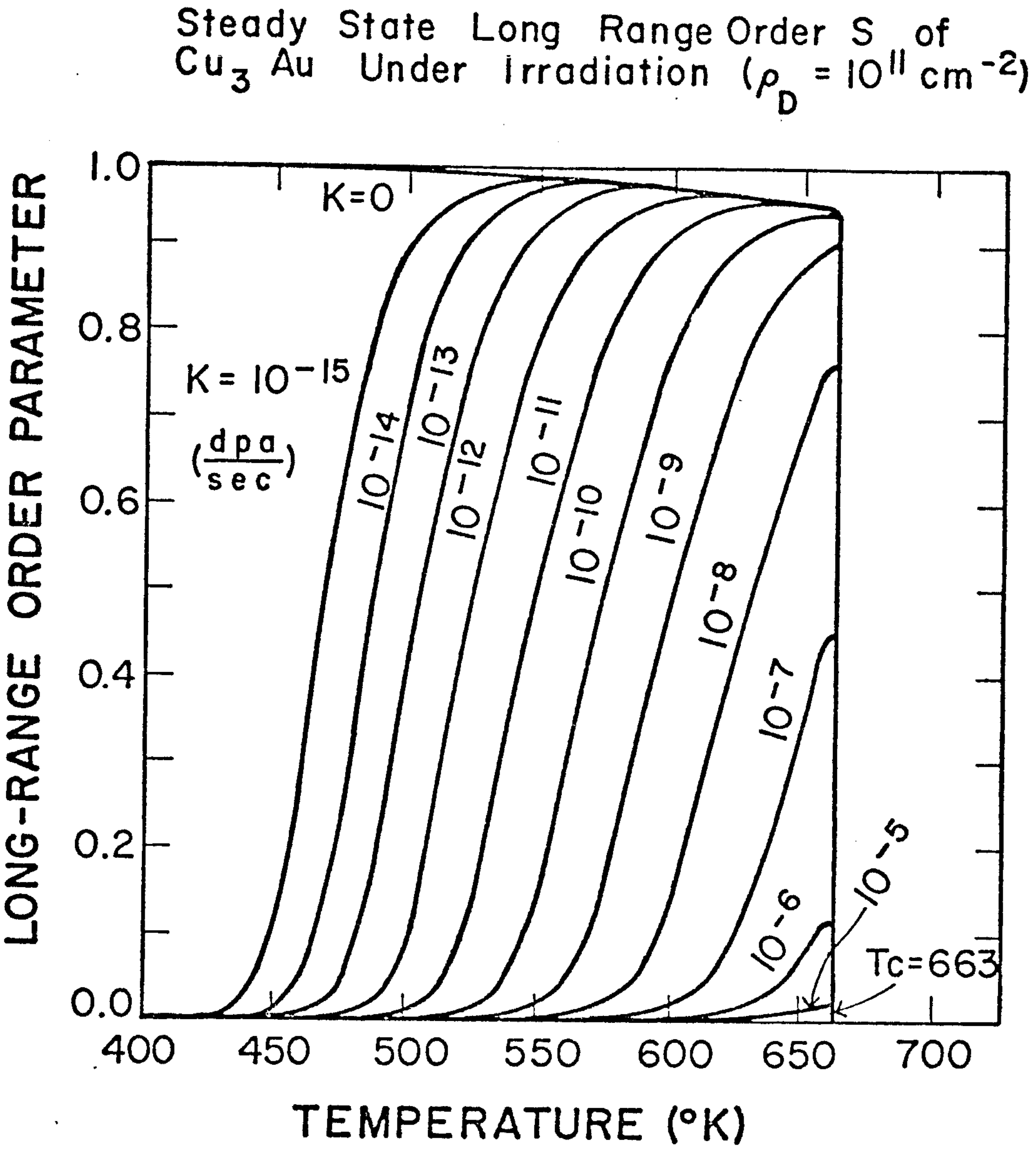

Figure VII-4. The steady-state long range order parameters of Cu_3Au under irradiation for various irradiation rates k (in dpa/sec) as indicated.

Table VII-1
Parameters used for the calculation of the long-range order of Cu_3Au under irradiation.

ε	ρ_d	Z_v	Z_i	E_v^f	E_v^m	D_o	$(\nu_r \nu_w)^{1/2}$	σ
10	$1 \times 10^{11} cm^{-2}$	1.0	1.02	1.28 eV	0.71 eV	$0.78 \frac{cm^2}{sec}$	$10^{13} sec^{-1}$	0

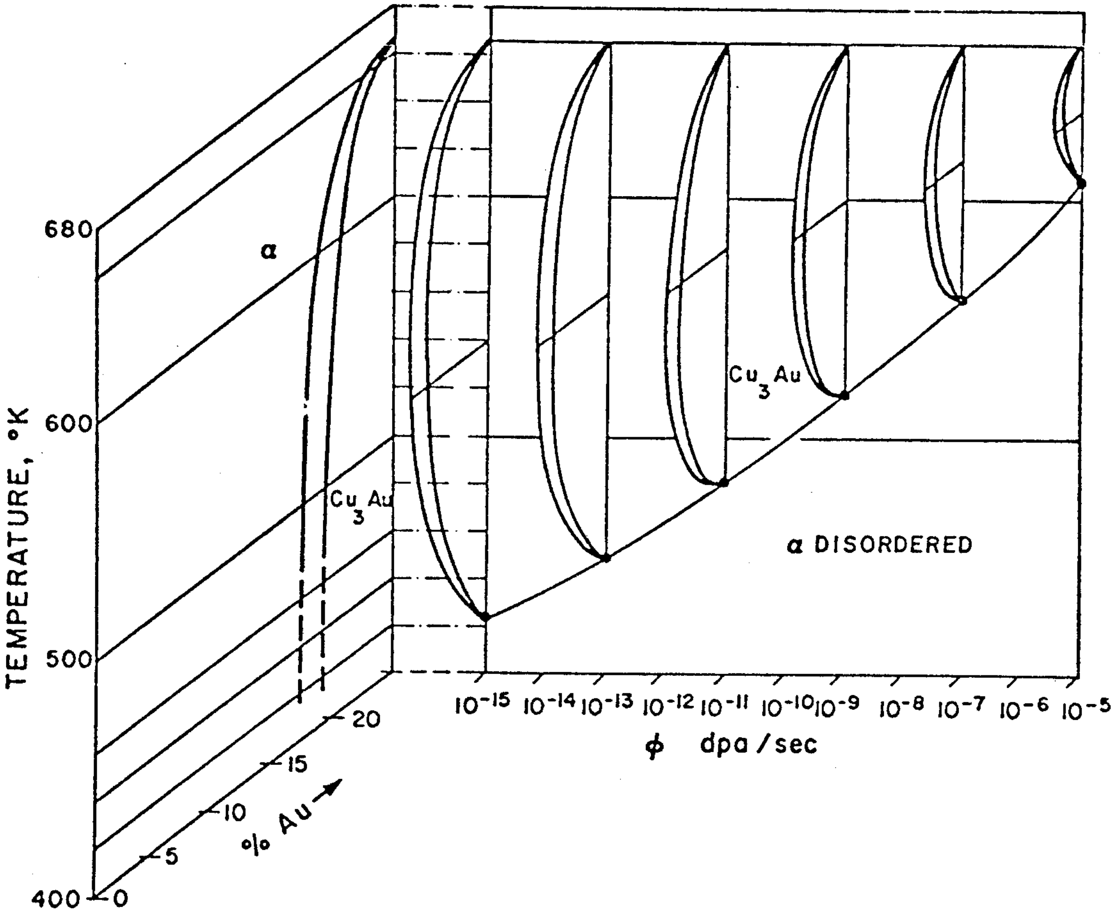

Figure VII-5. The radiation modified partial phase diagram from the Cu_3Au region of the Cu-Au system. The equilibrium phase diagram is on the left and radiation modified versions of the Cu_3Au loop are plotted as a function of dose rate on the third axis. The calculated points marking the minimum temperature for the ordered region are shown as dots at the base of each loop. The sides of the loops are schematic only.

Several investigators (147-152) have irradiated Cu_3Au; however, all these workers appear to have studied transient phenomena over limited dose ranges so that no measures of steady-state properties have been made. Most workers monitored resistivity and the connection between this and order is not simple. Therefore, there are no results to compare with the predictions of this section and further experimental work is required.

Finally, it should be noted that irradiation can actually increase the degree of order in a phase. This is probably an example of radiation enhancement of a sluggish reaction. Figure VII-6 shows schematically how this can occur. Consider a phase which has not been aged for sufficient time to produce the equilibrium degree of order, the maximum order obtained is, therefore, less than unity (S_o). Under irradiation, however, in the temperature range just below T_c, radiation enhanced diffusion increases the thermal reordering rate causing the steady-state order parameter to lie above the original incompletely equilibrated level (Fig. VII-6). The arrows on the diagram indicate the direction in which the order parameter will change under irradiation.

C, Radiation Induced Phase Instability

The change in the order-disorder region of an alloy described in Section B-4 is an example of an irradiation modified phase transition. When a strongly ordered intermetallic compound is in thermal equilibrium with other phases of the alloy, disordering of this ordered compound can change the whole alloy phase structure. As

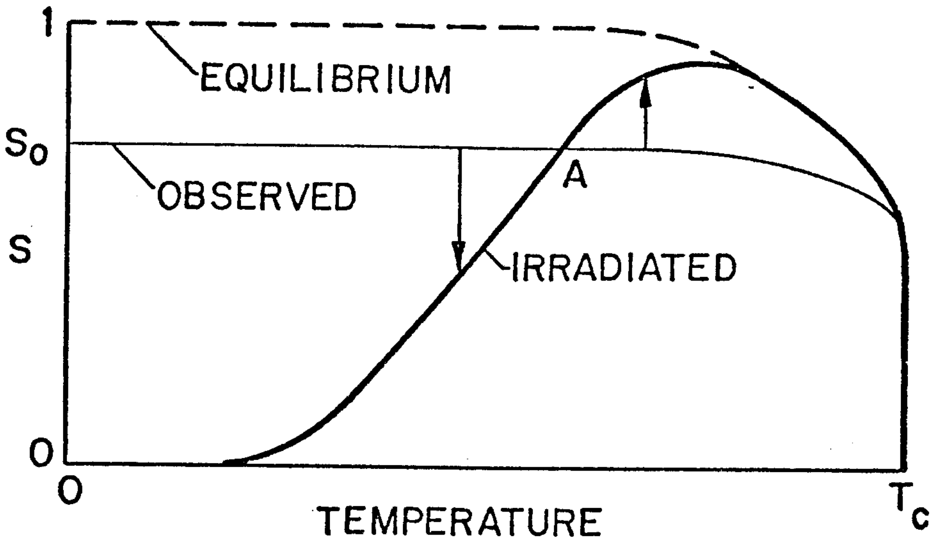

Figure VII-6. Showing how in the temperature range just above point A, radiation induces an increase in order over the incompletely aged state indicated by the line marked "observed". The arrows indicate how the order varies to the right and left of point A.

described in the thermal equilibrium theory of order-disorder transition, atoms in the alloy are arranged to obtain the degree of order which minimizes the free energy. When the alloy is irradiated, it is displaced from thermal equilibrium to a steady-state of long-range order S where the free energy is higher than this equilibrium value. Under irradiation, therefore, a new free energy balance between adjacent phases may be established giving a lower free energy than can be attained with the partially (or entirely) radiation disordered compound.

Figure VII-7 shows the modification of compositions of alloy phases α and γ determined by the common tangents of free energy curves when irradiation induces an increase of free energy δF of the intermetallic compound β.

Since in the above sections the free energy of an ordered phase under irradiation has been obtained, this can be inserted into equilibrium calculations of phase diagrams containing such phases, to obtain the irradiation modified phase fields. This assumes, of course, that the free energy of disordered phases is unaffected by irradiation and that they can achieve a new equilibrium when an ordered phase dissolves.

To illustrate this part of the calculation we take several systems for which calculated phase diagrams have been published and which contain strongly ordering phases. Diagrams for the systems Ti-Co, Nb-Rh and Ti-Ru have been calculated by Kaufman (153) using a set of thermodynamic data listed in Ref. 153. The calculational

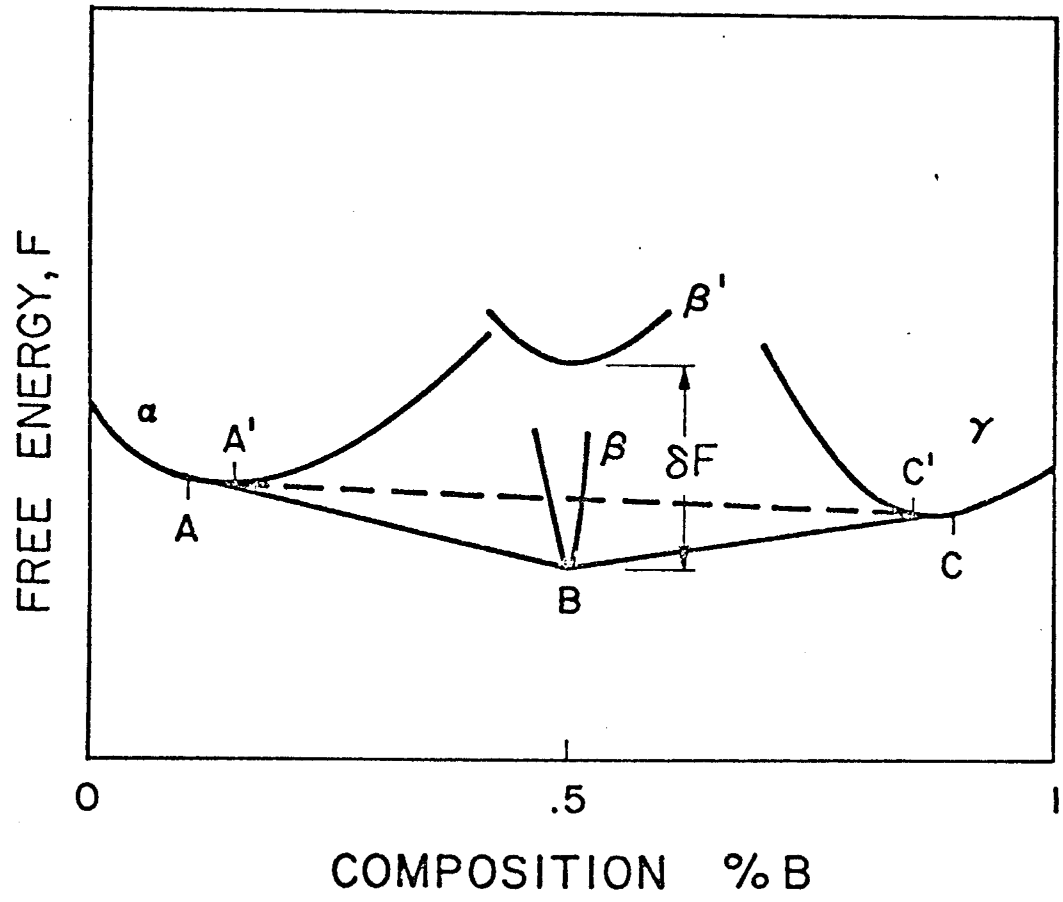

Figure VII-7. Showing how an ordered intermetallic compound β increases its free energy by an amount δF as it disorders to β' under irradiation. The new equilibrium is then indicated by the dashed tangent line A'C' between α and γ phases. Note the change in solubilities from A to A' and C to C' when this occurs.

procedure is based on subregular solution theory as developed by Kubachewski and co-workers (154-157), and adopted in a set of computer programs using a wide range of thermodynamic data, by Kaufman (153,156,157). These computer programs were modified to use the free energy of the compounds calculated from section B, for the steady-state degree of order under irradiation using data given in Table VII-2.

In the case of Ti-Co and Nb-Rh systems the increase in free energy was insufficient to remove the compounds $TiCo_3$ and $NbRh_3$ from the phase diagram. Instead the phase boundary of the terminal solid solution was progressively shifted to higher solubilities, reflecting the change in common tangent contact point on the free energy curve for the terminal solutions. The limit of the effect of radiation occurs when the compound is fully disordered at lower temperatures. At intermediate temperatures the boundary lies between the thermal equilibrium value (fully ordered compound) and the higher solubility appropriate for a balance with the fully disordered compound. The separation of the phase boundary from the equilibrium position occurs at higher temperatures for higher irradiation rates as Figures VII-8 and VII-9 show. The irradiation rates chosen (10^{-7} and 10^{-3} dpa/sec) are appropriate to fast reactor neutrons and heavy ion irradiations, respectively. These results show that particles of the ordered phase in the α matrix will shrink under irradiation and may dissolve entirely if the alloy composition is close to the phase boundary.

Table VII-2

	ε	$\rho_d(\mathrm{cm}^{-2})$	Z_v	Z_i	$E_v^f(\mathrm{eV})$	$E_v^m(\mathrm{eV})$	$D_o(\frac{\mathrm{cm}^2}{\mathrm{sec}})$	σ	$E_i^m(\mathrm{eV})$	$D_{io}(\frac{\mathrm{cm}^2}{\mathrm{sec}})$	$\Omega(\mathrm{eV})$	$(\nu_v\nu_i)^{1/2}$ (sec^{-1})
TiRu	10	10^{11}	1.0	1.02	1.6	1.0	1.0	0	-	-	0.18	10^{13}
$TiCo_3$	10	10^{11}	1.0	1.02	1.6	1.0	1.0	0.01	0.15	0.01	0.20	10^{13}
$NbRb_3$	10	10^{11}	1.0	1.02	1.0	1.0	1.0	0.01	0.15	0.01	0.16	10^{13}

(1) $\alpha/D_i = 10^{17}$ used in all cases to compute defect concentrations (where α is the recombination parameter) (6)

(2) The defect parameters of pure T_i are used as an approximation in TiRu and $TiCo_3$. Defect parameters are assumed in $NbRb_3$ calculation.

(3) The ordering energy Ω is obtained from thermodynamic data in Ref. 153 and is assumed to be temperature independent.

(4) $\sigma = 0$ in the TiRu compound because the large size difference makes interstitialcy reordering unlikely. The σ values of 0.01 for $TiCo_3$ and $NbRh_3$ are estimates.

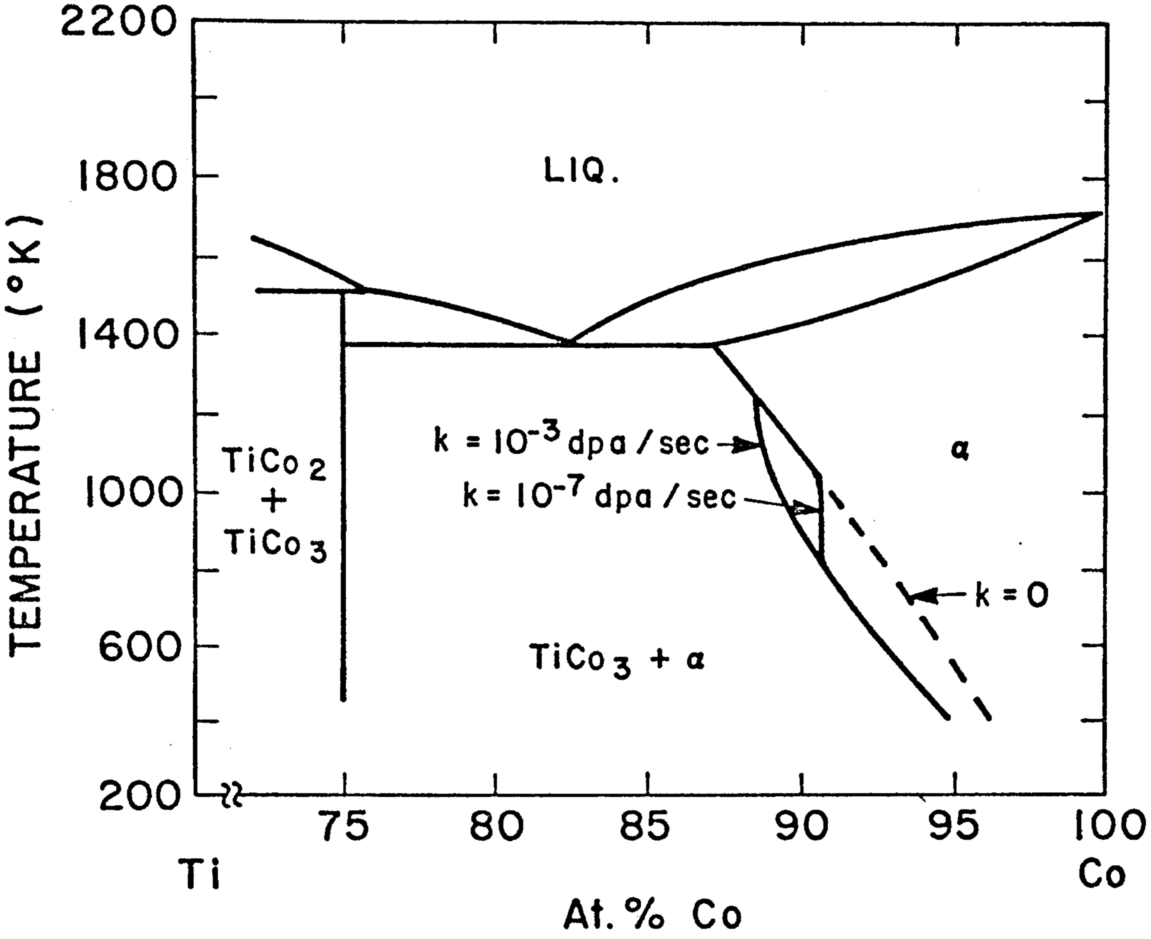

Figure VII-8. The calculated partial phase diagram for the Ti-Co system as modified by irradiation at the damage rates shown. The original equilibrium phase boundary is the k=0 line.

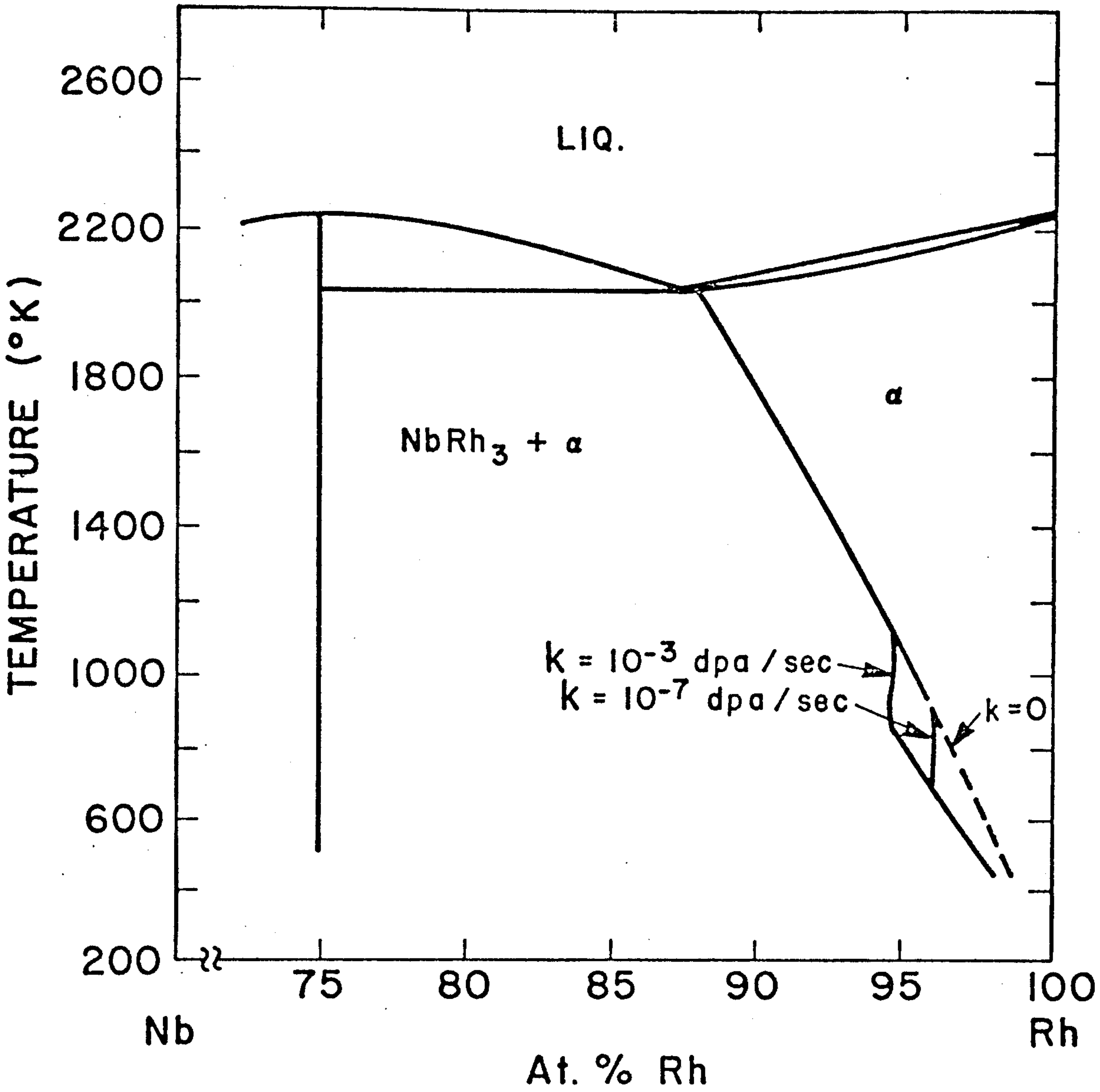

Figure VII-9. The calculated partial phase diagram for the Nb-Rh system as modified by irradiation at the rates shown.

The calculated equilibrium phase diagram [following Kaufman (153)] for the TiRu system is shown in Fig. VII-10a; it agrees closely with experiment. The diagram contains the strongly ordering compound TiRu, for which the free energy shift on disordering is particularly large since the equi-atomic composition maximizes the number of wrong bonds when disordered. The order parameter calculated from this model is shown in Fig. VII-11, the variation of vacancy concentration at steady-state is also shown. The parameters used in the calculation are found in Table VII-2.

The large increase in free energy as the compound disorders under irradiation, lifts the compound's free energy curve above the common tangent for the adjacent phases. A new balance state then occurs based on the mixture of these two phases (β and ε') giving a new two-phase region on the diagram (Fig. VII-10b and c). At the equi-atomic composition the free energy of the β phase itself is lower than the disordered TiRu so that the β field extends over this range as the figure shows.

The temperature at which the TiRu phase disappears depends upon the irradiation rate. A critical degree of disorder is required to remove the phase above the β free energy and this depends upon the disordering rate which in turn depends upon the irradiation rate (Figs. VII-10b and c).

The diagram shows that the disordered compound will transform to β. If the compound exists as particles in an ε' matrix (the β+ε' region) the new β phase may form by in-situ transformation of the

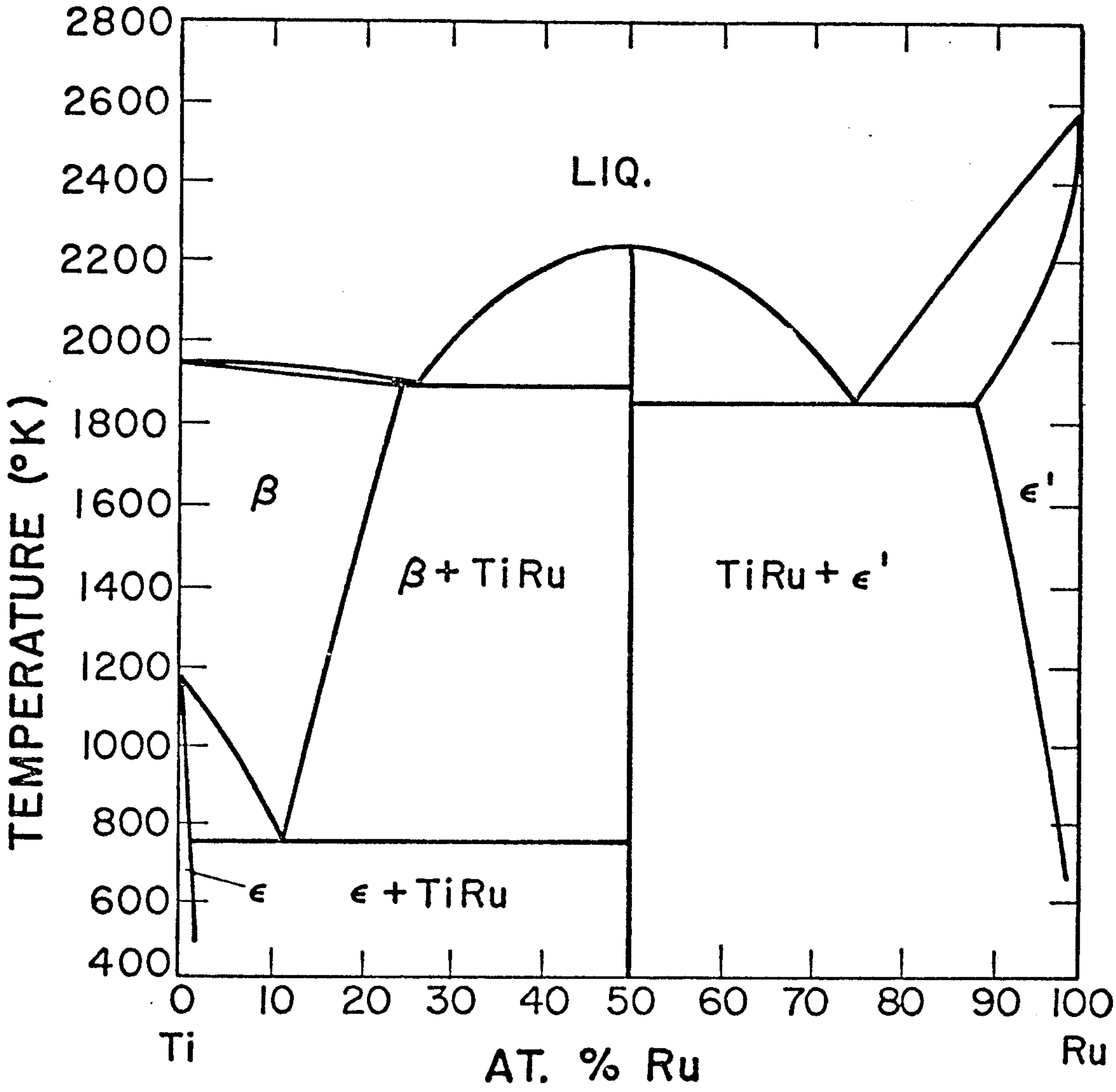

Figure VII-10-a. The equilibrium phase diagram for the Ti-Ru system as calculated by Kaufman.

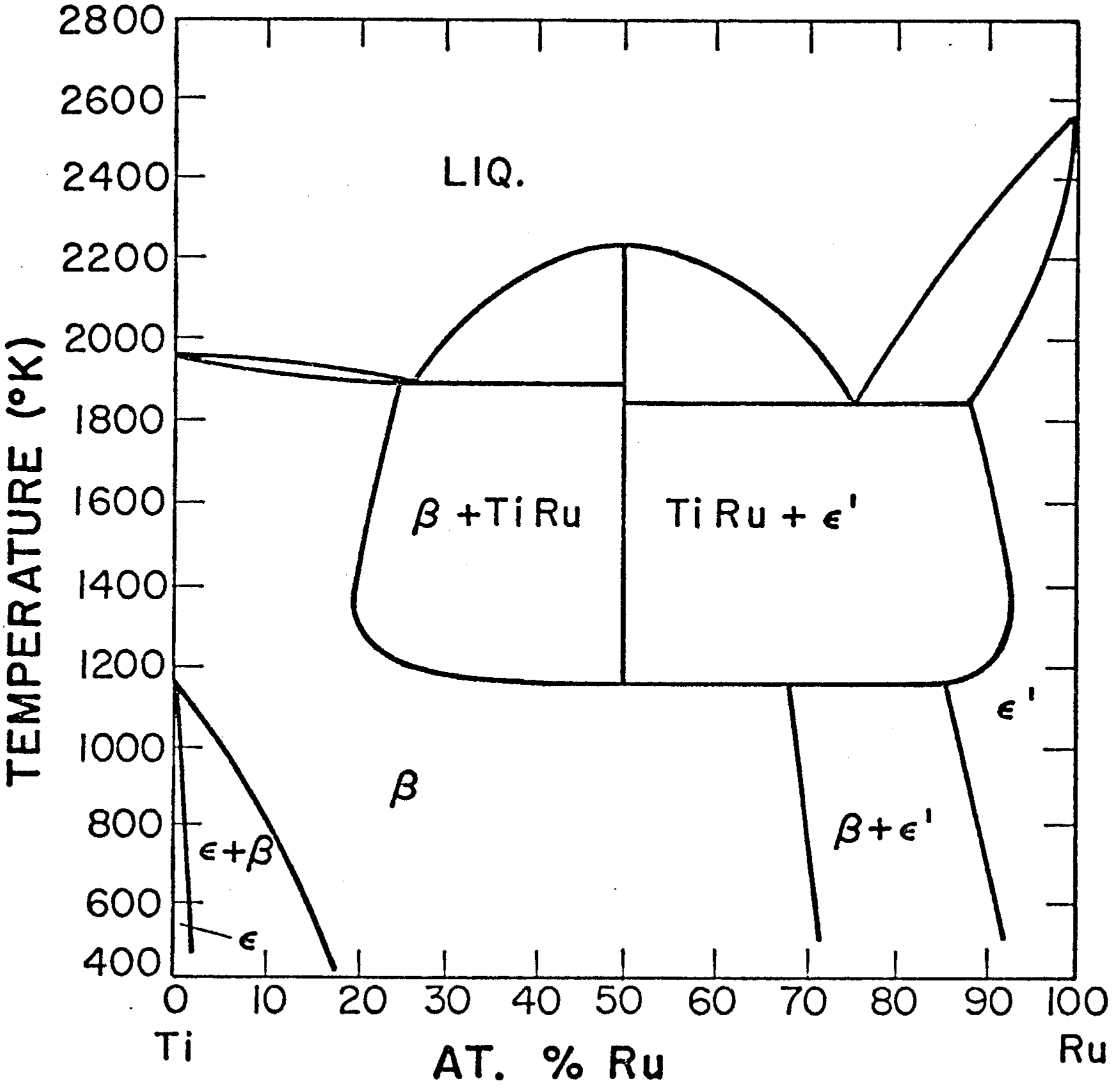

Figure VII-10-b. The radiation modified Ti-Ru system for a dose rate of 10^{-3} dpa/sec, calculated using the data in Table VII-2 and Ref. (153).

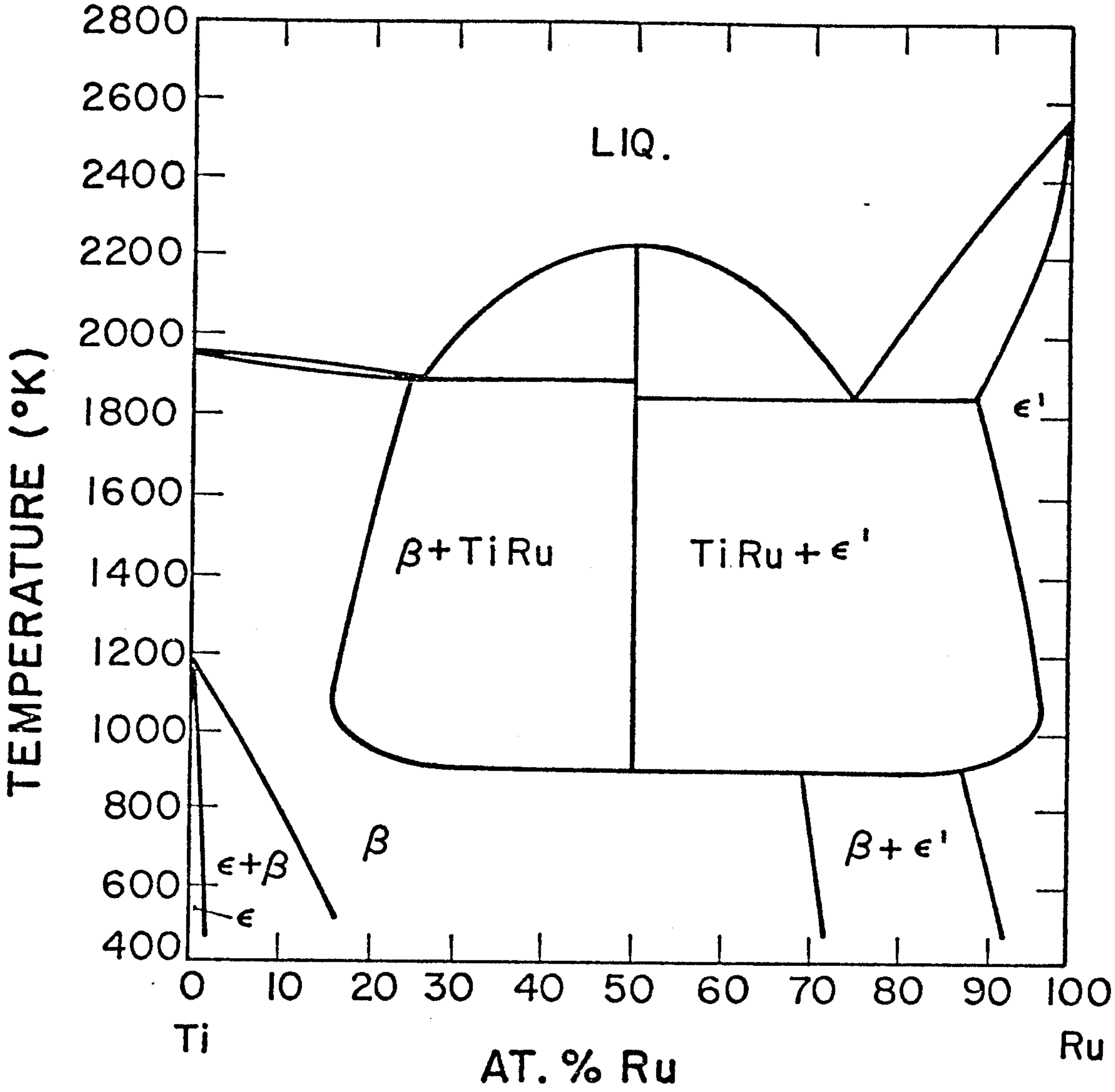

Figure VII-10-c. As 10 b) for a dose rate of 10^{-7} dpa/sec.

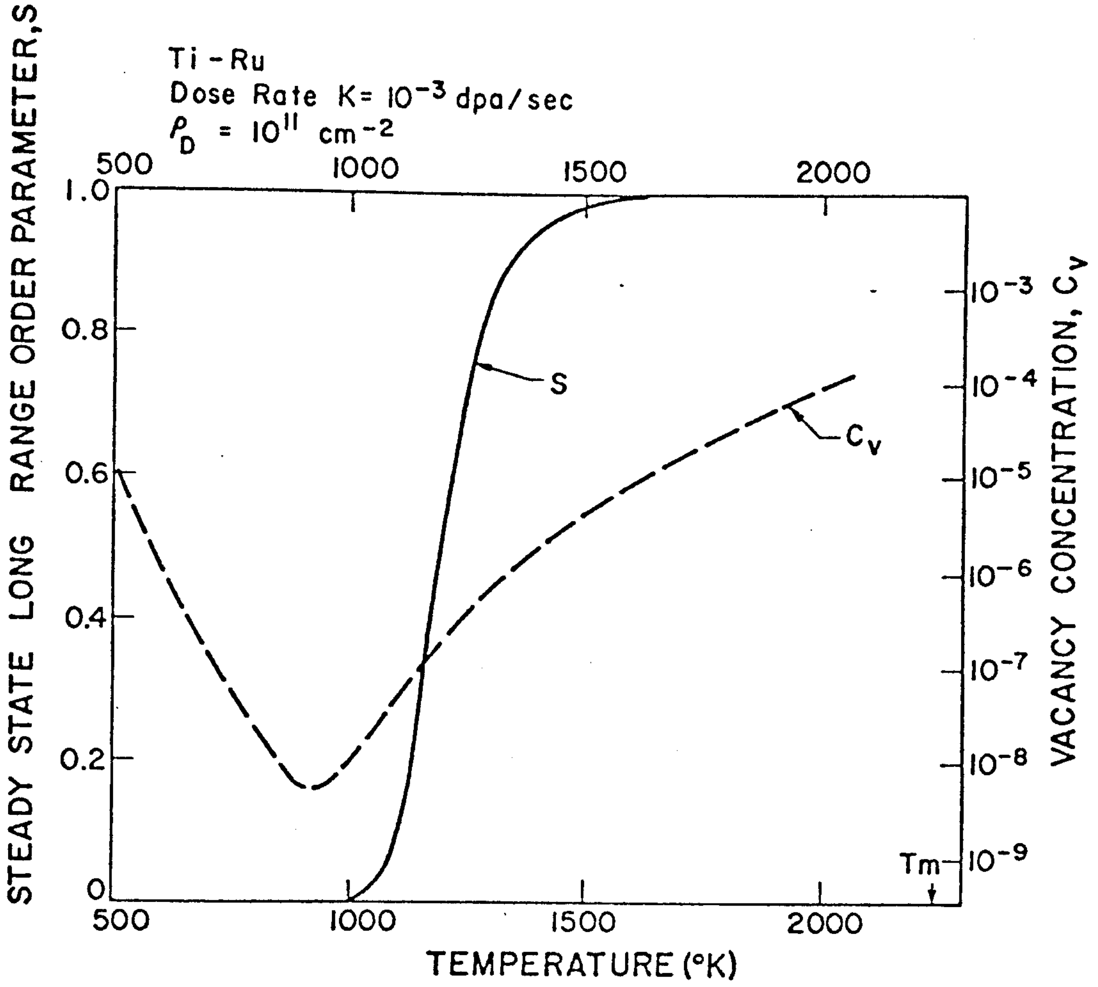

Figure VII-11. The variation of vacancy concentration C_V and order parameter S, in Ti-Ru under a dose rate of $k = 10^{-3}$ dpa/sec. Calculated using the data in Table VII-2 following the method of Ref. (6).

disordered TiRu or by nucleation and growth from the supersaturated ε' produced by TiRu dissolution.

The detailed mode of transformation of the destabilized compound will depend upon kinetic features which remain to be explored and are not included in the current model.

D. Discussion

1) Examples of Radiation-disorder Instabilities

Williams, Stiegler and Wiffen (160) irradiated W-Re alloys in EBR-II to the doses of $6.1 \sim 37 \times 10^{21}$ neutrons/cm^2 (> 0.1 MeV). They reported formation of χ-phase (WRe_3) in a single-phase (bcc W-rich solid solution) region close to the (bcc+σ) phase boundary. σ is an ordered phase (near 50 at.%Re) between the tungsten-rich bcc and the disordered χ-phase in the thermal equilibrium phase diagram. Kaufman et al. (161) estimated the increase of the free energy of σ-phase necessary for the formation of χ-phase to be $\sim$5440 J/mole (1.3 k cal/mole). They used Maydet and Russel's theory (64) to compute the irradiation-induced effective free energy change which turned out to be well below the value necessary for the suppression of σ-phase. $5\sim10$ kJ/mole, however, could be easily attained by disordering the ordered σ-phase resulting in its dissolution and replacement by the disordered χ-phase, as in the T-Ru case. Though the mechanism of the phase instability of W-Re system can now be understood, the quantitative computation of the irradiation modified phase diagram must await a complete crystallographic structure determination of the complicated σ-phase.

A similar disappearance of σ-phase has been observed in the Fe-Ni-Cr system. Brown and Cawthorne (162) were unable to detect σ-phase after irradiation at temperatures up to 700°C. In this range σ-phase is regularly observed and its presence is predicted from thermodynamic calculations. In its place a γ' precipitate formed. The absence of σ-phase has been confirmed by Bilsby (163). Thermodynamic data are unavailable for both the σ- and γ'-phases at the present time. In addition, the details of the ordering arrangement in σ-phase are unclear. It is, therefore, not possible to calculate the ternary diagram at the present time. However, the fact that the strongly ordered, equi-atomic σ-phase disappears certainly suggests radiation disordering as a possible cause.

This model so far has considered only the effect of chemical bonding in the ordered structures. The next step is the more difficult one of calculating the energy change under irradiation when the order is due to the size difference of atoms (e.g. Laves phases). Obviously, a similar phenomenology will apply but the calculation of the free energy of such phases when they are disordered by irradiation is very difficult. It seems likely that such effects will be very large, readily destabilizing such phases.

Finally, it should be noted that a large change in free energy on disordering does not guarantee a large phase diagram change. If the ordered phase is much more stable than surrounding phases even large shifts will not destabilize it entirely.

2) Implications for Alloy Design

The calculations presented demonstrate that radiation induced disordering is capable of radically altering phase diagrams under irradiation. Since radiation disordering as a phenomenon has already been demonstrated experimentally, it is clear that we have a sound explanation for phase instabilities under irradiation.

In this model we make no attempt to improve on current theories of order-disorder, the objective has been to provide a clear conceptual framework for further experiment. Experimental results for the reordering and disordering rates under irradiation, together with the necessary thermodynamic data, are all that are required to determine phase diagrams.

From the alloy design point of view we can conclude that phases having the following characteristics are likely candidates for radiation induced destabilization.

a) A very high ordering energy.
b) A similar stability (free energy) to adjacent phases.
c) Close to equi-atomic concentration.

This model offers a guide to a particular type of phase stability which must be combined with solute segregation and other mechanisms to obtain an overall picture of alloy stability under irradiation. Such a comprehensive approach will require that all the various aspects described in the introduction are included. One can now begin to distinguish how this problem should be attacked within the framework of our current understanding.

Firstly, alloy design should be based on a knowledge of the true equilibrium state of the material and its approach to this equilibrium under irradiation. Secondly, solute-defect coupling should be evaluated based on measurements and theory currently available. Thirdly, second phases used to strengthen the material, or which may form under irradiation need to be evaluated. This latter step will include the model of this chapter, but kinetic effects associated with nucleation of new phases stabilized by irradiation will need to be added so that radiation phase diagrams can be used to predict which phases will actually occur in practice.

Clearly, this requires a major research effort a substantial part of which will involve measurements of basic thermodynamic properties in systems of interest.

3) Limitations of the Model

Probably the most important assumption made in the calculations described here is that when a given compound disorders and becomes unstable with respect to a mixture of two adjacent phases, then a new equilibrium will be attained. Since this involves the nucleation and growth of a new phase in the structure, whether or not equilibrium is attained depends on kinetic factors. Both nucleation and growth depend on diffusion and this will be enhanced by irradiation, because of the larger defect population. However, at very low temperatures defects will remain frozen and the new phase will be unable to form. Under these conditions the radiation phase diagram will not be obeyed and the two-phase region will be found in practice to consist of a supersaturated solution produced by the dissolution of ordered particles.

The relevant free energy which the disordered compound must then exceed is that of the supersaturated matrix rather than the free energy of the two phase mixture.

Even if diffusion is permitted new phases may not nucleate. However, at this point a unified approach would consider radiation affected nucleation which has been discussed for incoherent precipitates by Maydet and Russil (64) and for coherent precipitates by Martin (122). In both of these approaches nucleation may be either promoted or inhibited. Further study on the kinetics of the steady-state conditions is needed.

This model is also limited by the fact that we have selected a simple phenomenological approach to order-disorder so as to provide a framework for using experimental values of ordering and disordering rates under irradiation. The calculational details, therefore, rest on the assumptions of quasi-chemical or sub-regular solution theory and the long range order approximation. However, in an area of high technological interest, it is better to use simple models with phenomenological adjustment to produce detailed agreement with experiment rather than to attempt very complex ab-initio calculations with less general models.

E. Summary

1. Starting from current knowledge on the disordering of structures under irradiation it has been shown that the free energy changes produced are sufficient to cause many ordered phases to become unstable.

2. Phase diagrams under irradiation can be calculated if ordering or disordering rates are known (together with necessary thermodynamic data for the equilibrium diagram).

3. In general at low temperature, phases which have undergone an order-disorder transition on cooling, can be forced to revert to the disordered form by irradiation. The temperature for this has been calculated for Cu_3Au as a function of dose rate.

4. Several cases of radiation phase instabilities may be explicable by this mechanism.

VIII. CONCLUSIONS

Heavy-ion irradiation damage in pure Mo and Mo-9.1at.%Zr has been investigated and the phase stability of the two-phase alloy under irradiation has been studied. The results show that the addition of 7.5-at.%Zr to Mo (the saturated Mo-rich solid solution) reduces or supresses void swelling at low temperatures ($\leq$ 800°C). At higher temperatures ($\geq$ 850°C) swelling in the alloy is significantly increased at higher doses ($\geq$ 4 dpa) though it is reduced at lower doses compared to pure Mo.

The reduction in void swelling of the alloy at lower temperatures or doses is due to the difficulty in void nucleation while the larger total swelling at higher doses and higher temperatures is caused by the higher void growth rate than pure Mo. The Zr may be gettering a gas impurity (probably oxygen) which is necessary for significant void nucleation, resulting in an incubation period required for void formation.

A high density of dislocation loops form in the alloy during the incubation period for void nucleation. The higher dislocation density may provide a larger biased sink strength which increases void growth rate. Faulted interstitial loops ($\vec{b}$ = a/2 <110>) were observed, indicating that stacking fault energy is reduced by Zr solute addition.

In pure Mo, a high density of loops form only at lower temperature close to the void formation threshold. The formation of rafts of small loops in Mo is evidence for the gliding of unfaulted loops in Mo. The reduced stacking fault energy in the alloy promotes loop nucleation and allows loops to remain faulted after nucleation. Being faulted, the small loops are unable to glide to form rafts in contrast to pure Mo.

Irradiation induced precipitation of γ-phase (Mo_2Zr) at grain boundaries were observed. Among all the models of phase instability proposed, it is most easily explained by the enrichment of Zr at the grain boundary due to defect-solute flux coupling caused by a large binding between the vacancy and the over-sized Zr atom.

A kinetic model of order-disorder transformations under irradiation has been developed. The rate equation is solved for both transient and steady state. The theory is applied to compute the steady state long-range order of Cu_3Au under irradiation.

Phase instability of alloys due to the disordering of an intermetallic compound is proposed. The free energy of the partially or completely disordered phase is calculated such that radiation modified phase diagrams can be computed. The theory is applied to compute the phase diagrams of Ti-Co, Nb-Rh and Ti-Ru systems under conditions typical of neutron irradiation and heavy-ion bombardment.

Experimental observation of the phase instabilities of W-Re and Fe-Ni-Cr systems are explained on the basis of this theory while quantitative calculation of these two alloy systems with more complicated crystallographic structures (σ-phase) is still being studied.

REFERENCES

1. C. Cawthorne and E. J. Fulton, *Nature* *216*, 575 (1967).

2. G. L. Kulcinski, Proceedings of Int. Conf. on *Radiation Effects and Tritium Technology for Fusion Reactors*, Gatlinburg, Tenn., Oct. 1975, CONF-750989, p. 1-17 (1976).

3. R. S. Nelson and D. J. Mazey, *Radiation Damage in Reactor Materials*, Vol. II, IAEA Symposium Proceedings, Vienna, June 1969, STI-PUB-230, p. 157 (1969).

4. J. L. Katz and H. Wiedersich, *J. Chem. Phys*., *55*, 1414 (1971).

5. K. C. Russell, *Acta Met*., *19*, 753 (1971).

6. A. D. Brailsford and R. Bullough, *J. Nucl. Matls*. *44*, 121 (1972).

7. R. Bullough and R. C. Perrin, Proc. of Int. Conf. on *Radiation Induced Voids in Metals*, Albany, N.Y., June 1971, CONF-710601, p. 769 (1972).

8. R. Bullough, B. L. Eyre and K. Krishan, *Proc. R. Soc. London* *A346*, 81 (1975).

9. O. Hauser, M. Schenk, *Keinenenergie* *6*,(12), 655 (1963), available in trans. from H. M. stationary office, London as AERE Trans. 1008.

10. A. C. Damask, AIME Symp. on *Radiation Effects*, Ashville, N.C., p. 77.

11. K. C. Russell, 1st Conf. Effects in *Breeder Struct. Materials*, Scottsdale, (1977), p. 82.

12. Y. Adda, M. Beyeler, G. Brebec, *Thin Solid Films* *25*, 107 (1975).

13. J. A. Hudson, *J. Br. Nucl. Energy Soc*. *14*, 127 (1975).

14. P. Wilkes, Workshop on Solute Segregation and Phase Stability, Gatlinberg, Nov. 1978, to be published in J. Nucl. Materials.

15. P. S. Dklad and T. E. Mitchell, *Acta Met*. *23*, 1287 (1975).

16. K. L. Bertram, F. J. Minter, J. A. Hudson and K. C. Russell, to be published in J. of Nucl. Materials (1978).

17. R. S. Nelson, J. A. Hudson and D. J. Mazey, *J. Nucl. Matls*. *44*, 318 (1972).

18. P. R. Okamoto and H. Wiedersich, J. Nucl. Matls. 53, 336 (1974).

19. C. Brown, Consultant Symposium on The Physics of Irradiation Produced Voids, Nelson (ed.), Harwell, U.K., 1974, AERE-R7934, p. 83 (1975).

20. R. K. Williams, J. O. Stiegler and W. Wiffen, Oak Ridge Natl. Lab. ORNL-TM-4500 (1974).

21. G. H. Kinchin and R. S. Pease, Reports on Progress in Physics 18, 1 (1955).

22. M. W. Thompson, Defects and Radiation Damage in Metals, Cambridge Univ. Press (1969).

23. F. Seitz and J. Harrison, Phys. Rev. 98, 1530 (1955).

24. W. S. Snyder and J. Neufeld, Phys. Rev. 97, 1636 (1955).

25. J. Neufeld and W. S. Snyder, Phys. Rev. 99, 1326 (1955).

26. I. M. Torrens and M. T. Robinson, Interatomic Potentials and Simulation of Lattice Defects, P. C. Gehlen, J. R. Beeler, Jr., R. I. Jaffe (eds.), Plenum Press, p. 423 (1972).

27. J. Lindhard, V. Nielsen, M. Scharff and P. V. Thomsen, Mat. Fys. Medd. Dan. Vid. Selsk. 33, No. 10 (1963).

28. M. T. Robinsin, Proc. of Conf. on Nuclear Fusion Reactors, British Nuclear Energy Society, p. 364 (1970).

29. J. Lindhard, M. Scharff and H. E. Schiott, Mat. Fys. Medd. Dan. Vid. Selsk. 33, No. 14 (1963).

30. G. L. Kulcinski, J. J. Laidler and D. G. Doran, Radiation Effects, 7, 195 (1971).

31. I. Manning and G. P. Mueller, Com. Phys. Comm. 7, 85 (1974).

32. J. B. Whitley, G. L. Kulcinski, P. Wilkes and H. V. Smith, Jr., J. Nucl. Matls. 79, 159 (1979).

33. J. B. Whitley, Ph.D. Thesis, University of Wisconsin -Madison (1978).

34. H. Wiedersich, , Burton and J. L. Katz, J. Nucl. Matls. 51, 287 (1974).

35. H. Wiedersich, Consultant Symposium on The Physics of Irradiation Produced Voids, ed. Nelson, Harwell, U.K., 1974, AERE-R 7934, p. 147 (1975).

36. K. C. Russell, Scripta Met. 6, 209 (1972).

37. K. C. Russell, Acta Met. 20, 899 (1972).

38. B. T. M. Loh, Acta Met. 20, 1305 (1972).

39. J. L. Katz and H. Wiedersich, J. Nucl. Matls. 46, 41 (1973).

40. W. G. Wolfer and M. H. Yoo, Proc. of Int. Conf. on Radiation Effects and Tritium Technology for Fusion Reactors, Gatlinburg, Tenn. Oct. 1975, CONF-750989, p. II-458 (1976).

41. S.D. Harkness and C.-Y. Li, Met. Trans. 2, 1457 (1971).

42. H. Wiedersich, Rad. Eff. 12, 111 (1972).

43. B. L. Eyre, Int. Conf. on Fundamental Aspects of Radiation Damage in Metals, Gatlinburg, Tenn. 1975, CONF-751006, p. 729 (1976).

44. B. L. Eyre and R. Bullough, Phil Mag. 12, 31 (1965).

45. K.-Y. Liou and P. Wilkes, UWFDM-292, Feb. 1979, submitted to J. Nucl. Materials.

46. F. S. Ham, J. Phys. Chem. Sol. 6, 335 (1958).

47. P. R. Okamoto, S. D. Harkness, and J. J. Laidler, ANS Trans. 16, 70 (1973).

48. P. R. Okamoto, A. T. Santhanam, H. Wiedersich and A. Taylor, Nucl. Tech. 22, 45 (1974).

49. P. R. Okamoto, A. Taylor and H. Wiedersich, Proc. Int. Conf. on Fundamental Aspects of Radiation Damage in Metals, Gatlinburg, Tenn. 1975, CONF-751006, p. 1188 (1976).

50. A. Barbu and A. J. Ardell, Scripta Met. 9, 1233 (1975).

51. E. A. Kenik, Scripta Met. 10, 733 (1976).

52. P. P. Pronko, P. R. Okamoto and H. Wiedersich, Proc. Third Intl. Conf. on Ion Beam Analysis, Washington, D.C., 1977.

53. A. Barbu and G. Martin, Scripta Met. 11, 771 (1977).

54. D. I. Potter, L. E. Rehn, P. R. Okamoto and H. Wiedersich, Scripta Met. 11, 1095 (1977).

55. D. I. Potter and D. G. Ryding, J. Nucl. Matls. 71, 14 (1977).

56. A. D. Marwick, R. C. Piller, *Radiation Effects 33*, 245 (1977).

57. R. C. Piller and A. D. Marwick, *J. Nucl. Matls. 71*, 309 (1978).

58. N. Q. Lam, P. R. Okamoto and R. A. Johnson, submitted to J. Nucl. Materials.

59. T. R. Anthony, Proc. Int. Conf. on *Radiation-induced Voids in Metals*, J. W. Corbett and L. C. Ianniello (eds.), Albany, N. Y., 1971, CONF-710601, p. 630 (1972).

60. R. A. Johnson and N. Q. Lam, *Phys. Rev. B13*, 4364 (1976).

61. N. Q. Lam and R. A. Johnson, *Nucl. Met. 20*, 121 (1976).

62. R. A. Johnson and N. Q. Lam, *Phys. Rev. B15*, 1794 (1977).

63. H. Wiedersich, P. R. Okamoto and N. Q. Lam, to be published in J. of Nucl. Materials.

64. S. I. Maydet and K. C. Russell, *J. Nucl. Matls. 64*, 101 (1977).

65. M. R. Mruzik and K. C. Russell, *J. Nucl. Matls. 78*, 343 (1978).

66. F. A. Smidt, Jr., Naval Research Laboratory Memorandum Report 3293, May 1976.

67. G. L. Kulcinski, J. L. Brimhall and H. E. Kissinger, Proc. Int. Conf. on *Radiation-induced Voids in Metals*, J. W. Corbett and L.C. Ianniello (eds.), Albany, N. Y., 1971, CONF-710601, p. 449 (1972).

68. J. H. Evans, *Radiation Effects 17*, 67 (1973); and AERE-R 6733 (1972).

69. J. L. Brimhall, E. P. Simonen, and H. E. Kissinger, *J. Nucl. Matls. 48*, 339 (1973).

70. J. L. Brimhall and E. P. Simonen, Proc. of Int. Conf. on *Defects and Defect Clusters in B.C.C. Metals and Their Alloys*, R. R. Arsenault (ed.), Gaithersburg, Maryland, p. 321 (1973).

71. J. L. Brimhall and E. P. Simonen, *J. Nucl. Matls. 52*, 323 (1974).

72. J. F. Stubbins, Ph.D. Thesis, University of Cincinnati, Ohio (1975).

73. J. L. Brimhall, Battelle Pacific Northwest Labs. Report on BCC Ion Correlation Experiment, BNWL-2293, April (1977).

74. J. L. Brimhall, Consultant Symposium on The Physics of Irradiation Produced Voids, Nelson (ed.), Harwell, U.K., 1974, AERE-R7934, p. 197 (1975).

75. D. W. Keefer, H. H. Neely, J. C. Robinson, A. G. Pard and D. Kramer, Proc. ASTM Conf. on Irradiation Effects on Structural Alloys for Nuclear Applications, ASTM-STP-484, p. 332 (1970).

76. J. L. Brimhall, L. A. Charlot and H. E. Kissinger, First Topical Meeting on Fusion Reactor Materials, Miami Beach, Florida, Jan. 1979, to be published in J. Nucl. Materials.

77. J. Bentley, B. L. Eyre and M. H. Loretto, Proc. Int. Conf. on Fundamental Aspects of Radiation Damage in Metals, Gatlinburg, Tenn., Oct. 1975, CONF-751006, p. 925 (1976).

78. B. L. Eyre, Defects in Refractory Metals, R. de Batist, J. Nihoul and L. Stals (eds.), (1972).

79. J. Bentley, Ph.D. Thesis, University of Birmingham, England (1974).

80. V. K. Sikka and J. Moteff, J. Nucl. Matls. 54, 325 (1974).

81. V. K. Sikka, Ph.D. Thesis, University of Cincinnati, Ohio (1973).

82. J. D. Elen, G. Hamburg and A. Mastenbrock, J. Nucl. Matls. 39, 194 (1971).

83. F. W. Wiffen, Proc. Int. Conf. on Radiation-induced Voids in Metals, Albany, N. Y., (1971), CONF-710601, p. 386 (1972).

84. Y. Adda, Proc. Int. Conf. on Radiation-induced Voids in Metals, Albany, N. Y., (1971), CONF-710601, p. 31 (1972).

85. B. L. Eyre and A. F. Bartlett, J. Nucl. Matls. 47, 143 (1973).

86. R. C. Rau, R. L. Ladd and J. Moteff, J. Nucl. Matls 33, 324 (1971).

87. G. L. Kulcinski, B. Mastel and J. L. Brimhall, Rad. Effects 2, 57 (1969).

88. A. G. Pard and K. R. Garr, Proc. Int. Conf. on Radiation Effects and Tritium Technology for Fusion Reactors, Gatlinburg, Tenn., 1975, CONF-750989, p. I-312 (1976).

89. B. L. Eyre and A. F. Bartlett, AERE (Harwell-R-7027) (1972).

90. J. Bentley, M. H. Loretto and B. L. Eyre, Proc. Int. Conf. on Radiation Effects and Tritium Technology for Fusion Reactors, Gatlingburg, Tenn., 1975, CONF-750989, p. I-297 (1976).

91. H. V. Smith, Jr., and H. T, Richards, *Nucl. Instr. and Meth.* *125*, 497 (1975).

92. G. T. Caskey, R. A. Douglas, H. T. Richards and H. V. Smith, Jr., to be published in Nucl. Instr. and Meth.

93. J. H. Billen and H. T. Richards, Symposium of North-Eastern Accelerator Personal Conf., Oak Ridge, Tenn., Oct. 1978.

94. K -Y. Liou, H. V. Smith, Jr., P. Wilkes and G. L. Kulcinski, submitted to J. Nucl. Materials.

95. E. Rudy, *Compendium of Phase Diagram Data*, Part V, Air Force Materials Lab. Report AFML-TR-65-2 (1969), or *Metals Handbook*, Vol. 8, p. 322.

96. R. P. Elliott, Armour Research Foundation, Chicago, IL, Technical Report 1, OSR Technical Note OSR-TN-247, p. 38 (1954).

97. D. M. Maher and B. L. Eyre, *Phil. Mag.* *23*, 409 (1971).

98. H. V. Smith, Jr., K.-Y. Liou, G. L. Kulcinski and P. Wilkes, UWFDM-177, Nucl. Engr. Dept., U. of Wisconsin-Madison, WI (1976).

99. K -Y. Liou, P. Wilkes, G. L. Kulcinski and J. H. Billen, presented at the First Topical Meeting on Fusion Reactor Materials, Miami, Florida, Jan. 1979, to be published in J. Nucl. Materials.

100. U. Essmann and M. Wilkens, *Phys. Stat. Sol.* *4*, K53 (1964).

101. M. Wilkens and M. Rühle, *Phys. Stat. Sol* (*b*) *49*, 749 (1972).

102. H. Wiedersich, J. J. Barton and J. L. Katz, *J. Nucl. Matls*. *51*, 287 (1974).

103. J. H. Evans, *Nature* *229*, 403 (1971).

104. J. H. Evans, *Rad. Effects* *8*, 115 (1971).

105. J. H. Evans, *Rad. Effects* *10*, 55 (1971).

106. G. L. Kulcinski and J. L. Brimhall, Proc. of ASTM Conf. on *Effects of Radiation on Substructural and Mechanical Properties of Metals and Alloys*, Los Angeles, CA, June 1972, ASTM-STP-529, p. 258 (1973).

107. J. L. Brimhall, Proc. of Int. Conf. on *Radiation Effects and Tritium Technology for Fusion Reactors*, Gatlinburg, Tenn. Oct. 1975, CONF-750989, p. I-73 (1976).

108. A. M. Stoneham, Consultant Symposium on The Physics of Irradiation Produced Voids, Nelson (ed.), Harwell, U.K., 1974 AERE-R7934, p. 319 (1975).

109. A. M. Stoneham, Proc. Int. Conf. on Fundamental Aspects of Radiation Damage in Metals, Gatlinburg, Tenn. Oct. 1975, CONF-751006-P2, p. 1221 (1976).

110. G. Martin, Phil. Mag. 32, 615 (1975).

111. B. A. Loomis, S. B. Gerber and A. Taylor, J. Nucl. Matls 68, 19 (1977).

112. F. V. Nolfi, Jr., J. Appl. Phys. 47, 24 (1976).

113. L. J. Chen and A. J. Ardell, J. Nucl. Matls. 75, 177 (1978).

114. P. Benoist and G. Martin, Proc. Intl. Conf. on Fundamental Aspects of Radiation Damage in Metals, Gatlinburg, Tenn. Oct. 1975, CONF-751006-P2, p. 1236 (1976).

115. A. D. Brailsford, J. Appl. Phys. 48, 4402 (1977).

116. R. I. Saunderson, P. Wilkes and G. W. Lorimer, Acta. Met. 26, 1357 (1978).

117. V. K. Tewary and R. Bullough, J. Phys F 2, L69 (1972).

118. V. K. Tewary, Adv. Phys. 22, 757 (1973).

119. A. J. E. Foreman, UKAEA Report AERE-R 7135, June (1972).

120. S. B. Fisher and K. R. Williams, Rad. Effects 32, 123 (1977).

121. H. W. King, J. Materials Science 1, 79 (1966).

122. G. Martin, Workshop on Solute Segregation and Phase Stability, Gatlinburg, Tenn. Nov. 1978, to be published in J. of Nucl. Materials.

123. P. Wilkes, K.-Y. Liou and R. G. Lott, Rad. Effects 29, 249 (1976).

124. L. M. Howe and M. H. Rainville, J. Nucl. Matls. 68, 215 (1977).

125. M. L. Jenkins and M. Wilkens, Phil. Mag. 34, 1155 (1976).

126. T. L. Francavilla, R. A. Meussner and S. T. Sekula, Sol. State Comm. 23, 207 (1977).

127. A. R. Sweedler and D. E. Cox, Phys. Rev.B 12, 147 (1975).

128. A. S. Nowick and L. R. Weisberg, Acta. Met. 6, 260 (1958).

129. V. S. Polenok, Fiz. Metal. Metalloved 36, 188 (1973).

130. J. Rothstein, Phys. Rev. 94, 1429 (1954).

131. F. P. Burns and S. L. Quimby, Phys. Rev. 97, 1567 (1955).

132. M. A. Kirk and J. B. Cohen, Met. Trans. 7A, 307 (1976).

133. P. Ehrhart, Proc. Int. Conf. on Properties of Atomic Defects in Metals, Argonne, IL, 1976, p. 200 (1978).

134. W. Schilling, Proc. Int. Conf. on Properties of Atomic Defects in Metals, Argonne, IL, 1976, p. 465 (1978).

135. H. G. Haubold, Proc. Int. Conf. on Fundamental Aspects of Radiation Damage in Metals, Gatlinburg, Tenn, 1975, CONF-751006, p. 268, (1976).

136. R. A. Johnson, J. Phys. F. Metal. Phys. 3, 295 (1973).

137. P. H. Dederichs, Proc. Intl. Conf. on Fundamental Aspects of Radiation Damage in Metals, Gatlinburg, Tenn., 1975, CONF-751006, p. 187 (1976).

138. F. W. Young, Jr., Proc. Int. Conf. on the Properties of Atomic Defects in Metals, Argonne, IL, 1976, p. 310 (1978).

139. T. Muto and Y. Takagi, Sol. St. Phys., F. Seitz and D. Turnbull, (eds.) Vol. 1, p. 193 (1955).

140. L. Guttman, Solid State Phys., Vol. 3, p. 145 (1956).

141. R. H. Fowler and E. A. Guggenheim, Proc. Roy. Soc. A174, 189 (1940).

142. E. A. Guggenheim, Mixtures, Oxford University Press (1952).

143. Y. Takagi, Proc. Phys. Math. Soc. Japan, 23, 44 (1941).

144. C. N. Yang, J. Chem. Phys. 13, 66 (1945).

145. C. N. Yang and Y. Y. Li, Chinese J. Phys. 7, 59 (1947).

146. M. L. McGlashan, Thesis, Reading University (1951), described in Ref. 142.

147. M. A. Kirk and T. H. Blewitt, Met. Trans. 9A, 1729 (1978).

148. T. H. Blewitt and R. R. Coltman, Acta. Met 2, 549 (1954).

149. H. L. Glick, F. C. Brooks, W. F. Witzig and W. E. Johnson, Phys. Rev. 87, 1074 (1952).

150. S. Siegel, Phys. Rev. 75, 1823 (1949).

151. J. A. Brinkman, C. E. Dixon and C. J. Meechan, Acta. Met. 2, 38 (1954).

152. R. A. Dugdale, Phil. Mag., 537 (1956).

153. L. Kaufman and H. Bernstein, Computer Calculation of Phase Diagrams, Academic Press, N. Y. (1970).

154. O. Kubachewski, Phase Stability in Metals and Alloys, Rudman, Stringer and Jaffee (eds.), N. Y., p. 63 (1967).

155. O. Kubachewski and W. Slough, Prog. Mat. Sci. 14, 1 (1969).

156. O. Kubachewski and J. A. Catterall, Thermochemical Data of Alloys, Pergamon Press, N. Y. (1956).

157. F. H. Hayes, F. Muller and O. Kubachewski, J. Inst. Met. 98, 20 (1970).

158. L. Kaufman, Prog. Mat. Sci. 14, 45 (1969).

159. L. Kaufman and H. Bernstein, Phase Diagrams, A. Alper (ed.), Academic Press, N. Y., 1, p. 45 (1970).

160. R. K. Williams, J. O. Stiegler and F. W. Wiffen, ORNL-TM-4500 (1974).

161. L. Kaufman, J. S. Watkin, J. H. Gittus, and A. P. Miodownkik, Calphad 1, 280 (1977).

162. C. Brown and C. Cawthorne, J. Nucl. Matls. 66, 201 (1977).

163. Bilsby, private communication quoted in Ref. 161.

164. B. L. Eyre, J. H. Evans, British Nuclear Society European Conf. on Voids Formed by Irradiation of Reactor Materials, S. F. Pugh, M. H. Loretto and D.I.R. Norris (eds.), p. 323 (1971).